Inorganic—Carbon Nanomaterial Composites for Chemical Sensing

by

James E. Ellis

B.S., Santa Clara University

Submitted to the Graduate Faculty of the

Kenneth P. Dietrich School of Arts and Sciences in partial fulfillment

of the requirements for the degree of

Doctor of Philosophy in Chemistry

University of Pittsburgh

2018

UNIVERSITY OF PITTSBURGH

THE KENNETH P. DIETRICH SCHOOL OF ARTS AND SCIENCES

This dissertation was presented

by

James E. Ellis

It was defended on

August 28th, 2018

and approved by

Haitao Liu, Associate Professor, Department of Chemistry

Nathaniel L. Rosi, Professor, Department of Chemistry

Goetz Veser, Professor, Department of Chemical Engineering

Dissertation Advisor: Alexander Star, Professor, Department of Chemistry

Reproduced with permissions from:

Ellis, J. E.; Green, U.; Sorescu, D. C.; Zhao, Y. Star, A. *J. Phys. Chem. Lett.* **2015**, *6*, 712-717

Ellis, J. E.; Sorescu, D. C.; Burkert, S. C.; White, D. L.; Star, A. *ACS Appl. Mater. Interfaces* **2017**, *9*, 27142-27151

Ellis, J. E.; Star, A. *ChemPlusChem* **2016**, *81*, 1248-1265

Ellis, J. E.; Zeng, Z.; Hwang, S. I.; Li, S.; Luo, T.-Y.; Burkert, S. C.; White, D. L.; Rosi, N. L.; Gassensmith, J. J.; Star, A. *Chem. Sci.* **2019** *Advanced Article*, DOI: DOI: 10.1039/C8SC03987A

Inorganic—Carbon Nanomaterial Composites for Chemical Sensing

James E. Ellis, PhD

University of Pittsburgh, 2018

Carbon nanomaterials have been demonstrated to be excellent transducer materials for chemical sensing. Their high surface to volume ratio, high conductivity, and nanoscale dimensions allow them to be incorporated into miniaturized, low power consumption devices. The attachment of receptors to carbon nanomaterials as an analyte recognition layer is crucial for achieving selective and sensitive chemical sensing. The hybridization of carbon nanomaterials with metals, metal oxides, and other inorganic materials has created a new class of materials, inorganic—carbon nanomaterial composites. These composites seek to combine the properties of inorganic materials with the aforementioned properties of carbon nanomaterials. The surface chemistry and electronic structure of these composites are important for various applications, including chemical sensing.

In this work we describe the synthesis and characterization of novel inorganic—carbon nanomaterial composites. Attachment of the inorganic materials to the carbon nanomaterial layer was achieved through both covalent and noncovalent methods. Characterization of these composites was performed with electron microscopy, X-ray diffraction, photoelectron spectroscopy, fluorescence spectroscopy, Raman spectroscopy, electrical measurements, and gas adsorption measurements. Most of the described inorganic—carbon nanomaterial composites were incorporated into chemiresistor devices for chemical gas sensing.

The indium oxide/single-walled carbon nanotube composite was found to be sensitive to volatile organic compounds such as ethanol and acetone, while the carbon nitride/reduced

graphene oxide composite was sensitive to inorganic gases such as oxygen and carbon dioxide. The sensing mechanisms for these inorganic—carbon nanomaterial composites are explored and discussed. A new photoredox sensing mechanism was demonstrated for the carbon nitride/reduced graphene oxide composite. Tuning the electronic structure of carbon nitride/reduced graphene oxide with copper nanoparticles was found to change the sensor sensitivity toward carbon dioxide. Through hybridization of carbon nanomaterial with new inorganic materials like zeolitic imidazolate frameworks (ZIF) and carbon nitride, we have shown that carbon nanomaterial composites can achieve new properties such as microporosity and photoexcited charge carriers, respectively. Combining these properties with those of carbon nanomaterials will benefit a variety of applications including chemical sensors, (photo)electrocatalysts, and energy storage devices, among others.

TABLE OF CONTENTS

LIST OF TABLES

LIST OF FIGURES

PREFACE

I would like to acknowledge and thank my research advisor, Dr. Alexander Star; my colleagues, both past and present; my collaborators, especially Dr. Dan Sorescu and Dr. David Finegold; and my committee members: Dr. Nat Rosi, Dr. Haitao Liu, and Dr. Götz Veser. They have all had a hand in forming my graduate study experience and the research presented in this document. I would also like to thank my parents; my siblings, Diane and Charlie; my friends, especially Rob, Todd, Daniel, Tom, Matthew, Bart, and Steve; my mentor, Dr. David Sanchez; and the Oratory. They have been exceptionally encouraging to me over these last 6 years. I dedicate this dissertation to BVM.

1.0 INTRODUCTION

1.1 CHAPTER PREFACE

Chemical gas detection is an important task for a variety of industries, occupations, and scientific fields. Each chemical gas detection application has its own requirements with regards to target analyte, limit of detection (LOD), sensitivity, selectivity, response/recovery time, size, and robustness, thus requiring sensor devices specifically suited for the given application. For some fields such as medical, military, and occupational safety, chemical gas detection can be a matter of life and death. Such motivation drives development of new sensor devices that improve upon the aforementioned performance parameters. This dissertation will focus solely on electrical transduction devices, which are the more common of the two primary transduction types; optical transduction devices will not be discussed.

Electrical sensor development can be divided into three facets: 1) sensing material or substrate, 2) sensor device architecture, and 3) data treatment. An example of new data treatment analysis is the use of multivariate analysis in gas sensor arrays (or e-noses), which has made chemical gas identification possible; however, quantification with these same arrays remains a challenge. This dissertation will not discuss novel data treatment. Many types of electrical sensor device architectures have been demonstrated including chemiresistors, chemical capacitors, chemical inductors, field-effect transistors (FETs), and electrochemical devices, among others.

This dissertation will focus on the development of new sensing materials that are tested within a chemiresistor device architecture. The basic design of a chemiresistor includes two metallic electrodes on a solid substrate (i.e. Si, paper, polymer, etc.), bridged by a sensing element or a network of sensing elements. A constant voltage is applied across the two electrodes while the current is simultaneously measured, thus allowing the output resistance to be plotted in real time. Substitution of different sensing elements in a chemiresistor device provides control over the sensor's selectivity and sensitivity.

The first section of this introduction will cover traditional gas sensors (both unselective and selective), the sensing elements used in these sensors, and the mechanistic models used to understand their response. The second section will introduce carbon nanomaterials (CNM), their electronic structure and electrical properties. Finally, the third section will introduce inorganic—CNM composites, synthetic strategies and characterization for inorganic—CNM composites, sensing mechanisms and characteristics of CNM-based sensors. All of these topics will serve as background to the research projects detailed in the following chapters.

Section 1.4.1 is adapted from a review article written by James E. Ellis and Alexander Star with permission from *ChemPlusChem* **2016**, *81*, 1248-1265. Copyright 2016 Wiley-VCH.

1.2 TRADITIONAL CHEMICAL GAS SENSORS AND THEIR MECHANISMS

Quantification and identification of a chemical gas target requires both sensitivity (response vs. concentration function) and selectivity (response only for a single gas). A non-selective gas sensor functions on a widely applicable principle such as ionization or thermal conductivity, which provides quantification without identification. However, certain non-selective sensors can

be selective for certain classes of compounds (e.g., organic compounds with high electronegative functionalities). These sensors are effective for applications in which the detection of a change in gas composition is important, but the identity of the gas composition itself is unimportant. In contrast, selective gas sensors require a direct interaction *via* adsorption with the sensing element, thus making the focus of development toward surface chemistry. The three broad categories of selective gas sensors include metal oxide-based sensors, catalytic wire sensors, and electrochemical sensors. Since these sensors typically involve a catalytic reaction occurring on the surface of the sensing element, sensor development can often benefit from heterogeneous catalysis development.

1.2.1 Non-selective gas sensors

Electrically transduced non-selective gas sensors include flame ionization and photoionization detectors (FID and PID, respectively) and thermal conductivity detectors (TCD). FID and PID rely on the ability of gases to ionize when exposed to an ionization source. TCD, on the other hand, relies on the thermal conductivity coefficient that is unique to each gas. These detectors are often coupled with gas chromatography (GC) columns in order to separate the gas composition into its individual components. While GCs can determine the number of gas components with a given composition, the technique cannot identify the components unless coupled to another instrument such as a mass spectrometer.

TCD is the most non-selective gas detectors since its operating principle is based on thermal conductivity rather than ionization potential. In a basic TCD set-up, a Wheatstone bridge circuit is utilized wherein one resistor leg (R_1) of the bridge is exposed to the sample gas environment while the other resistor leg (R_2) is exposed to a reference gas environment, typically

He. The other two resistor legs (R_3 and R_4) of the Wheatstone bridge are isolated. Whenever the gas environment across the sample gas resistor leg has a different thermal conductivity coefficient than helium, a resulting difference in the resistor temperature and thus resistance occurs. The voltage across the bridge (V_B) can be determined according to equation (1), where V_S is the source voltage of the circuit:

$$V_B = (R_1/(R_1+R_3) - R_2/(R_2+R_4)) * V_S \quad \text{(Eq. 1)}$$

A differential op amp connected to the bridges provides a V_{out} depending on the voltage difference between V_B and V_S. The advantages of TCD include its sensitivity toward all gases including noncombustible inorganic gases and their large linear dynamic range (~10^5). The disadvantages of TCD are its relatively poor sensitivity (~10^{-8} g solute/mL carrier gas) and the requirement of a reference gas, which makes portable TCD infeasible.

The operating principle behind PID and FID is the ionization of the sample gas and its subsequent collection at a charged electrode plate. The ionization sources for PID are gas discharge lamps equipped with filter windows; controlling the combination of fill gas and filter window allows an ionization potential between 8.4 eV and 11.7 eV to be selected. Gases and vapors with ionization potentials below the UV radiation source, which includes many volatile organic compounds (VOCs), will be ionized and converted into electrical current at the collector electrode; however, any gas with ionization potentials above the UV radiation energy will not generate a current. For example, methane has an ionization potential of ~12.5 eV;[1] therefore, no PID is capable of sensing methane at any concentration. FID is effective for difficult to ionize organic species like methane because most organic species pyrolyzed in an air-hydrogen flame will produce ions and electrons. However, neither PID nor FID is capable of detecting inorganic gases with high ionization energies, such as CO_2, CO, H_2O, and SO_x. The primary advantage of

PID over FID is the portability of the ionization source that allows PID to be standalone VOC sensors, while FID is limited to benchtop instruments since it requires a H_2 source for operation.

Non-selective gas sensors are ideal for detecting a change within a gas matrix; however, their reliance on a reference source (TCD) or H_2 source (FID) often limits their use to benchtop instruments, catalytic reactors, and other laboratory setting applications. PID instruments are used as portable VOC detectors, but their high power consumption and low selectivity (gases with ionization potentials below photon energy) limits their application to industrial safety. In order to achieve a higher degree of selectivity, new mechanisms that involve preferential surface adsorption and subsequent reaction are required.

1.2.2 Selective gas sensors

Selective gas sensors can be divided into three broad categories based on their operating mechanism: (1) metal-oxide based sensors, (2) catalytic sensors, and (3) electrochemical sensors. Figure 1.1 illustrates the mechanisms for each respective type of sensor using CO detection as an example.

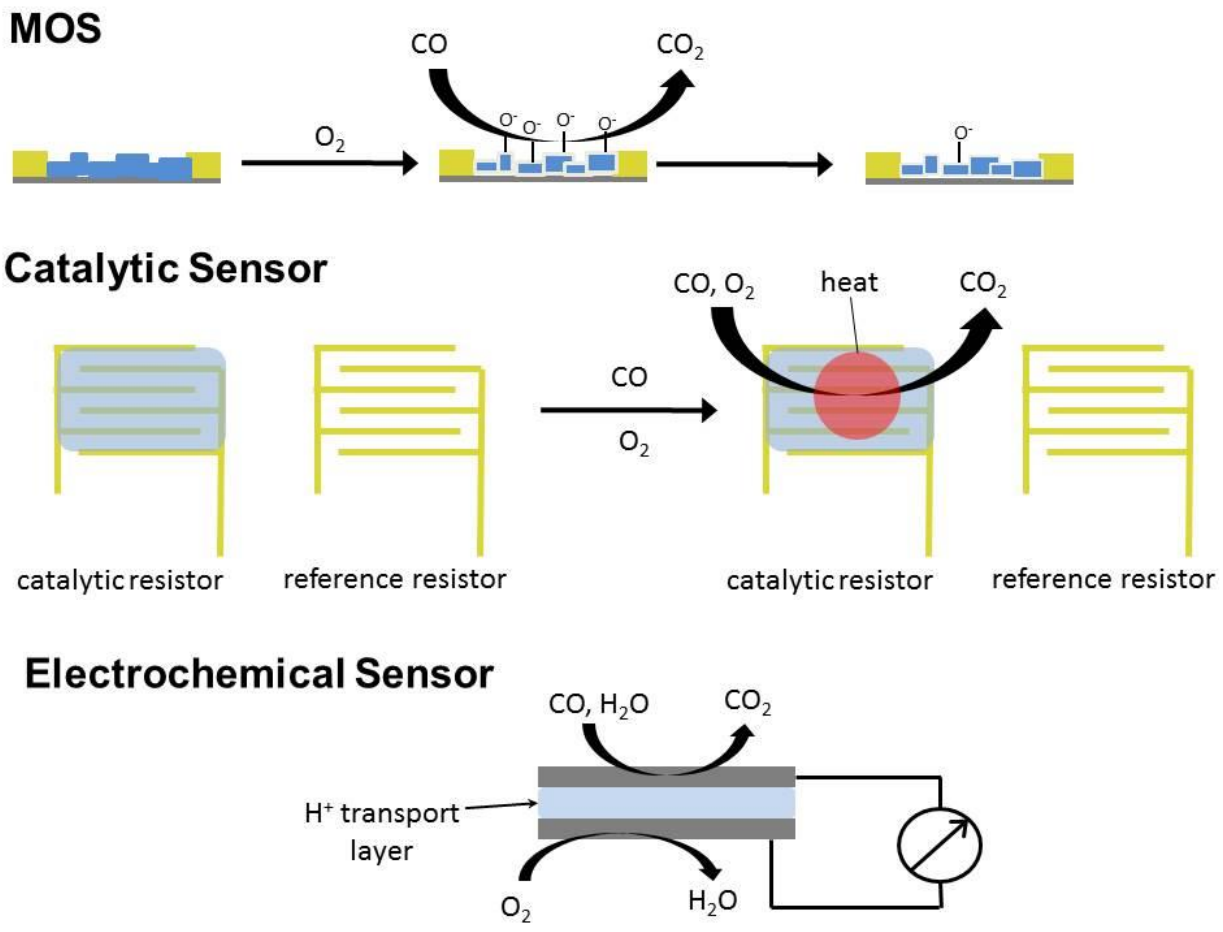

Figure 1.1 Schematic illustrations of three traditional selective gas sensors. Metal oxide sensor (MOS) (top); catalytic sensor (middle); and two-electrode electrochemical (bottom). All sensors are sensing carbon monoxide as an example of operation.

Metal oxide-based sensors (MOS) are commonly used to sense oxidizing (e.g., O_2, NO_x, etc.) and reducing gases (e.g., alcohols, NH_3, etc.). In 1962, Seiyama *et al.* reported a zinc oxide film that could detect noncombustible gases in air, while Taguchi in the same year patented a similar result for tin oxide films.[2] The resistance across thin films of semiconducting metal oxides is observed to change depending on whether the film is exposed to an oxidizing or reducing gas environment. Resistance change occurs across an n-type (p-type) metal oxide film because adsorption of O_2 (or other oxidizing gas) will create a depletion (accumulation) layer on the particles that compose the metal oxide film. These depletion (accumulation) layers will modulate the potential barrier at the grain boundary between metal oxide particles, thus affecting the overall resistance across the film. When exposed to reducing gases, these oxidizing species will react and desorb from the metal oxide particles resulting in a decreased space charge layer.

There are two proposed mechanistic models for how oxidizing gases may form space charge layers on metal oxide particles. The ionosorption model proposes that electrons are sequestered by oxidizing species adsorbing on the surface of metal oxides as negatively charged ions. While this model explains the necessity of high operating and the high sensitivity toward reducing gases, there exists very little *in situ*/operando spectroscopic evidence of such ionosorbed species on metal oxide sensors.[3] The oxygen vacancy model proposes that oxidizing species fill oxygen vacancies on the metal oxide surface, while reducing species create more oxygen vacancies. The modulation oxygen stoichiometry for a metal oxide may significantly affect its electronic structure. This model may explain the absence of ionosorbed oxygen species. Both the ionosorption model and the oxygen vacancy model have been cited exclusively to explain the sensitivity of indium oxide toward ethanol; wherein Guo *et al.* saw a decrease in sensitivity with an increase in initial oxygen vacancies, Seetha *et al.* observed the opposite

trend.[4-5] In either case, more *in situ* spectroscopic studies would benefit the theoretical understanding of MOS detectors.

There are three major variables that provide control over the selectivity of metal oxide-based sensors: (1) temperature, (2) metal oxide identity, and (3) dopants. Typically MOS detectors are operated between 100-600^{o}C; sensitivity is rarely observed below 100^{o}C, while particles begin to sinter above 600^{o}C. The effect of temperature has been correlated to the type of ionosorbed species on the surface of metal oxides. $O_2^-{}_{(ads)}$ is thought to only exist on the surface at low temperatures (<150^{o}C), while other ionosorbed species like $O^-{}_{(ads)}$ and $O^{2-}{}_{(ads)}$ only exist at high temperatures (>150^{o}C). While certain reducing gas species may react with $O_2^-{}_{(ads)}$, others may only react with more reactive species like $O^-{}_{(ads)}$ or $O^{2-}{}_{(ads)}$. The metal oxide identity plays an important role in sensor selectivity as well. While SnO_2 and 3d transition metal oxides are the most popular sensing elements for MOS detectors, there are also several demonstrated examples of mixed metal stoichiometry oxides such $LnCrO_3$ and $LnFeO_3$ (Ln = La, Pr, Nd, Sm, Eu, Gd, Tb, Dy, Ho, Er, Tm, Yb and Lu).[6] Each metal oxide shows its own unique affinity toward different target analytes.[7] In addition to the metal oxide itself, noble metal and main group element dopants have shown to greatly affect MOS selectivity. For example, SnO_2-Au is very sensitive toward acetone but not hydrogen sulfide, while SnO_2-$Sb^{III,V}$ is sensitive to hydrogen sulfide but not acetone.[8]

MOS detectors have benefitted from the development in nanomaterial synthesis.[9] Nanomaterials have much larger surface area to volume ratios than their bulk counterparts, such that the Debye screening length approaches the radius of the nanoparticle or nanowire. Reducing the size of metal oxide particles to the nanoscale will not affect selectivity, but should have a large effect on the MOS sensitivity.

The second type of selective gas sensor is the catalytic gas sensor, which is used to sense combustible gases. The working principle behind catalytic gas sensors is the exothermic combustion reaction catalyzed by the sensing element results in a temperature increase and a subsequent increase in sensor resistance. Most catalytic sensors are composed of metal wires or nanoparticle films that have a high affinity toward adsorbing combustible gases such as H_2, CO, or hydrocarbons. Some catalytic sensors are composed of metal nanoparticles incorporated in a metal oxide matrix, for example Au NP/Co_3O_4.[10] The metal oxide matrix provides oxygen for combustion while the metal NPs serve at the site of combustion. Other catalytic systems such as Pt-group metal catalysts are capable of splitting oxygen and do not require a metal oxide matrix.[11] The circuitry for catalytic sensors is similar to a TCD (see section 1.2.1), but unlike TCD, catalytic sensors do not require a constant flow of a reference gas across the reference resistor. In contrast to the operating principle being thermal conductivity, which is universal, the operating principle in catalytic sensors is combustion catalysis, which will only occur on the resistor with the deposited sensing element, and not on the reference resistor of the Wheatstone bridge.

The final type of traditional selective sensor is the electrochemical sensor. The challenge that presents itself with electrochemical sensors is creating small, robust, selective devices that are capable of performing common laboratory electroanalytical techniques like amperometry (and less commonly voltammetry). Electrochemical sensors are typically two electrode galvanic cells separated by a proton bridge. In ambient conditions (oxygen and humidity), no current is generated because no spontaneous redox pairs are present. However, in the presence of reducing gases, CO for example, a redox reaction occurs wherein CO is oxidized to CO_2 and O_2 is reduced to H_2O. Humidity as a proton source is crucial for the operation of electrochemical sensors. A

calibration curve can be constructed for electrochemical sensors since the current generated is proportional to the concentration of the reducing gas. Electrochemical sensors are not functional in applications where both the reducing and oxidizing gas species are variable. Functionalization of the electrode surface, as well as the incorporation of a third reference electrode, provides selectivity for electrochemical sensors. Surface functionalization provides kinetic enhancement of certain redox reactions over others. A three electrode electrolytic cell allows the sensing of non-spontaneous reducing gases since the potential at the electrode surface can be specifically tuned. While the use of a three-electrode cell provides more selectivity, it also significantly increases the power consumption as compared to the two electrode set-up.

PID, MOS, catalytic sensors, and electrochemical sensors are commercially applied as chemical gas sensors. Each sensor type has its own set of performance parameters, advantages, and disadvantages. For example, PID, MOS, and catalytic sensors have high power consumption because of the ionization source and microheaters, respectively. High power consumption requires a bulky battery and frequent recharging, which places limits on size reduction and sensor lifetime. In contrast, electrochemical sensors have less power consumption than MOS and catalytic sensors and are often more sensitive; however, their components are more expensive and less robust compared to other sensor types.

A solution to the high power requirements of traditional sensors is to decouple the receptor and transducer functions of the sensor across two different materials. Carbon nanomaterials have proven themselves to be excellent electrical transducers because of their semiconducting nature, high conductivity, and high surface area to volume ratio. While MOS requires high voltages and operating temperatures to transduce a chemical reaction into an electrical signal, carbon nanomaterials can sense the same target at room temperature and low voltages because of their sensitivity and high conductivity. Analogous to traditional sensor types, functionalization of carbon nanomaterial surfaces provides control over selectivity.

1.3 CARBON NANOMATERIALS

Carbon nanomaterials (CNMs) are a class of nanomaterials composed primarily of carbon atoms. When referring to CNMs, this dissertation will be referring to one-dimensional and two-dimensional sp^2-hybridized nanomaterials, namely carbon nanotubes (CNTs) and graphene, respectively; however, zero-dimensional sp^2-hybridized (e.g., fullerenes) and sp^3-hybridized CNMs (e.g., nanodiamonds) do exist and are commonly studied subclasses of CNMs. CNTs and graphene are significant for chemical sensing because of their high conductivity, semiconducting electronic structure, high surface area-to-volume ratio, and surface functionalization capability.

CNTs can either be multi-walled (MWCNTs) or single-walled (SWCNTs) in structure. SWCNTs can be between 0.4 to 3 nm in diameter and are either metallic or semiconducting in electronic structure; both diameter and electronic structure depend on the rolling vector or chirality, which will be discussed in section 1.3.1. MWCNTs can be thought as concentric SWCNTs and are always found to be metallic. Currently, mass production of CNTs has been

demonstrated with two techniques: arc-discharge method and chemical vapor deposition (CVD). Briefly, arc discharge method is where a high voltage between two carbon electrodes produces a bridging plasma that generates CNTs as a byproduct. Pressure, gas type, and electrode composition can affect the types and yields of CNTs generated. In a CVD synthesis, a carbon source gas such as methane is flowed across a metal-based catalyst substrate in a high temperature furnace. The carbon gas dissolves in the metal catalyst in the form of metal carbides and reforms into a CNM. CVD is commonly used to synthesize MWCNTs, SWCNTs, heteroatom-doped CNTs, and graphene. The synthesis of a single chirality CNT has not been performed; therefore, separation techniques have been investigated to separate semiconducting chiralities from their metallic counterparts.[12]

Graphene can either be synthesized by a bottom-up method (e.g., CVD) or prepared from a top-down method (e.g., mechanical exfoliation). The "scotch-tape method", which was used by Geim and Novoselov in their initial report on graphene, produces high quality sheets;[13] however, the dimensions of the sheets are small and variable, and the procedure is time-intensive. CVD can produce spatially large sheets of graphene, but they are often polycrystalline.[14-16] The relatively weak stacking forces of graphite allows for top-down mechanical exfoliation methods in the presence of intercalants to separate graphite into few- and single-layer graphene.[17] top-down production method begins with graphite to produce a graphene-like analogue called reduced graphene oxide (rGO). In this method, graphite is oxidized into graphite oxide, exfoliated into graphene oxide, and reduced (either chemically or thermally) into rGO.[18] This solution-based method is the most scalable; however, the resulting sheets are dimensionally heterogeneous and often contain oxygen functionalities left over from the reduction process.

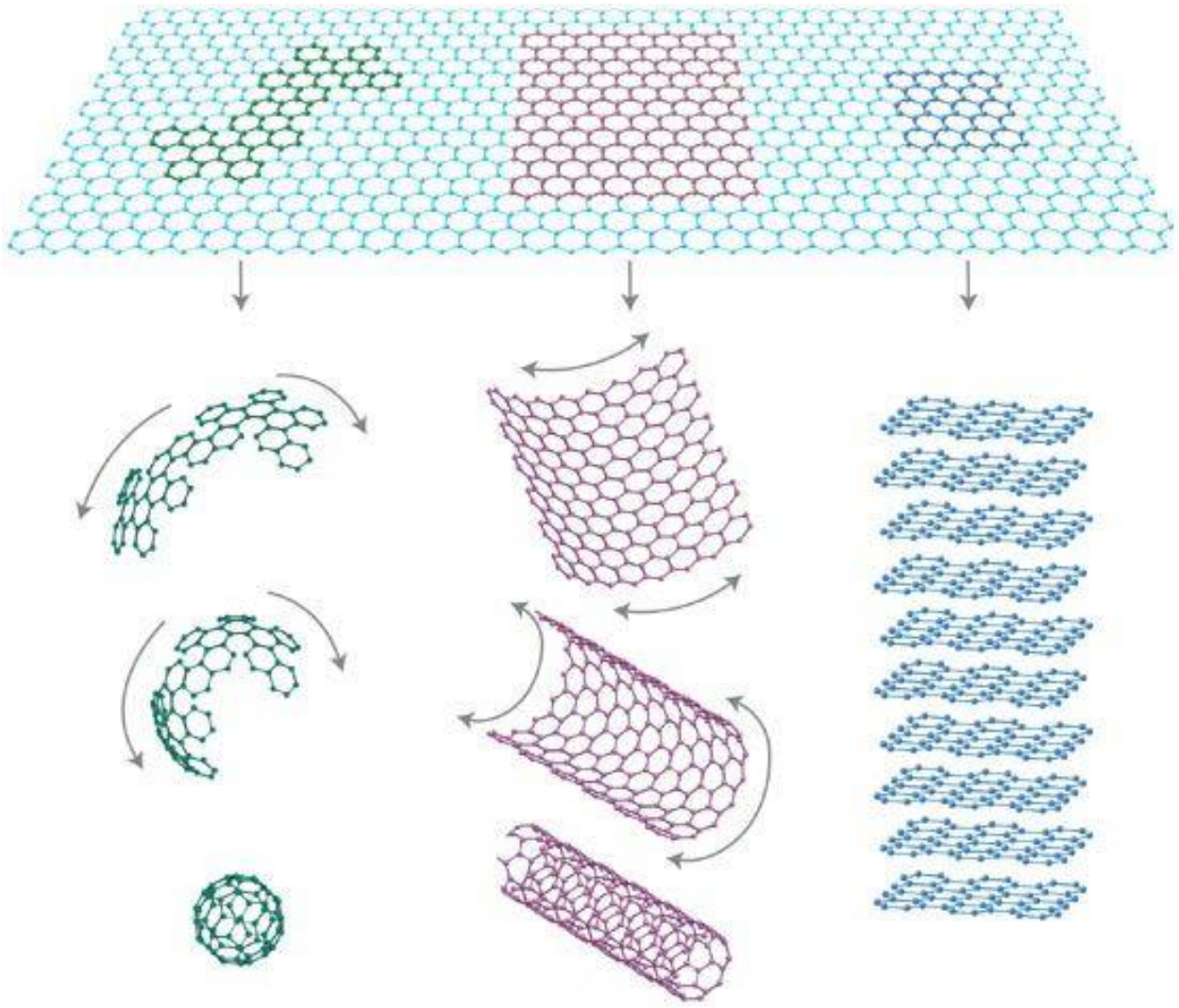

Figure 1.2 Graphene as building block for all graphitic carbon allotropes. A section of graphene can be rolled into a zero-dimensional (0-D) fullerene (left), a one-dimensional carbon nanotube (middle), or stacked to form three-dimensional (3-D) graphite. Reprinted with permission from reference [19]. Copyright 2007 Nature Publishing Group.

1.3.1 Electronic properties of CNM

Graphene has an exceptionally high electron mobility that ranges from at least 2,000 $cm^2/V{\cdot}s$ for freshly micromechanically exfoliated sheets to 200,000 $cm^2/V{\cdot}s$ for annealed and suspended graphene.[20] Moreover, hole mobility is approximately equal to electron mobility in graphene.[21] The work function of graphene is similar to graphite's (4.6 eV),[22] but can be substantially modulated with metal contacts.[23] Graphene has a unique electronic structure wherein the conduction and valence bands are symmetric cones that meet at a point, such that its Fermi level can be tuned with an electric field in a symmetrically ambipolar effect.[24] However, because of graphene's zero-bandgap and linear dispersion curve of electronic states, modulating the transport characteristics with an electric field to achieve non-linear effects is inefficient. For this reason, researchers have investigated methods to create small bandgaps in graphene. This search has led to the development of graphene analogues such as graphene nanoribbons and reduced graphene oxide.

Graphene nanoribbons were first theoretically described as a potential way to quantum confine graphene's 2D electron gas. It was predicted that graphene nanoribbons would either be metallic or semiconducting depending on whether their edge was zig-zag or armchair, respectively.[25] For armchair nanoribbons, the bandgap created is determined by the ribbon width and length.[26] Graphene nanoribbons have since been experimentally prepared by lithography, free ion beam, and ultrasonication.[27-31] The graphene nanoribbons prepared by Dai and coworkers achieved an on/off current ratio of 10^6 when incorporated into a field effect transistor (FET) device; however, mobility had decreased to around 200 $cm^2/V{\cdot}s$.[29] A covalent framework of graphene nanoribbons called nanoporous graphene has been prepared through organic synthesis and has remarkably demonstrated a bandgap of 1 eV.[32]

The introduction of sp^3 carbon defects into graphene is another method to create a bandgap. rGO is a graphene analogue that has a variable amount of sp^3 carbon domains across the basal plane and edge. Licea-Jiménez and coworkers found that the method and duration of chemical reduction used on graphene oxide affected the observed optical bandgap of the prepared rGO sheets.[33] rGO has a tunable bandgap between 0.2 and 2 eV depending on its level of oxidation.[34] In addition to tuning the bandgap, the work function of rGO can also be tuned depending on the reduction method and degree of oxidation. Tasis and coworkers demonstrated that rGO sheets reduced with hydrazine had a work function ranging from 4.2-4.5 eV while thermally reduced rGO sheets had a work function ranging from 4.5-5.5 eV.[35] rGO typically has a larger hole mobility than electron mobility; a reduction method using Na-NH_3 as the reduction agent was able to achieve an rGO material with a hole mobility of 123 $cm^2/V{\cdot}s$.[36]

One can visualize SWCNTs as a sheet of graphene rolled into a cylinder whereby the origin of the graphene sheet is connected to position L (Fig. 1.3); the lattice translation vector **L**, also called the rolling vector, can be defined as $\mathbf{L} = \mathbf{na} + \mathbf{mb}$, where **a** and **b** are the primitive translation vectors. The chiral angle, η, formed between the rolling vector, **L**, and the primitive vector, **a**, determines whether the SWCNT is zig-zag ($\eta = 0^o$), armchair ($\eta = \pi/6$), or chiral. Armchair nanotubes are always metallic, while zig-zag and chiral nanotubes may either be metallic or semiconducting. The primitive vector magnitudes determine the electronic structure wherein if $\mathbf{n} + \mathbf{m} = 3k$, then the CNT is metallic; otherwise it is semiconducting.[37] The bandgap of a semiconducting CNT may be 0.6 eV or greater and is inversely proportional to its diameter.[38] The carrier mobility of single-nanotube transistors has been reported to be >10,000 $cm^2/V{\cdot}s$;[39] however, CNT network transistors have demonstrated a field effect mobility of just 150 $cm^2/V{\cdot}s$.[40] SWCNTs display p-type behavior, wherein holes are the majority charge carrier,

in ambient conditions. Oxygen adsorption is believed to cause the p-doping of CNTs because annealing in vacuum is able to recover CNT's intrinsic ambipolar transfer characteristics.[41]

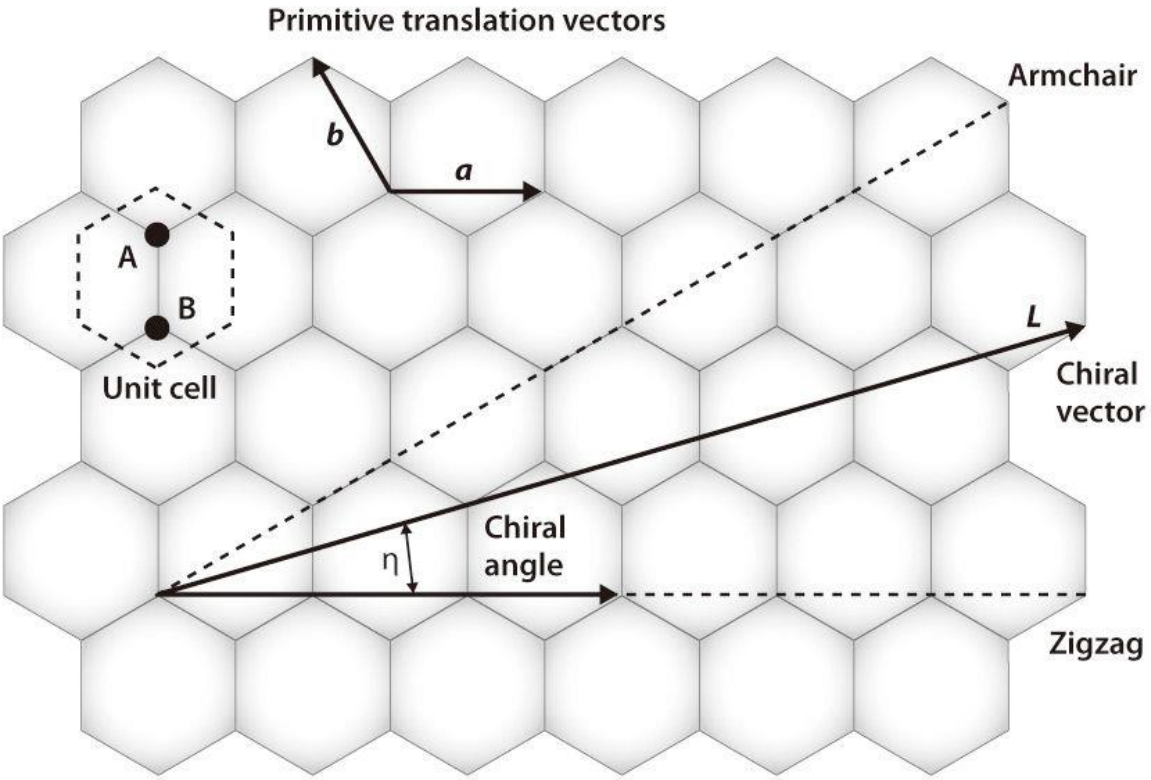

Figure 1.3 Carbon nanotube structure from graphene lattice. The hexagonal unit cell containing two carbon atoms (A and B), the primitive translation vectors (a and b), the chiral vector (L), the chiral angle (η), and the 0^o (zigzag) and 30^o (armchair) vectors. Reprinted with permission from reference [42]. Copyright 2009 Nature Publishing Group.

The work function of SWCNTs has been determined to be 5.05 eV using ultraviolet photoelectron spectroscopy (UPS).[43] When contacting a CNT to a metal contact, the CNT's band edges will bend to match its Fermi level with the metal's Fermi level. A large Fermi level mismatch between a CNT and a metal contact will result in a large Schottky barrier, which impedes the flow of charge across the barrier. For this reason, metal contacts used in CNM-based devices are typically Au, which has a work function closely matched to CNTs (5.1 eV). Modulation of the metal contact's work function through molecular adsorption can alter the Schottky barrier and affect the resistance across the CNT/metal interface; this is a potential sensing mechanism for CNM-based sensors and will be discussed further in section 1.4.3.

1.4 INORGANIC—CNM GAS SENSORS

1.4.1 CNM functionalization with inorganic receptors

CNM functionalization *via* covalent, noncovalent, and defect chemistry provides a variety of chemical handles on the CNM sidewall, basal plane, or edges where molecular receptors can be appended.[44-45] CNMs have been hybridized with inorganic compounds for a variety of applications including photocatalysts, supercapacitors, photonics, and chemical sensors, among others.[46] For CNM-based sensing materials, there are certain considerations to take into account when functionalizing the CNM with receptors. These include 1) electron delocalization, 2) coverage density, and 3) stability. High electron delocalization across the receptor and transducer near the Fermi level is important for chemisorption or reactions that occur on the receptor's surface to affect the transducer. The coverage density of the receptor on the CNT surface is

directly related to the sensitivity of the sensor toward the gas analyte. For covalent functionalization, a balance between functionalized coverage density and pristine sp^2-hybridized network must be struck to achieve optimum sensitivity. Stability of the receptor in different physical and chemical environments is important for a robust and re-useable sensor. For example, a breath sensor must function in a range of working temperatures, as well as an oxidative and humid environment. If the chemical linker or intermolecular force attaching the receptor to the transducer is disturbed by these conditions, a decrease in performance will be observed. Blondeau has outlined the advantages and disadvantages of different CNM functionalization methods for enhancing the surface sensitivity and selectivity.[47]

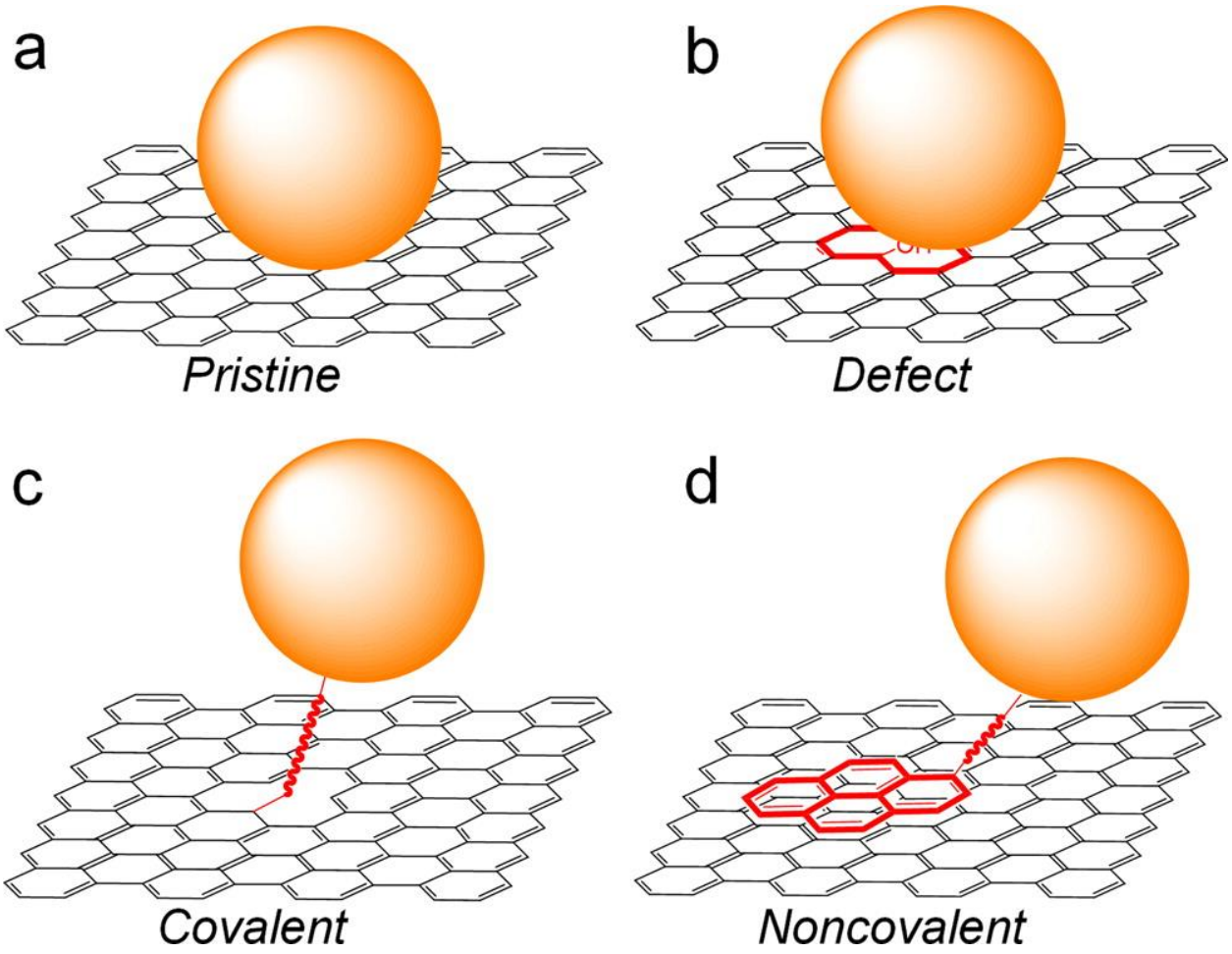

Figure 1.4 Schematic illustrations of four different types of inorganic—CNM interfaces. (a) A pristine interface between a nanoparticle (NP) and graphitic surface; (b) A NP attached to a defect site on a graphitic surface; (c) a covalent attachment of a NP to a graphitic surface through a linker molecule; (d) a noncovalent attachment of a NP to a graphitic surface through a linker molecule. Reprinted with permission from reference [48]. Copyright 2013 American Chemical Society.

Pristine CNMs consist of a hexagonal network of sp^2-hybridized carbon atoms, making chemical linkage between a molecular receptor and a CNM difficult. rGO has residual oxygen defects present even after the reduction step, so an additional oxidation step is unnecessary. However, as-synthesized CNTs are entirely sp^2-hybridized carbon. Defect chemistry seeks to create a chemical handle on a CNT structural defect that can eventually serve as a chemical linker between the receptor and the CNT (Fig. 1.4b). Oxidation *via* acid treatment is a popular functionalization approach since it creates many hydroxyl and carboxyl moieties along the sidewall and ends, achieves aqueous dispersibility depending on the degree of oxidation, and can be completed in a one-pot batch synthesis.[49] Carboxyl groups can serve as covalent linkers through amidation and esterification reactions, while oxygen moieties in general serve as nucleation sites for metal oxide (or hydroxide) clusters. Acid oxidation proceeds by creating defect sites such as pentagon-heptagon pairs and Stone-Wales defects at high strain points along the CNT sidewall, which are then subsequently consumed by the oxidative agent.[50] Oxygen plasma treatment has emerged as an alternative method for CNT oxidation.[51] A disadvantage of this method is the disturbance of the conjugated sp^2 network, which can have adverse effects on electron-transport properties. Vázquez *et al.* have explored ball-milling as a method to make SWCNTs dispersible in water while avoiding sidewall defects common in acid oxidation.[52] In the same paper, these water-dispersible SWCNTs were shown to be functionalized *via* cycloaddition reactions. Jeon *et al*. demonstrated a ball-milling procedure to halogenate the edges of graphene; Cl, Br, and I edge functionalized graphene nanoplatelets were the produced material.[53]

An example of covalently functionalized CNTs *via* oxidized defects is Hongjie Dai and coworkers' work using oxidized CNTs to synthesize strongly coupled inorganic-nanocarbon

hybrid materials.[54-55] CNTs are oxidized by a modified Hummers' method wherein purified CNTs are dispersed in heated, concentrated sulfuric acid with addition of sodium nitrate and potassium permanganate, followed by treatment with hydrogen peroxide. This treatment produces oxygen functionalities that serve as nucleation sites for metal salts or complexes. Wang *et al.* produced a $Ni(OH)_2$/CNT hybrid material used as a battery cathode by nucleating nickel acetate at the oxygen defect sites of oxidized CNTs, followed by a hydrothermal treatment.[56] Another example of this synthetic method is Liang *et al.*'s synthesis of CoO/CNT hybrid material as an oxygen reduction catalyst.[57] This two-step synthetic procedure produces strongly-coupled inorganic/nanocarbon hybrid materials with drastically enhanced charge transfer compared to the physical mixture of the two components.

Other types of covalent functionalization include fluorination, cycloaddition, radical addition, and nucleophilic and electrophilic additions (Fig. 1.4c).[58-59] A small catalogue of cycloaddition reactions have been applied to CNTs, including 1,3 dipolar cycloaddition, as well as carbene and nitrene addition. Hu *et al.* observed that dichlorocarbene addition to CNT sidewalls formed cyclopropane rings with the functionalization amount ranging between 12 and 23%.[60] Holzinger *et al.* first described the addition of nitrenes to SWCNTs to form aziridene rings.[61] The degree of nitrene functionalization as well as variety of side group on the resulting aziridene ring has improved in recent years.[62-63] 1,3 dipolar cycloaddition with azomethine ylides has been a widely used method of covalent functionalization due to its highly adaptable side group chemistry.[64] Since azomethine ylides are synthesized by condensing aldehydes with alpha-amino acids, the side groups on the precursors can contain moieties, such as protected amines, for further functionalization once attached to the CNT.[65] Furthermore, it has been shown that ferrocene covalently attached to a SWCNT *via* 1,3 dipolar cycloaddition of an azomethine ylide

can transfer its charge into the π-system of the SWCNT.[66] The disadvantages of organic covalent functionalization are the large amounts of solvent needed to disperse CNT bundles into individual tubes and the long reaction times required. To work around these issues, researchers have employed noncovalent functionalization as a method to disperse CNTs, as well as to serve as chemical linkage points for receptor addition.

Noncovalent functionalization of CNTs relies on intermolecular interactions such as π-π stacking,[67] electrostatic,[68] and van der Waals interactions (Fig. 1.4d).[69] Unlike covalent functionalization, noncovalent modifications do not disturb the sp^2 carbon network of the CNT by creating sp^3 carbon scattering sites, thus maintaining the electron transport properties of the pristine tube.[70] Of the available noncovalent interaction options, π-π stacking is highly utilized due to the degree of functionalization, the strength of the intermolecular interaction, and the variety of side groups available to attach to the polycyclic aromatic molecule, typically pyrene. π-π stacking has been used to attach quantum dots (QDs),[71] biomolecules,[72] and metal nanoparticles[73] to CNTs. The choice between covalent and noncovalent functionalization depends on the subsequent chemical modifier and the end to which the composite material will be applied. If the composite will be used at high temperatures or sintering of nanoparticles is a risk, covalent functionalization is the better option. However, if the pristine optical or electrical properties of the CNT must be maintained, noncovalent functionalization would be the preferred method. Noncovalent functionalization is commonly used to append biomolecules such as proteins to the CNT surface for the purpose of biosensing.[74]

Van der Waals heterostructures (vdWH) are composite structures between a two-dimensional nanomaterial and other nanomaterial (0-D, 1-D, or 2-D) that are held together by weak van der Waals forces (Fig. 1.4a). This strategy allows composite structures with disparate

lattices to be matched, which is important for creating different types of heterojunctions between metals, semiconductors, and insulators. vdWH transistors have been assembled between a variety of transition metal dichalcogenides (TMDs), a type of 2-D semiconductor, and graphene.[75] When two semiconductors are stacked on each other, interesting heterojunctions may result depending on the initial positions of the valence and conduction bands. For example, if the conduction band minimum (CBM) and valence band maximum (VBM) of semiconductor 1 is with the energy bandgap of semiconductor 2, a straddling heterojunction will form that promotes charge transfer between the two layers (Fig. 1.5). Staggered heterojunctions, where the CBM of semiconductor 1 is found in the energy gap of semiconductor 2 and the VBM of semiconductor 2 is found in the energy gap of semiconductor 1, are often used to form Z-scheme photocatalysts for water splitting.

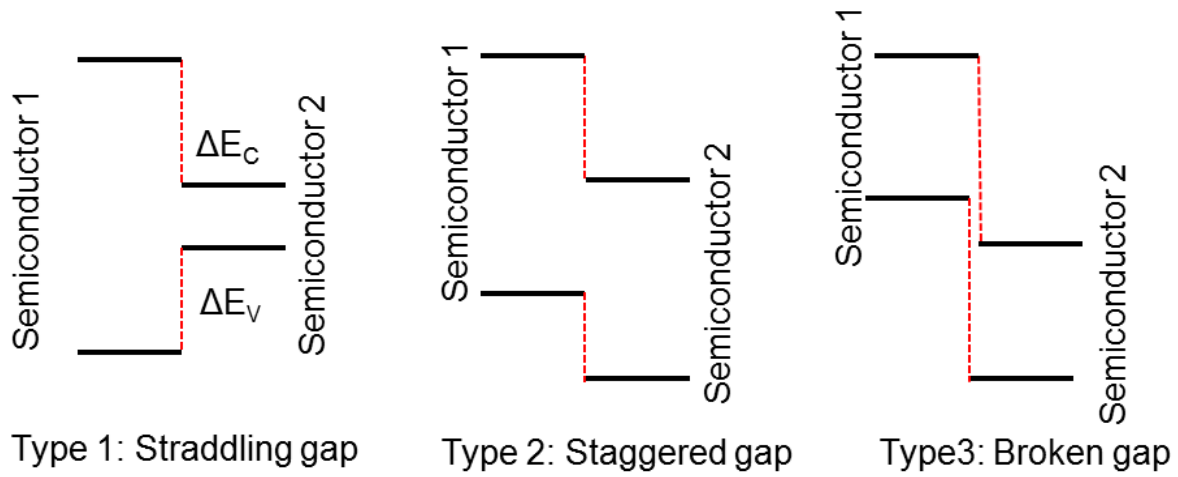

Figure 1.5 Schematic illustrations of semiconductor heterojunction types. Straddling gap (left), staggered gap (middle) and broken gap (right).

1.4.2 Characterization of inorganic—CNM composites

Due to changes in electrical, optical, chemical and structural characteristics, it is common to use a wide-array of techniques to characterize inorganic—CNM composites. A combination of microscopy, spectroscopy, and electrical measurements are performed to analyze such composites and correlate the chemical and physical structure with the relevant application mechanism.

1.4.2.1 Electron Microscopy

Electron microscopy is the primary method to study physical features of nanomaterials. Both scanning electron microscopy (SEM) and transmission electron microscopy (TEM) provide resolution down to the nanoscale realm, allowing for dimensional and morphological analysis of the composites. With high-resolution transmission electron microscopy (HRTEM), resolution down to the atomic scale is achievable, allowing individual atoms of a crystalline solid to be visualized. While both SEM and TEM use electron guns and field emission as the illumination source, the mechanism of image formation and contrast differs. For SEM, the electron beam is condensed to a very small area and scanned back and forth over the surface of an object. The reflected electrons caused by elastic back-scattering or inelastic scattered secondary electrons are detected, providing a magnified image with topographical details of the sample surface.[76] For TEM, the electron beam is transmitted through the sample, carrying diffraction information of the specimen in the forward-scattered wave, which is detected with a CCD detector. Unfortunately, the diffraction information of the transmitted electron waves is lost due to nonlinear propagation through the objective lens. The contrast seen in a TEM image is caused by three factors: (i) local strain & defects, (ii) crystal potential or atomic distribution of the sample,

and (iii) mass thickness or atomic number contrast.[77] In the case of HRTEM, the diffracted waves that forward-scatter from the sample are focused into a single point by the objective lens and form a diffraction pattern on the back focal plane. To see the HRTEM image in real-space, an inverse Fourier transform is applied to the diffraction pattern detected on the back focal plane. While normal bright field TEM images will provide information on a sample's morphology, HRTEM is needed to provide electron diffraction information of a crystalline sample.

1.4.2.2 Spectroscopy

Spectroscopy is a powerful characterization tool wherein electron or photon radiation probes matter. Information directly or indirectly gleaned from spectroscopic experiments include molecular vibrations (Fourier transform IR, Raman), electronic transitions (UV-vis absorption, fluorescence), electron binding energies (X-ray photoelectron spectroscopy, electron energy loss spectroscopy), among others. In addition to the probed interaction, different spectroscopic techniques can either analyze a sample as a surface or bulk. Since inorganic—CNM composites are commonly used in surface applications such as heterogeneous catalysis and sensing, surface spectroscopic techniques are more relevant for characterization.

Electron spectroscopy, especially X-ray photoelectron spectroscopy (XPS), is perhaps the most effective characterization technique for inorganic—CNM hybrids. Both a qualitative and quantitative analysis technique, XPS uses monochromatic X-radiation to study the surface (1 to 5 nm depth) of a solid. The theoretical principle behind XPS is that an incident beam of high-energy, monochromatic X-radiation will excite and eject core electrons of atoms in its path. The XPS detector detects counts of electrons versus electron kinetic energy. The kinetic energy, E_k, of an ejected electron will vary depending on its original binding energy, which allows XPS to plot electron counts versus electron binding energy, according to equation 1.

$$E_b = h\nu - E_k - w \quad \text{(Eq. 2)}$$

The incident, monochromatic radiation is *hv* and the work function is *w*. The binding energy peaks of core electrons for different elements vary dramatically and can typically be resolved, with some exceptions. XPS survey scans scan over 800 eVs and are used for elemental identification and quantification of the sample's surface atoms. High-resolution scans around 25 eVs can provide information on the oxidation states and chemical structure for all atoms of a given element on the sample's surface. The binding energy of an atom's core electron can shift depending on the number of valence electrons present, thus allowing the oxidation state of that atom to be identified. Another factor that can affect the shifting of core electron binding energy is the chemical structure of the molecule or sample under analysis. For example, the 1s electron of an ester's carbonyl carbon will have a lower binding energy than the 1s electron of the aliphatic carbon due to the electron withdrawing effect of the oxygen atoms. This insight allows one to roughly determine the ratio of functionalities through deconvolution of a given peak.

In addition to surface spectroscopic techniques, Raman spectroscopy holds an important role in the arsenal of CNM characterization techniques due to resonantly enhanced Raman scattering intensity for 1D CNMs, which provides detailed vibrational information on CNTs. This resonance enhancement factor in CNTs is due to "quantum confinement of the phonon states into van Hove singularities."[78] Raman spectra for CNMs show three prominent scattering features: the G band (tangential modes), the D band (disorder-induced feature), and G' band (D band overtone). By using the intensity ratio D/G, one can infer the degree of defects present on the CNM. A D/G ratio of zero would be a completely pristine graphitic material; however, as discussed above, defects can act as sites for preferential nucleation and covalent bonding.

Though not technically spectroscopy, but rather a form of crystallography, powder X-ray diffraction (PXRD) is a common bulk characterization method for metal oxides, CNMs, and metal oxide/CNM hybrids. PXRD probes materials of a periodic structure with monochromatic X-radiation to determine the structural phases of the material. Periodic structural phases will have periodic electron density that can constructively diffract X-rays of given incident angles. The diffraction pattern generated by PXRD allows for easy identification of a metal oxide, or any other crystalline solid. For graphitic structures like few-layered graphene or graphene oxide, the d-spacing between graphitic layers can be calculated by applying Bragg's law to the material's (002) peak. Since basal plane defects and intercalation can cause further spacing between graphitic layers, this is a popular application of PXRD. Bragg's law is

$$n\lambda = 2dsin\theta \quad \text{(Eq. 3)}$$

where n is an integer, λ is the radiation wavelength, d is the atomic spacing between crystal plane, and θ is the scattering angle. The advantages of PXRD are ease of preparation and non-destructiveness, while the disadvantage is the need for relatively large sample amounts (>5 mg for high S/N).

1.4.3 Sensing mechanisms of CNM-based sensors

The sensing mechanism of a CNM-based sensor can be categorized into three broad categories: 1) intra-CNM mechanisms where the analyte interacts directly with the CNM to affect its electrical properties, 2) inter-CNM mechanisms in which the analyte affects the interface or contact point of CNMs, and 3) Schottky barrier modulation in which the interface between the CNM and the metal electrode is affected by the analyte. These three mechanisms are illustrated

for a CNT-based chemiresistor system in Figure 1.6. In mechanistic investigations of CNM sensors, the process of elimination is often used to determine which category is responsible for the observed response. For example, the CNT sensor response toward ammonia was investigated by fabricating devices that either had the CNT/metal contacts or the CNT conduction channel passivated.[79-80] A response only from the CNT/metal contact-passivated device would indicate an intra-CNT mechanism; in contrast, a response only from the channel-passivated device would indicate a Schottky barrier modulation mechanism.

Intra-CNM mechanisms (Fig. 1.6c) include doping, defect-inducing, or charge pinning events that occur between an analyte molecule and a CNM. Doping or charge transfer events change the charge carrier concentration of the CNM, while charge pinning affects the CNM's charge carrier mobility. Defect-inducing events can change either concentration or mobility or both. Under ambient conditions, CNMs are p-type because of oxygen adsorption; therefore, p-doping should further increase CNM hole conductance and n-doping should decrease hole conductance.[81] Doping of CNMs can be observed in FET experiments, wherein p-doping shifts the FET transfer curve toward negative voltages and n-doping has the opposite effect. CNM doping can also be observed through Raman spectroscopy. P-doping (n-doping) causes a blueshift (redshift) in the CNM G-peak.[82] Doping is a common sensing mechanism between CNMs and polar analytes, and has been observed in both single channel and CNM network devices.[83]

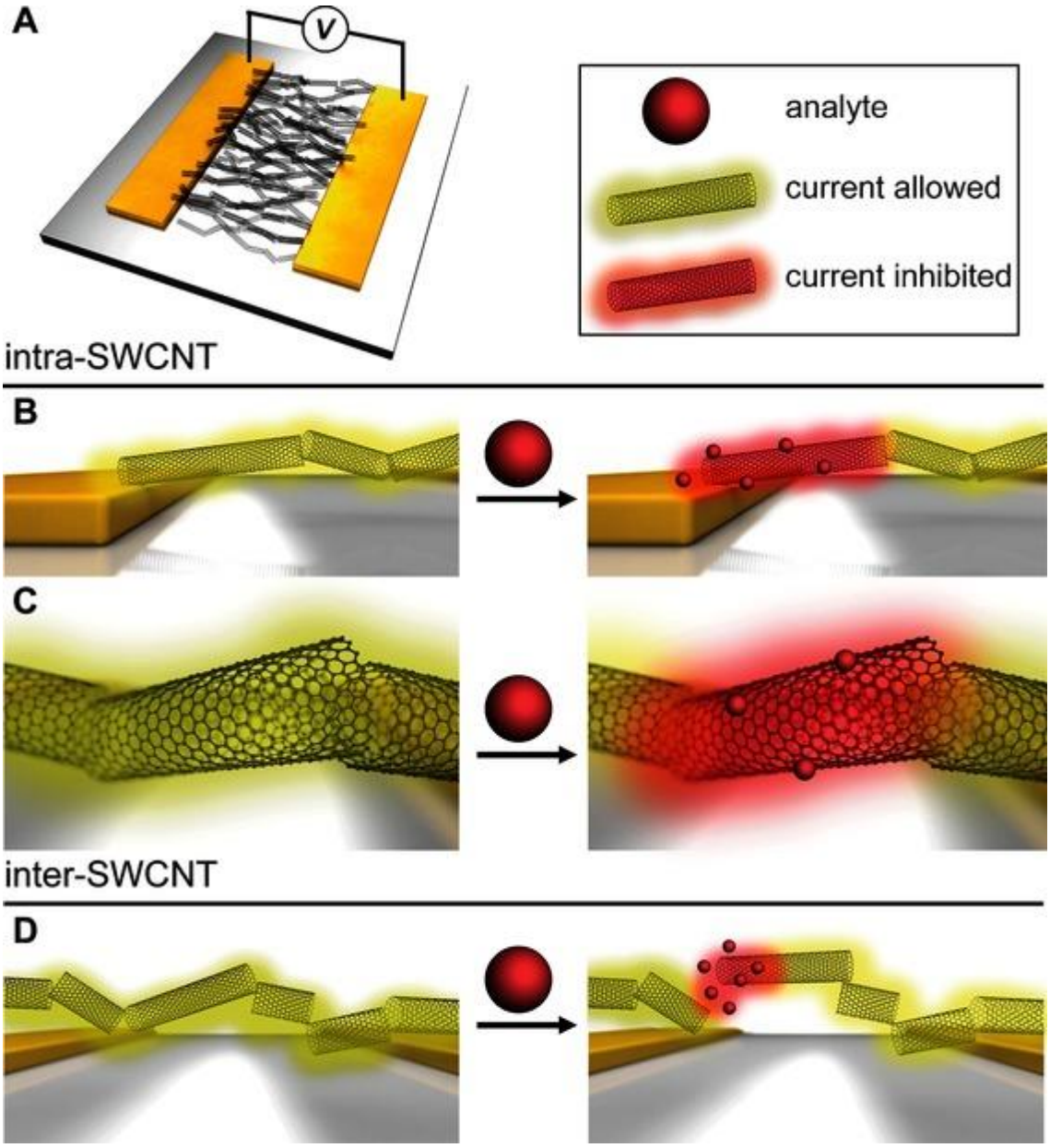

Figure 1.6 Schematic illustrations of SWCNT chemiresistor sensing mechanisms. (a) A SWCNT network chemiresistor; (b) Schottky barrier modulation at the SWCNT—metal electrode interface; (c) intra-SWCNT response mechanism; (d) inter-SWCNT response mechanism at the SWCNT—SWCNT interface. Reprinted with permission from reference [84]. Copyright 2015 Wiley-VCH.

In network CNM devices, conductance is often limited by charge tunneling at the CNM contact points. The probability of charge tunneling at these contact points exponentially decreases as the distance between CNMs increases.[85] Inter-CNM mechanisms (Fig. 1.6d) proceed in one of two ways: 1) the analyte increases the inter-CNM distance by either causing a surrounding matrix/polymer to swell or filling the interstitial space itself, thus decreasing conductance; or 2) the analyte decreases the inter-CNM distance by degrading the surrounding matrix/polymer, thus increasing the conductance. The first type of inter-CNM mechanisms is suited for non-polar analytes that are unable to directly interact with CNMs. For example, Wei *et al.* demonstrated a CNT network coated in a thin polymer film that was capable of sensing cyclohexane because of cyclohexane's ability to dissolve into the polymer film and cause swelling.[86] The second type has been utilized by Swager and coworkers to create target-specific dosimeters. In their work, semiconducting SWCNTs wrapped by a metallosupramolecular polymer displayed an irreversible increase in conductance that was related to the amount of nerve agent exposure.[87] This response was caused by the degradation of the metallosupramolecular polymer when exposed to the nerve agent. Inter-CNM sensing mechanisms are typically only applicable for CNT network devices because of their many sensitive CNT-CNT contact points; graphene or rGO network devices have larger sheet overlap contact points that are more difficult to disturb.

Schottky barrier modulation (Fig. 1.6b) occurs when the target analyte strongly adsorbs on the metal electrode of the device and causes a shift in the metal's work function. In a metal-CNM Schottky barrier, the valence and conduction band edges of the CNM bend in order for its Fermi level to match the metal's work function. For p-type CNMs, a shift of the metal's work function toward vacuum will increase the CNM's hole conduction, while a shift away from

vacuum will decrease hole conduction (increase electron conduction). Schottky barrier modulation has been used to describe the sensing mechanism of CNT-Pd electrode device sensitivity toward H_2.[88] The work function of Pd matches well with SWCNT Fermi such that transport across the contact is barrier-less; however, when H_2 adsorbs onto Pd, the barrier shifts and a detectable decrease in conductance is observed.

1.4.4 Sensing characteristics of CNM-based sensors

The parameters of performance for a CNM-based sensor are determined from the sensing response curve (Fig. 1.7). The sensing response curve plots the electrical signal of the CNM sensor (Either resistance, conductance, or current for chemiresistors) versus time. Response time and recovery time can be measured directly from the sensing response curve. Minimization of response and recovery time to seconds is often important for real world applications. The gradual incline or decline of the sensor baseline curve, drift, is a negative artifact of CNM-based sensors. Drift has been attributed to movement of deposited CNMs, Joule heating, and the electromotility of ions, among other causes. Minimization of drift is another important development for real world application of CNM-based sensors. Hysteresis is a difference in the sensor response curve when the gas exposure concentrations are increasing versus decreasing. A calibration plot (response vs. analyte concentration) can be constructed from the sensing response curve, which provides important performance parameters such as sensitivity, dynamic range, and limit of detection. Sensitivity of the sensor is determined by the slope of the calibration plot. Selectivity is determined by constructing calibration plots for other potentially confounding gases and comparing the slope of the target analyte to the slope of other gases. A sensor response can either be reversible, semi-reversible, or irreversible. For most applications, a sensor must be reversible;

however, irreversible sensors have been successfully applied as gas dosimeters.[87] For effective gas sensors, characteristics of merit such as sensitivity, selectivity, and short response/recovery time should be optimized, while negative characteristics such as drift, hysteresis, and irreversibility should be diminished.

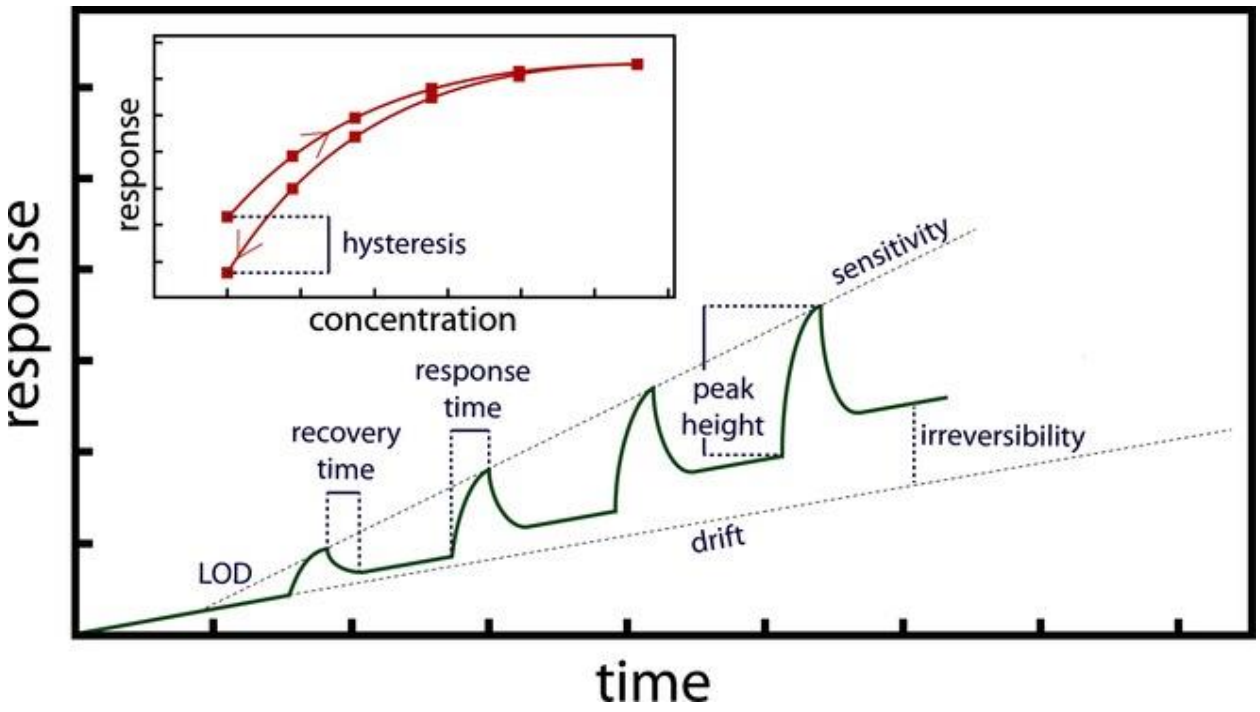

Figure 1.7 Graphical representation of a sensing response curve. An example of a sensing response curve highlighting different sensor characteristics such as limit of detection (LOD), recovery/response time, drift, sensitivity, hysteresis, and irreversibility. Reprinted with permission from reference [84]. Copyright 2015 Wiley-VCH.

2.0 INDIUM OXIDE—SINGLE-WALLED CARBON NANOTUBE COMPOSITE FOR ETHANOL SENSING AT ROOM TEMPERATURE

2.1 CHAPTER PREFACE

Parts of the text and figures in this chapter were published in The Journal of Physical Chemistry Letters, and have been reprinted with permission from *J. Phys. Chem. Lett.* **2015** DOI: 10.1021/jz502631a.

List of Authors: James E. Ellis, Uri Green, Dan C. Sorescu, Yong Zhao, and Alexander Star

Author Contributions: JEE, UG, and AS designed the experiments. JEE and AS wrote the manuscript. JEE and UG performed the experimental work and DCS performed the computational modeling. YZ took the high-resolution transmission electron microscope image.

2.2 INTRODUCTION

For chemical sensor development, new materials that are rugged, selective, responsive to low concentrations of chemical analytes, and require low power to operate are much sought after in many applications, including medical, security, energy, and automotive areas.[89] In these applications chemical sensors are required to satisfy two general functions: 1) a receptor function and 2) a transducer function.[90] Traditionally, 3d transition metal oxides are most commonly used as chemiresistor sensing substrates due to their selectivity toward oxidizing and reducing gases and large responses to low gas concentrations.[91-93] However, metal oxide-based sensors require the metal oxide component to serve as both the receptor and transducer. While metal oxide films are highly effective at adsorbing and interacting with chemical species at their surface, they require high temperatures, large voltages, and expensive semiconductor parameter analyzers to transduce the surface chemical interaction into a detectable electrical signal.

Due to exceptionally large charge carrier mobility (~79,000 $cm^2/V{\cdot}s$), semiconducting carbon nanotubes (CNTs) are ideal transducers for chemical sensing applications.[94] In contrast, the electron mobility of an indium oxide thin film, a common ethanol sensing substrate,[95-96] is three to four orders of magnitude smaller than the mobility of semiconducting CNTs.[97] This disparity in charge carrier mobility has led chemical sensor development to separate the receptor function and transducer function of the sensor into individual components of hybrid composites. In metal oxide/CNT hybrid composites,[98-100] the metal oxide performs the receptor function when interacting with gases that have large adsorption energies to its surface, while semiconducting CNTs serve the transducer function by turning the chemical interaction into an observable electrical signal due to a corresponding change in electrical resistance.

In terms of sensing, physical phenomena such as surface adsorption and charge transfer are related to a sensor's selectivity and sensitivity, respectively.[3] To understand why metal oxides may selectively sense one gas over another, it is necessary to study the morphology of the given oxide and to evaluate the electronic modifications induced upon adsorption of different gas species on that oxide's surface. For hybrid sensors such as metal oxide/CNT composites, it is important that the electronic states near the Fermi level are delocalized across both the receptor and transducer. Electron delocalization between the surface and transducer allows for charge acceptance or donation from gas adsorption to affect the sensor's electrical response.

For the case of In_2O_3/CNT composites,[101-102] the n-type oxide transfers electrons into the p-type CNTs[103] upon hybridization,[104] behavior that is similar to p-n junction ethanol sensors made with n-type In_2O_3/p-type NiO nanostructures.[105] Yet for all metal oxide-based sensors, elevated temperatures and oxidative environments are needed to create ionosorbed oxygen species (O_2^-, O^-, O^{2-}), which are necessary to make the oxides sensitive to gas adsorption.[106] Investigation of the sensing response and mechanism of In_2O_3/CNT toward ethanol at room temperature under non-oxidative conditions may illuminate alternative directions for sensor development as well as provide fundamental insight into the mechanism of this and other hybrid metal oxide materials like SnO_2/CNT[107-108]

2.3 EXPERIMENTAL SECTION

Synthesis of In_2O_3/SWCNT: Oxidized SWCNTs (ox-SWCNTs, containing surface oxygen functional groups between 1.0 and 3.0 atomic %) were purchased from Carbon Solutions, Inc. and used as received. The growth of the In_2O_3 crystalline structure on the surface of the

individual SWCNTs was achieved through a sol-gel synthesis approach, as illustrated in Figure 2.2 through a reaction with indium hydroxide in basic pH. The indium hydroxide solution was prepared by dispersing $InCl_3$ (Sigma-Aldrich, 10 mg, .005 mmol) in aqueous ammonia (1.5 mL, 28-30 wt% NH_3) solution. This solution is slowly added (over an hour) to ox-SWCNTs (P3-SWCNT, Carbon Solutions Inc., 0.5 mg) sonicated in ethanol (17 mL), and stirred for an additional hour. The solution was dialyzed in water overnight. The dialyzed solution was filtered and the solid was collected. The growth of the crystalline structure of the In_2O_3 was controlled by utilizing the furnace of a thermo-gravimetric analyzer (TGA) for the annealing process. This was achieved by monitoring the thermo-gravimetric profile of samples at constant heating and nitrogen flow rates (5 ^oC/min, 100 ml/min), and terminating the sequence at selected points.

Material characterization: Transmission electron microscopy (FEI Morgagni, TEM), high-resolution TEM (JEOL JEM-2100F, HRTEM), and scanning electron microscopy images (Phillips XL30 FEG, SEM) illustrated the morphology of this ox-SWCNT@In_2O_3 hybrid material. Using X-ray diffraction (Bruker D8 Discover, GADDS Detector, XRD) the crystallinity of the resulting nanostructures generated *via* this method was further confirmed. DRIFTS (Shimadzu IRPrestige-21, Pike Technologies Easidiff DRIFTS accessory) and XPS (Escalab 250 XI Thermo Scientific XPS) confirmed the presence of hydroxy groups on the In_2O_3 surface. For XPS, the sample surface was cleaned with Ar ion etching to remove any hydrocarbon contamination.

Gas sensing experiments: Gas sensing experiments were performed using Si chips fabricated in-house, and connected to 40 CERDIP packages with Au wires. Each Si chip

contained 4 devices with interdigitated gold electrodes. In_2O_3/SWCNT solution (1 mg/ml in DI water) was dropcasted on a single chip (3 µL, solvent was allowed to evaporate on a 120 ^oC hot plate), placed on a test board (bias voltage: 500 mV), and sealed in a Teflon chamber. Using a Keithley Dual SourceMeter 2602 and Keithley Switching Matrix 708A, which allows 4 data outputs simultaneously, changes in electrical conductance were collected with Zephyr data-acquisition software (http://zephyr.sourceforge.net). Two gas flow controllers allowed the gas environment over the chip to be manipulated. For every experiment, ten minutes of 300 sccm dry N_2 (Matheson Tri-gas) was flowed over the chip to expel the sealed Teflon chamber of O_2. Afterwards, acetone (20 ppm in dry N_2, Matheson Tri-gas) or ethanol (200 ppm in dry N_2, Liquid Technology Corp.) was flowed at a given concentration for a two minute burst, and allowed to return back to baseline in dry N_2 for three minutes. This process was repeated so that six different, increasing concentrations of acetone or ethanol were flowed over the same chip for a single run.

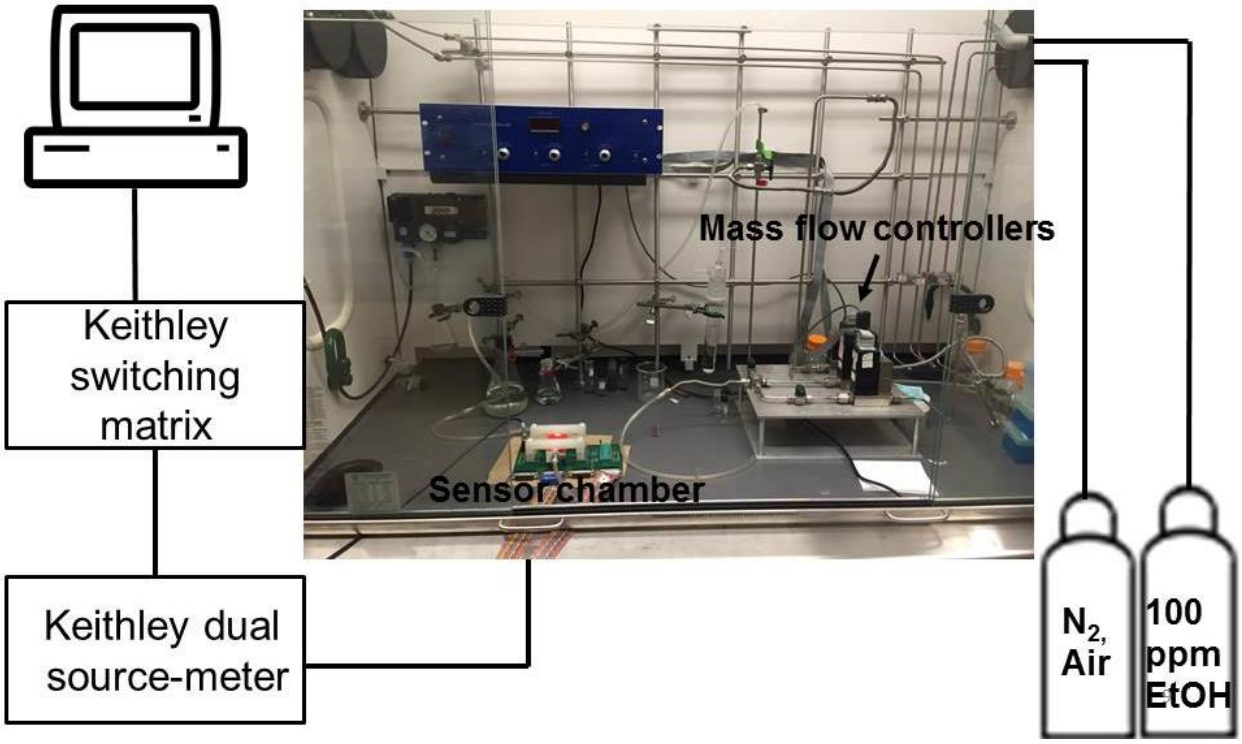

Figure 2.1 Schematic illustration of the gas sensing apparatus used in gas sensing experiments. For research done in other chapters, the apparatus is the same except for the change in background and analytic gas cylinders.

2.4 RESULTS AND DISCUSSION

2.4.1 Synthesis and characterization of In_2O_3/SWCNT composite

A sol-gel synthetic strategy was used in this work to achieve a core-shell morphology In_2O_3/SWCNT composite. SWCNTs were oxidized with nitric acid to provide functionalities such as carboxyl and hydroxyl groups on the CNT's outer wall for indium clusters to nucleate (Fig. 2.2a). Indium salts, such as indium nitrate or indium chloride, were ripened in basic solution to yield indium hydroxide clusters.[109] After dialysis, the gel was collected, air-dried, and simultaneously calcined and characterized with a thermogravimetric analyzer (TGA). The advantages of using TGA for the calcination include: (i) it allows for N_2 (non-oxidative) environment so that SWCNTs are not oxidatively-modified, (ii) heating gradient can be controlled, and (iii) loss of mass can be measured.

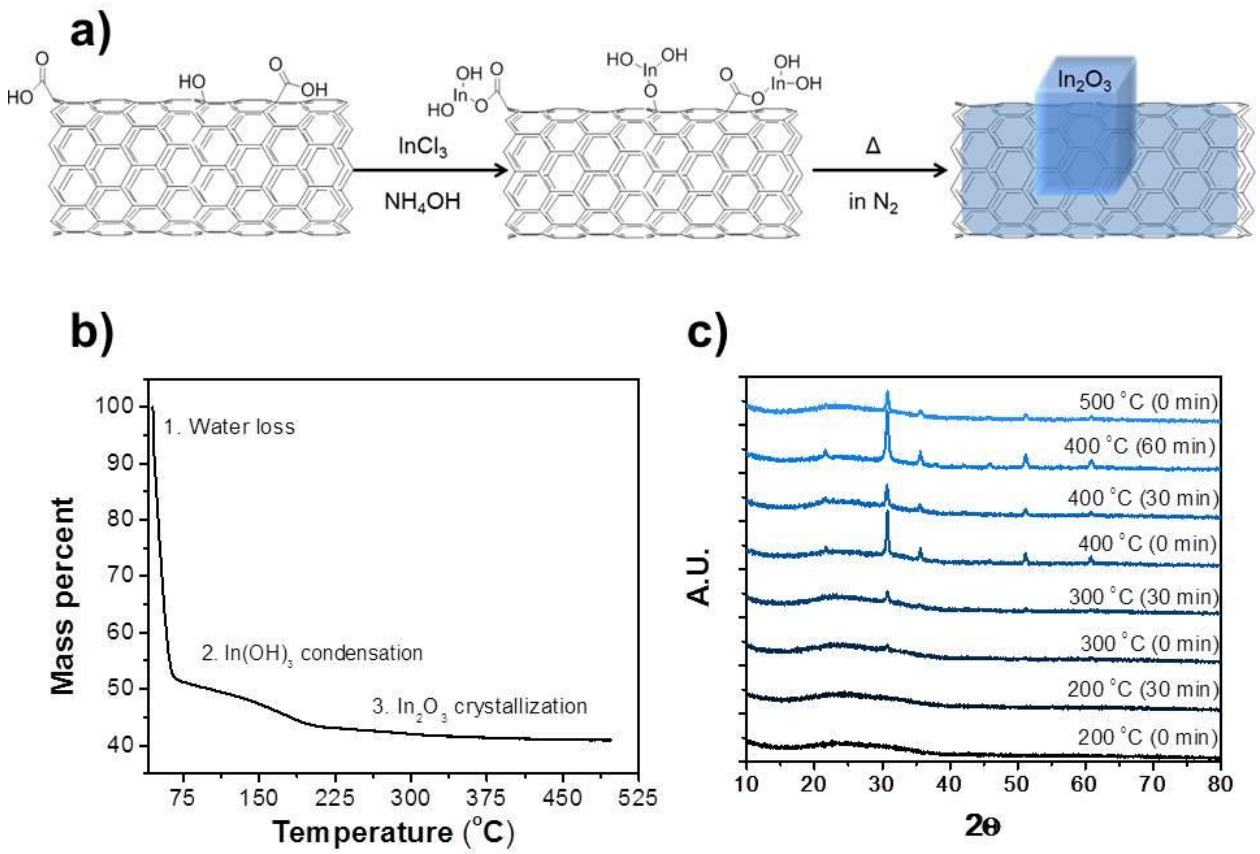

Figure 2.2 Synthesis of In_2O_3/SWCNT composite. (a) Schematic illustration of the sol-gel procedure used to synthesize In_2O_3/SWCNT composite; (b) TGA curve of In_2O_3/SWCNT composite showing the characteristic mass loss during the annealing procedure; (c) XRD patterns of different annealing conditions for In_2O_3/SWCNT.

The TGA curve (Figure 2.2b) has three distinct slopes, which correspond to (i) evaporation of solvent (25-80 ^{o}C), (ii) dehydration of $In(OH)_3$ (80-200 ^{o}C), and (iii) crystallization of amorphous In_2O_3 to cubic In_2O_3 (200-500 ^{o}C). The material was characterized with TEM at three different points of the TGA curve. At the 200 ^{o}C point (Fig. 2.3a), the indium shell is condensed around the SWCNT, but is not yet crystalline in nature. With longer calcination times at elevated temperatures, the indium oxide phase condenses onto the ox-SWCNTs and evolves from purely amorphous In_2O_3 to crystalline In_2O_3 (Fig. 2.2c). At the 400 ^{o}C point (Fig. 2.3b), the indium oxide shell is condensed around the SWCNT and distinct crystalline nanoparticles are visible in the TEM image. SEM characterization was performed on this calcined composite, confirming that the majority of CNT surface area is surrounded by In_2O_3 nanoparticles (Fig. 2.3c). HRTEM of this material shows In_2O_3 nanoparticles attached above a bundle of SWCNTS (Fig. 2.3d). The crystalline lattice for the nanoparticle displays a d-spacing of approximately 0.3 nm, which corresponds with cubic In_2O_3 (222) phase. This calcination-dependent crystallization can be observed by the gradual appearance of cubic indium oxide XRD peaks as the calcination condition approaches 400 ^{o}C (Fig. 2.2c). The close association of crystalline In_2O_3 with a bundle of SWCNTs allows for rapid charge transfer during exposure to organic vapors, while the exposed SWCNTs in this material are able to form Ohmic contacts with each other. However, the composite material at the 500 ^{o}C point begins to become disassociated from itself. At high temperatures, the carboxyl groups may disassociate from the CNT defects, thus detaching the indium oxide domain from the CNT. Using computational means, we simulated nucleation of In_2O_3 clusters on oxidized SWCNTs to better understand the growth mechanism.

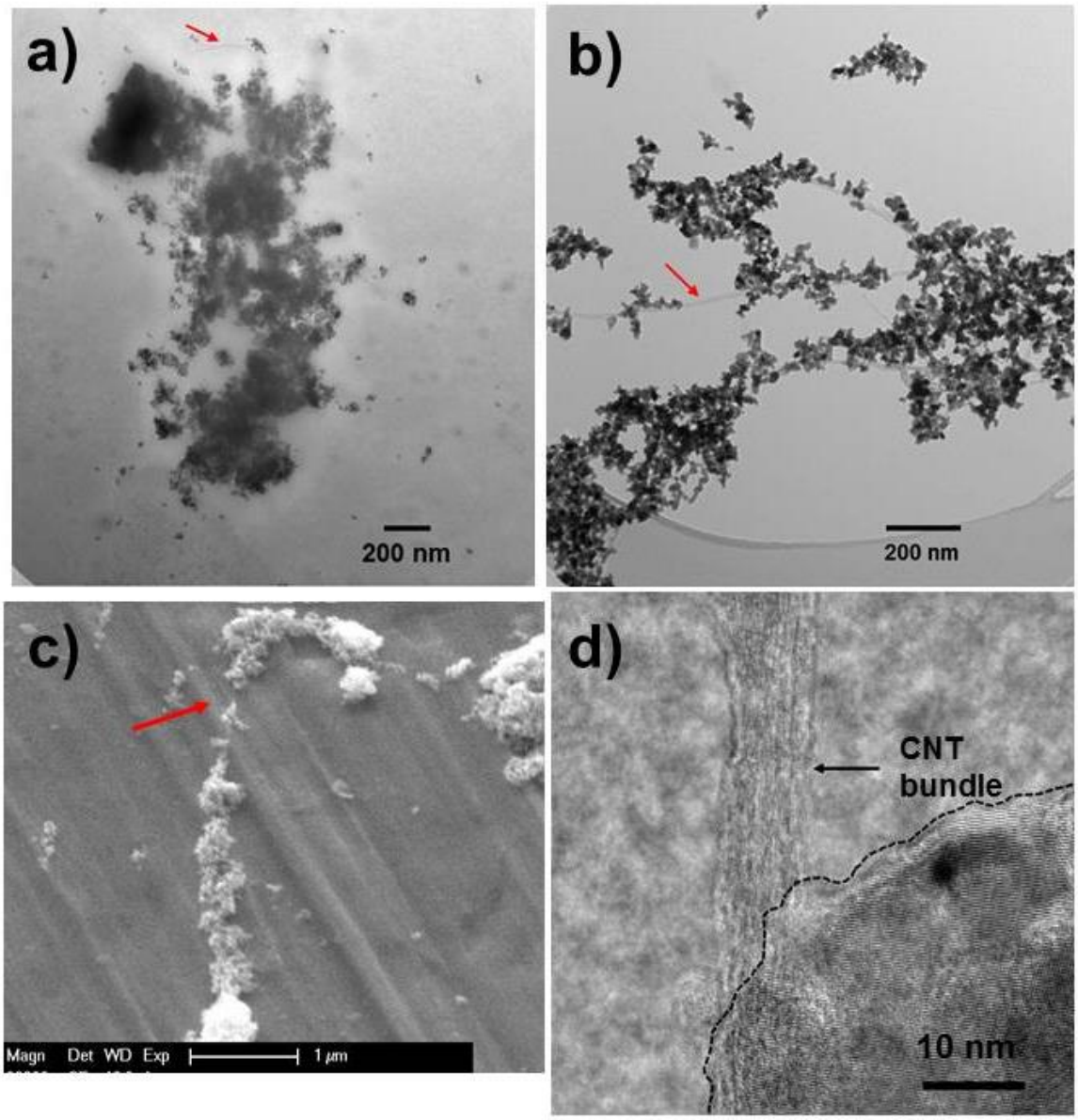

Figure 2.3 Morphology of In_2O_3/SWCNT composite. (a) TEM image of In_2O_3/SWCNT calcined at 200 °C; (b) TEM image of In_2O_3/SWCNT calcined at 400 °C; (c) SEM image of In_2O_3/SWCNT calcined at 400 °C; (d) HRTEM of In_2O_3/SWCNT calcined at 400 °C.

2.4.2 Modeling the Indium Oxide—SWCNT Interface at Defect Sites

To model our experimental In_2O_3/SWCNT system, a (14,0) CNT was constructed with two carboxyl groups located on either a Stone-Wales (SW) defect or an octagon-pentagon (OP) defect (Fig. 2.4); both defects are common to oxidized SWCNTs. It was calculated that an $(In_2O_3)_8$ cluster will adsorb to these sites and form a C-O-In bond at an adsorption energy of 56.3 kJ/mol (for SW defect) or 59.1 kJ/mol (for OP defect). The adsorption of the $(In_2O_3)_8$ cluster on carboxylated CNT takes place with a net charge transfer from the oxide to the carbon nanotube. The composite CNT/COOH/$(In_2O_3)_8$ system is effective in interacting and stabilizing molecules such as ethanol or acetone. For both ethanol and acetone, molecular adsorption takes place at indium atom sites with formation of an In-O bond. For the CNT with SW defect, adsorption energies of 19.4 kcal/mol and 18.2 kcal/mol were found for ethanol (Fig. 2.4a) and acetone, respectively. The corresponding values in the case of the CNT with OP pair defect are 23.7 kcal/mol for ethanol (Fig. 2.4d) and 23.3 kcal/mol for acetone. In the case of molecular adsorption, similarity in the bonding type also leads to close values for the corresponding binding energies of ethanol and acetone molecules.

It can be observed from the charge difference maps (Fig. 2.4b, f) that charge is transferred from the adsorbate molecules to the oxide cluster, which is important to the sensing mechanism discussed later. Another important aspect that can be gleaned from computational study of this composite material is its electronic properties. The localized densities of state (LDOS) for each component of the composite and the total DOS can be calculated for both the SW defect and the OP defect (Fig. 2.4d and h, respectively). Looking at the total DOS, the electronic changes indicate the presence of a semimetal or metal system with important electronic peak distributions. The charge densities corresponding to the states at or just above the

Fermi level show that the states are delocalized both on the oxide cluster and on the CNT surface (Figure 2.4c and g), which will contribute to this hybrid system's increased sensor performances.

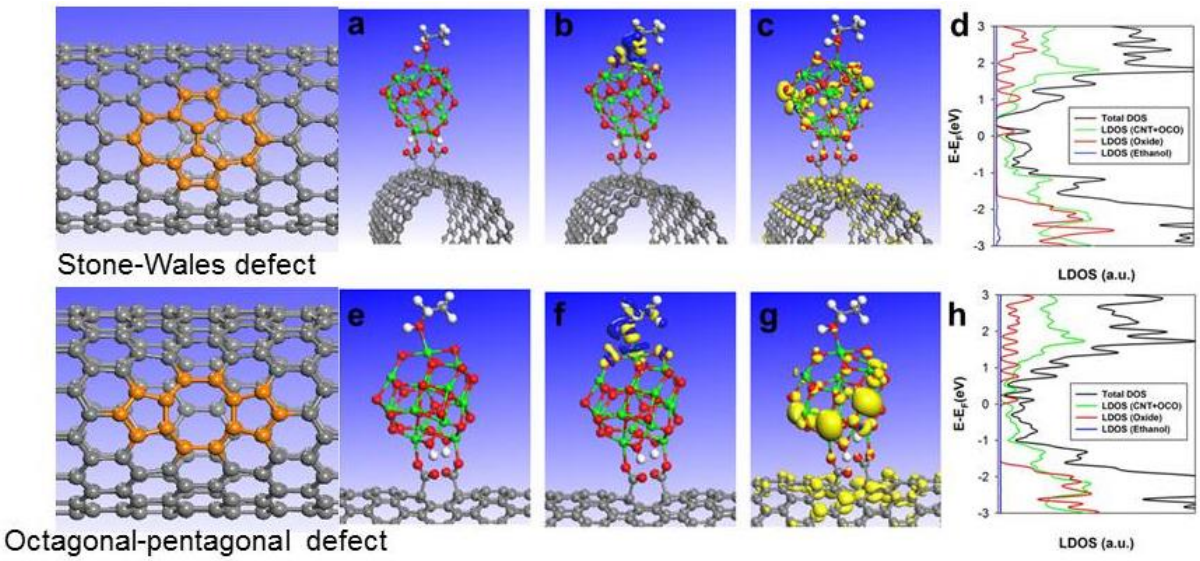

Figure 2.4 Representative adsorption configurations of ethanol on a hybrid $(In_2O_3)_8$ cluster- carboxyl-SWCNT with various defects. Top panels (a-d) illustrate the results for SWCNT with a Stone-Wales defect while bottom panels (e-g) present the case of SWCNT with an octagon pentagon pair defect. C atoms are grey, In atoms are green, O atoms are red and H atoms are white. Panels b) and f) represent the charge difference maps for ethanol adsorbed on the respective hybrid oxide-carboxyl-SWCNT systems. The indicated isosurfaces correspond to values of 0.015 $e^-/Å^3$ (yellow) and -0.015 $e^-/Å^3$ (blue). Panels c) and g) illustrate the partial charge density corresponding to the electronic bands situated at and immediately above the top of the valence band. The isosurface of 0.010 $e^-/Å^3$ is shown in both these two cases. In panels d) and h) the total density of states and its projections on the individual SWCNT, oxide and ethanol atoms are shown.

2.4.3 XPS Investigation of the In_2O_3/SWCNT Composite

XPS was performed on both bare oxidized-SWCNTs and In_2O_3/SWCNT composite calcined at 400 ^oC. The purpose of XPS was to confirm both the presence of oxygen moieties on the SWCNTs, and the presence of hydroxyl and oxygen vacancies on the In_2O_3 surface. The presence of adsorbed contaminants can skew the actual surface composition of the material, so a seven-second burst of Ar^+ plasma was applied to each sample to etch the contaminants off the surface. The survey scan of oxidized SWCNTs shows that only carbon and oxygen is present, and oxygen accounts for 4 atomic percent. A high-resolution scan of the O1s peak shows that hydroxyl and carboxyl groups are present on the oxidized SWCNT in approximately a 1:1 ratio. The survey scan of the 400 ^oC calcined In_2O_3/SWCNT composite shows the presence of carbon, indium, and oxygen with an In to O ratio of 2:3.13 (Fig. 2.5a). However, a high-resolution scan of the O1s peak shows that the surface oxygen atoms are not entirely composed of In_2O_3 lattice oxygen atoms (529.5 eV), but also of chemisorbed oxygen (530.8 eV) and hydroxyl oxygen (531.8 eV) (Fig. 2.5b). These binding energy values are taken from Gu *et al.*'s XPS study of cubic In_2O_3.[95] A mechanism elucidating the sensitivity of crystalline indium oxide towards ethanol *via* the oxidative mechanism was recently detailed by Hess and coworkers.[96] Their study suggested that, at 190 ^oC, ethanol is oxidized to adsorbed acetate or acetaldehyde by indium oxide, thus releasing electrons into the conduction band, and consequently decreasing the resistance. It is likely that the sensing mechanism observed with In_2O_3/SWCNT (*vide infra*) is similar to that described by Hess, but whereas they saw a decrease in resistance, we observe an increase in resistance (decrease in conductance). An increase in resistance is due to charge transfer between reduced In_2O_3 and p-type SWCNT. Yi and coworkers[104] showed *via* C_{1s} binding energy shifts that charge is transferred from In_2O_3 into SWCNTs. Hydroxy groups on the surface

of the In_2O_3, as seen with O_{1s} XPS, are capable of oxidizing adsorbed ethanol. The loss of hydroxy groups from the In_2O_3 surface creates oxygen vacancies, injecting free electrons back into In_2O_3 conduction band.

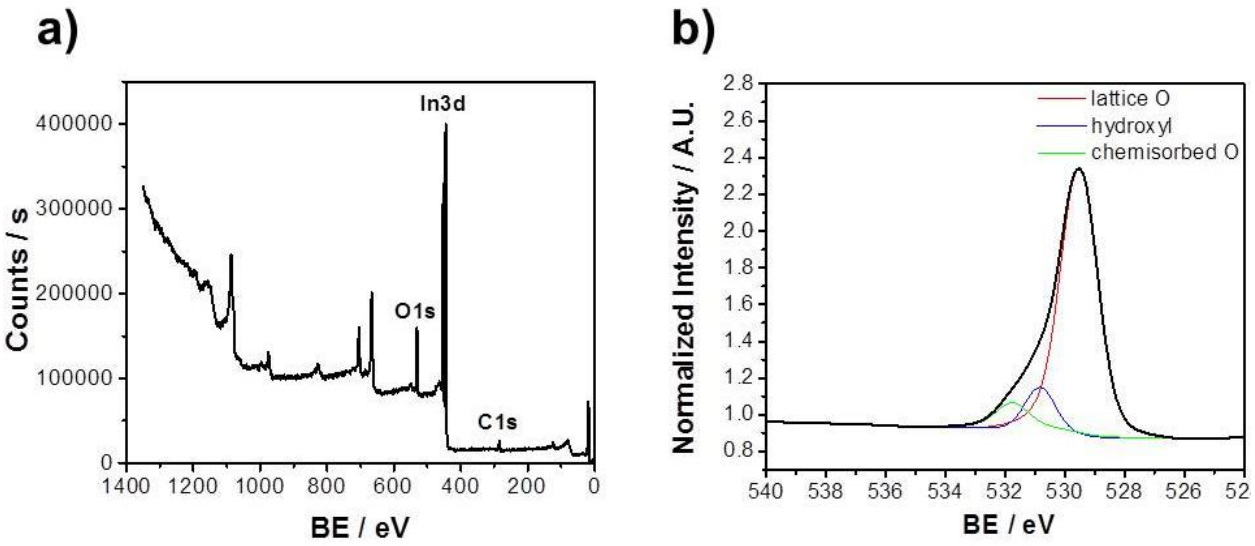

Figure 2.5 XPS of In_2O_3 composite. (a) Survey spectrum of In_2O_3/SWCNT composite; (b) high-resolution O_{1s} spectrum of In_2O_3/SWCNT (black curve) deconvolved into three different oxygen moieties: lattice oxygen (red curve), hydroxyl (blue curve), and chemisorbed oxygen (green curve).

2.4.4 In_2O_3/SWCNT Sensor Response toward Ethanol and Acetone

The sensor and its room temperature sensitivity toward acetone and ethanol vapors are presented in Figure 2.7. The sensor is composed of four interdigitated electrode pair devices with a layer of In_2O_3/SWCNT material deposited *via* drop cast method (Figure 2.6). Sensing experiments are performed in dry N_2, in which the sensor is exposed to six two-minute bursts of diluted organic vapors of increasing concentration (Figure 2.7a, b). Each burst of organic vapor is separated by three-minutes of dry N_2 flow to allow for baseline recovery. It is observed that the conductance baseline in dry N_2 drifts downward at a rate of ~4 μS/min. The gas flow for sensing experiments is kept at a constant rate of 300 standard cubic centimeters per minute (sccm). Both acetone and ethanol demonstrate a two-stage profile in their chemiresistor signals. The first-stage, which occurs within the first minute of vapor exposure, appears to be a linear response to the vapor concentration while the second is possibly saturation affected. The response and recovery times for both organic vapors are consistent for an hour, and likely longer. To account for the inherent noise in conductance measurements, a range of ± three standard deviations of the blank signal ($3s_{bl}$) , in this case dry N_2, was added to the graphs (dashed lines in Figure 2.7a, b). The linear first-stage signals for the three lowest acetone concentrations (0.5, 0.75, and 1.25 ppm) are below the limit of detection and are not included in Figure 3g, since they are within $3s_{bl}$ of the initial conductance (G_i).

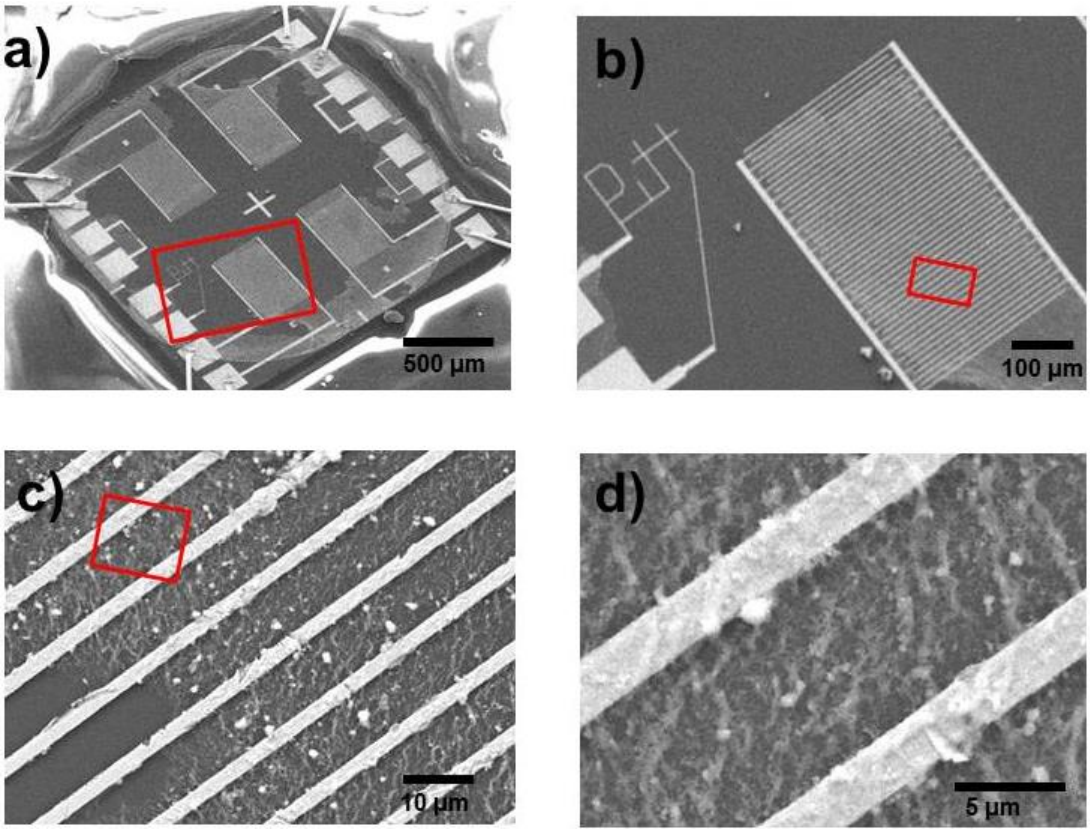

Figure 2.6 Chemiresistor chip at different magnifications after dropcasting In_2O_3/SWCNT. (a) SEM image of chemiresistor chip showing all four interdigitated gold electrode chemiresistor devices and wire bonds; (b) SEM image of one interdigitated gold electrode chemiresistor device; (c) SEM image of several interdigitated gold electrodes; (d) SEM image of two interdigitated gold electrodes and the network of In_2O_3/SWCNT between them.

The crystallinity of the indium oxide phase is crucial to the room temperature response of the sensor. While the sensitivity of the hybrid materials overall demonstrates a baseline response to both ethanol and acetone, once the annealing temperature crosses 400 ^oC, the formation of a higher crystalline phase, as shown in the XRD spectra (Fig. 2.2c), significantly influences the

device response (Fig. 2.7c). The response to ethanol is larger than that of acetone, particularly when the annealing process ramps to 400 ^{o}C and immediately cools down once reached. However, as the calcination conditions exceed 400 ^{o}C, the sensor begins to lose activity, which may be due to the detachment of crystalline In_2O_3 domains from the SWCNT. Past 400 ^{o}C, ox-SWCNTs can be thermally reduced, which may result in breaking the covalent linkage between indium crystals and SWCNTs.

The device response is defined as:

$$\frac{G_i - G_f}{G_i} * 1000/\Delta t \quad \text{(Eq. 4)}$$

where G_i is initial conductance immediately before organic vapor exposure, G_f is final conductance after 1 minute of organic vapor exposure, and Δt is amount of time between when G_i and G_f are recorded, which in this case is sixty seconds. Device response is only calculated for the first minute of vapor exposure since that is the time when the conductance drop of the sensor has a constant slope. For the best sensing material (400 ^{o}C, held for 0 minutes), the device response is plotted against the vapor concentration of both acetone and ethanol (Fig. 2.7d). For ethanol, the device response has a linear relationship to the logarithm of the vapor concentration, such that the sensor behavior can be fit with the Freundlich equation. The larger response to ethanol over acetone is consistent with other indium oxide-based sensors, but has been largely unexplained.

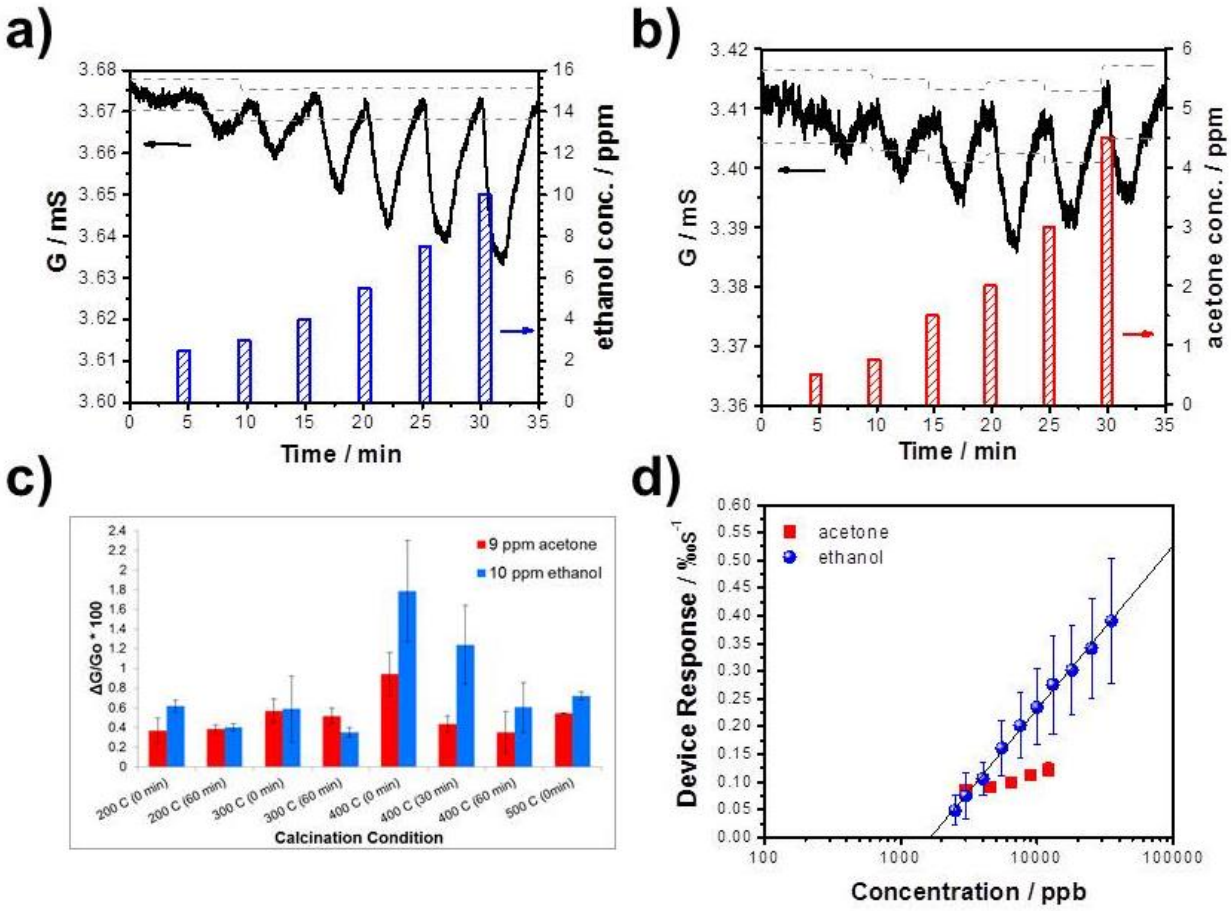

Figure 2.7 Electrical behavior of In_2O_3/SWCNT to varying concentrations of acetone and ethanol. (a, b) Conductance (G) versus time response of In_2O_3/SWCNT calcinated at 400 ºC, held for 0 minutes, to varying concentrations of acetone and ethanol, respectively. Dotted lines are $3s_{bl}$ from G_i. (c) Sensing response of various In_2O_3/SWCNT calcination conditions to 10 ppm ethanol and 9 ppm acetone. (d) Response rate of In_2O_3 versus vapor concentration. All sensing experiments done in dry N_2 environment.

2.4.5 DFT Calculations to Understand Ethanol Sensitivity

Using a crystalline In_2O_3 (111) surface, the adsorption properties of acetone and ethanol were theoretically investigated. In_2O_3 (111) surface is used because it is observed as the crystal lattice phase under HRTEM. The corresponding binding energies and the type of charge transfer obtained in this case (Figure 2.8a-c) is similar to that observed in the case of the hybrid SWCNT/COOH/$(In_2O_3)_8$ system shown above in Fig. 2.4. In particular, the largest adsorption energies for the two molecules are similar with values of 19.0 kcal/mol for ethanol and 18.9 kcal/mol for acetone. However, the adsorption energy for dissociative adsorption of ethanol (Fig. 2.8c) is significantly higher than simple chemisorption of acetone, which explains the overall higher activity of In_2O_3/SWCNT toward ethanol (slope from Fig. 2.7d). To assess the plausibility of the theoretical model used, diffuse reflectance infrared Fourier transform spectroscopy (DRIFTS) is performed on In_2O_3/SWCNT in the presence of ethanol vapors (Fig. 2.8d). The νCO frequencies for ethoxy specie are observed and are found to correspond well to the calculated frequencies for the adsorbed ethoxy specie on In_2O_3(111) surface (Fig. 2.8e).

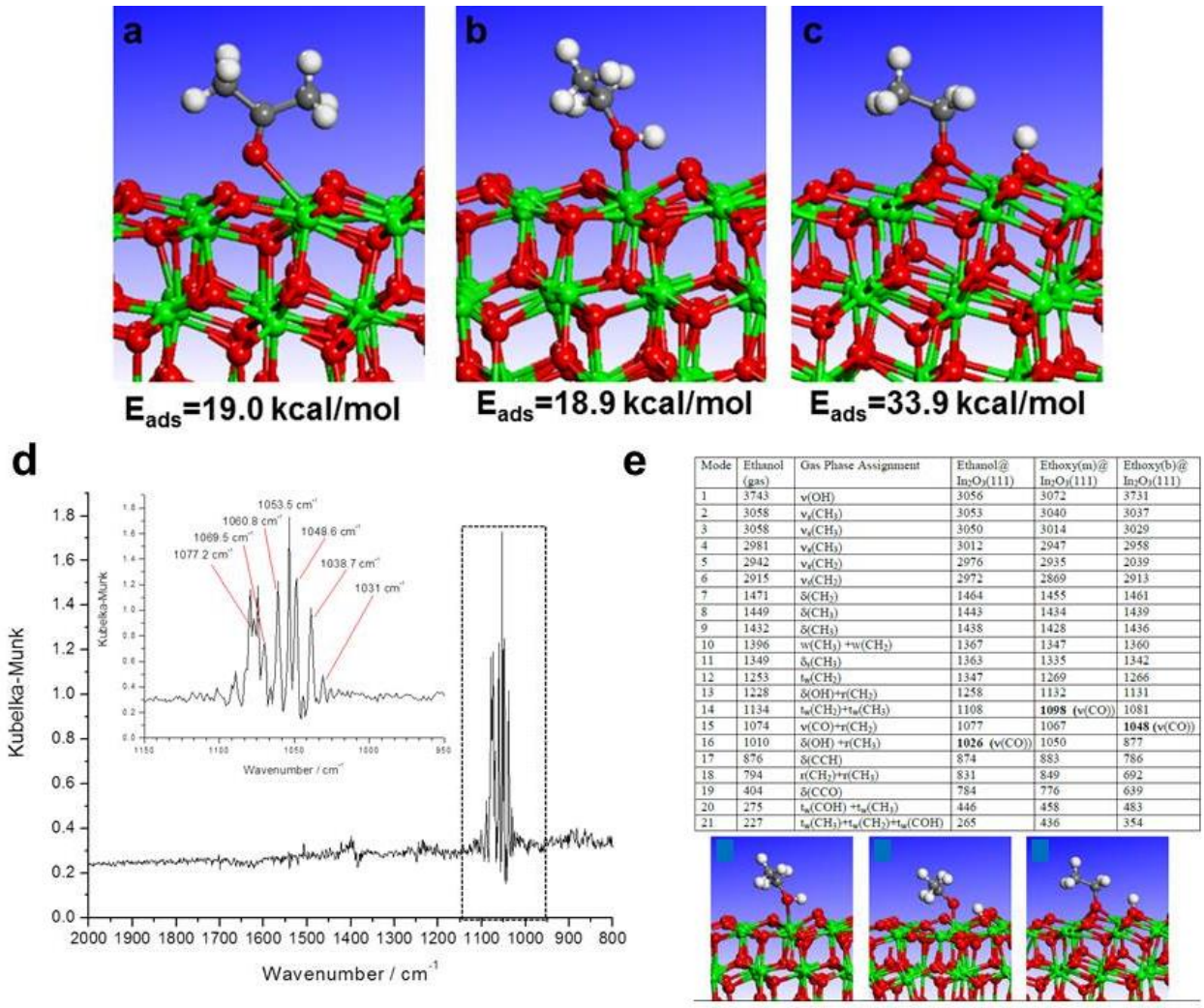

Mode	Ethanol (gas)	Gas Phase Assignment	Ethanol@ In_2O_3(111)	Ethoxy(m)@ In_2O_3(111)	Ethoxy(b)@ In_2O_3(111)
1	3743	ν(OH)	3056	3072	3731
2	3058	$\nu_a(CH_3)$	3053	3040	3037
3	3058	$\nu_a(CH_3)$	3050	3014	3029
4	2981	$\nu_s(CH_3)$	3012	2947	2958
5	2942	$\nu_s(CH_2)$	2976	2935	2039
6	2915	$\nu_s(CH_2)$	2972	2869	2913
7	1471	$\delta(CH_2)$	1464	1455	1461
8	1449	$\delta(CH_3)$	1443	1434	1439
9	1432	$\delta(CH_3)$	1438	1428	1436
10	1396	$w(CH_3)+w(CH_2)$	1367	1347	1360
11	1349	$\delta_s(CH_3)$	1363	1335	1342
12	1253	$t_w(CH_2)$	1347	1269	1266
13	1228	$\delta(OH)+r(CH_2)$	1258	1132	1131
14	1134	$t_w(CH_2)+t_w(CH_3)$	1108	**1098** (ν(CO))	1081
15	1074	$\nu(CO)+r(CH_2)$	1077	1067	**1048** (ν(CO))
16	1010	$\delta(OH)+r(CH_3)$	**1026** (ν(CO))	1050	877
17	876	δ(CCH)	874	883	786
18	794	$r(CH_2)+r(CH_3)$	831	849	692
19	404	δ(CCO)	784	776	639
20	275	$t_w(COH)+t_w(CH_3)$	446	458	483
21	227	$t_w(CH_3)+t_w(CH_2)+t_w(COH)$	265	436	354

Figure 2.8 Adsorption of acetone and ethanol to In_2O_3 (111) surface. Representative adsorption configurations of acetone (a) and ethanol (b,c) adsorbed on In_2O_3 (111) surface. In panel (b) the adsorption of ethanol in a molecular undissociated state is illustrated while panel (c) shows the case when the H atom of ethanol is donated to the surface with formation of an ethoxy species. (d) DRIFTS of In_2O_3/SWCNT composite exposed to ethanol vapors and (e) calculculated frequencies of vibrations for different types of ethanol adsorption on In_2O_3 (111): 1) unimolecular adsorption, 2) monodentate dissociative adsorption, and 3) bidentated dissociative adsorption.

2.5 CONCLUSION

In conclusion, it has been shown that In_2O_3 can be grown on the surface of ox-SWCNTs *via* a sol-gel method. Inherent oxygen functional groups on the ox-SWCNT surface, likely located at defects as shown through DFT calculations, provide sites for covalent linkage to In_2O_3. Through careful calcination, the In_2O_3 phase can be crystallized and condensed on the SWCNTs, providing close association between the crystal's surface and the nanotube surface, while allowing CNT-CNT contacts. At the Fermi level of this hybrid material, a delocalized electronic state across both the oxide cluster and on the CNT was observed through DFT calculations, which will contribute to this hybrid system's increased sensor performances. Sensing experiments with this novel hybrid material were performed in a non-oxidative environment and showed sensitivities to low concentrations of acetone and ethanol vapors. Therefore, given these experimental and theoretical DFT results, it is shown that ethanol preferentially adsorbs onto In_2O_3/SWCNT, making this composite material a potential candidate for low-power ethanol sensing.

3.0 GROWTH OF ZIF-8 ON MOLECULARLY ORDERED 2-METHYLIMIDAZOLE/SINGLE-WALLED CARBON NANOTUBES TO FORM HIGHLY POROUS, ELECTRICALLY CONDUCTIVE COMPOSITES

3.1 CHAPTER PREFACE

Parts of the text and figures in this chapter were published in Chemical Science, and have been reprinted with permission from Chem. Sci. 2019 DOI: 10.1039/C8SC03987A – Published by The Royal Society of Chemistry

List of contributors: James E. Ellis, Zidao Zeng, Sean I. Hwang, Shaobo Li, Tian-Yi Luo, Seth C. Burkert, David L. White, Nathaniel L. Rosi, Jeremiah J. Gassensmith, Alexander Star

Contributions: JEE, ZZ, SL, JJG, and AS designed synthetic and characterization experiments. JEE, ZZ, and SL performed synthetic experiments. JEE performed TEM, XRD, and electrical characterization. TL and NLR designed and performed gas adsorption experiments. SCB performed SEM. DLW performed Raman spectroscopy. SIH performed the gas sensing experiments. JEE and AS wrote this manuscript.

3.2 INTRODUCTION

A material that combines the physical properties of periodic porosity and electrical conductivity is an appealing candidate for a variety of applications including sensors, photovoltaics, thermoelectrics, electrocatalysts, and electrical energy storage materials. Electrically conductive metal-organic frameworks (MOFs) contain both of these physical properties; however, the mechanism of electrical conductivity found in MOFs, described as charge hopping, results in a much lower charge mobility than band transport materials. Charge hopping limits MOF electrical conductivity to high electrical fields and short distances, thus limiting their field of application. A potential solution to the low charge mobility inherent to conductive MOFs is to hybridize MOFs with band transport materials like carbon nanotubes (CNTs), thus improving electrical transduction in MOF-based sensors and electrocatalysts.

In this study, a zeolitic imidazolate framework (ZIF-8) was chosen as the model MOF because of its water stability, ease of synthesis, and well-documented characterization. ZIF-8 is composed of Zn(II) ions and 2-methylimidazole (2mIM) linkers, and has been studied as both a gas storage material as well as a biomimetic mineralization layer material. ZIF-L and dia(Zn) are polymorphs comprised of Zn(II) and 2mIM, but with different crystal topologies than ZIF-8. Control of Zn(II):2mIM ratio and temperature allows one polymorph to be favored over the other two during aqueous synthesis. The crystal morphology of ZIF-L dia(Zn) resemble a thin, almost two-dimensional leaf-like shape, while ZIF-8's crystal morphology is rhombic dodecahedral. Unlike ZIF-8, ZIF-L and dia(Zn) are nonporous at 77K; however, at STP, ZIF-L outperforms ZIF-8 in CO_2 uptake and selectivity over N_2 and CH_4.[110]

Several examples of MOF/CNT hybrid composites have been synthesized. Early reports found that the inclusion of CNTs into large MOF crystals enhanced gas adsorption compared to

the pristine MOF species.[111-112] Shim and coworkers were the first to demonstrate a core-shell composite material through homogeneous decoration of small ZIF-8 crystals on PVP-dispersed multi-walled carbon nanotubes (MWCNTs).[113] MOF/MWCNT hybrids have been applied toward electrocatalysis and energy storage because they are electrically conductive, high surface area materials.[114-117] A pyrolysis step is added to some MOF/MWCNT composites in order to convert the MOF shell into catalytically active metal nanoparticles and heteroatom-doped carbon domains.[118-120] Unlike MWCNTs, which have metallic electrical characteristics, smaller diameter single-walled carbon nanotubes (SWCNTs) can have either a metallic or semiconducting electronic structure depending on their chirality.[38] For this reason, they are purified based on chirality and applied toward electrical devices such as sensors and field-effect transistors. SWCNTs have excellent electrical characteristics (charge mobility, etc.) and consist almost entirely of surface atoms thereby making their electronic structure extremely sensitive to the surrounding chemical environment. To our knowledge, only one MOF/single-walled carbon nanotube (SWCNT) composite has been synthesized;[121] however, no investigation of MOF growth on the surface of SWCNTs has been reported. Gassensmith and coworkers investigated the growth of ZIF-8 on tobacco mosaic virus, a one-dimensional bionanoparticle, and discovered that careful control of the MOF precursor ligand/metal ratio significantly affects the resulting morphology of the composite.[122] For this reason we chose to composite ZIF-8 with SWCNTs, since a porous, semiconducting nanowire is a promising material for chemical sensing.

3.3 EXPERIMENTAL SECTION

ZIF/SWCNT synthesis with excess ox-SWCNT: To 6 ml of 0.5 mg/ml unsaturated CNT, 10 ml of 1344 mM 2mIM was added and mixed for 5 minutes. Finally, a 5 ml addition of 84 mM zinc nitrite was added. The vial was left unstirred for 4 hours. Solution was black when collected. Sample was centrifuged and washed with water twice. Black supernatant was observed and removed during water wash. Precipitate was collected and analyzed.

Preparation of 2mIM-saturated ox-SWCNT: 1904 mg 2mIM was dissolved in 15 ml of nanopure water and was added into 5 ml of 0.5 mg/ml CNT. The mixture was set for 2 hours before filtration with 0.2 μm pore size filter membrane. CNT was transferred into vail together with the filter membrane and 5 ml of nanopure water was added. Slight sonication was done for a couple of seconds to resuspend the CNT and the filter membrane was removed. Another 15 minutes sonication was done before further synthesis with this CNT.

ZIF/SWCNT synthesis with Zn:2mIM 1:40 ratio ($[Zn^{2+}]$ = 20 mM): To the 3 ml of 2mIM-saturated ox-SWCNT solution (0.1 mg/ml), 8 ml of 2-methylimidazole solution (1500 mM) was added. 4 ml of the zinc precursor(zinc nitrite or zinc acetate) solution (75 mM) was added after. The vial was shaken for 20 seconds after all the precursors were added and set overnight for 24 hours. Then the sample was centrifuged and washed with water twice and stored in water. For gas adsorption experiments, the material was washed twice with methanol after the water wash.

ZIF/SWCNT synthesis with Zn:2mIM 1:40 ratio ($[Zn^{2+}]$ = 10 mM): To 3 ml of 2mIM-saturated ox-SWCNT solution (0.05 mg/ml), 8 ml of 2-methylimidazole solution (750mM) was added. 4 ml of the zinc precursor(zinc acetate) solution (37.5 mM) was added after. The vial was

shaken for 20 seconds after all the precursors were added and left unstirred. The sample was centrifuged and washed with water twice and stored in water.

ZIF/SWCNT synthesis with Zn:2mIM 1:40 ratio ([Zn^{2+}] = 6.6 mM): To 50 μL of ox-SWCNT (4 mg/mL), 6 mL of 2-methylimidazole solution (400 mM) was added. 3 mL of the zinc precursor (zinc acetate) solution (20 mM) was added after. The vial was shaken for 20 seconds after all the precursors were added and left unstirred. The sample was centrifuged and washed with water.

ZIF/SWCNT synthesis with Zn:2mIM 1:8 ratio ([Zn^{2+}] = 20 mM): To 3 ml of 2mIM-saturated ox-SWCNT solution (0.1 mg/ml), 8 ml of 2-methylimidazole solution (300 mM) was added. 4 ml of the zinc precursor (zinc nitrite or zinc acetate) solution (75 mM) was added after. The vial was shaken for 20 seconds after all the precursors were added and collected after 24 hours. The sample was centrifuged and washed with water twice and stored in water.

Characterization section

Raman spectroscopy. Raman spectra were collected from an XplorA Raman AFM-TERS system with a 638 nm (24 mW) laser at 10% laser intensity and 1 s exposure time averaged over 10 accumulations. Sample were prepared by dropcasting concentrated solutions on glass slides.

Electron microscopy. Transmission electron microscopy (TEM) samples were prepared by dropcasting 7 μL of diluted samples in water on TEM sample grids (carbon film, 400 mesh copper grid; Electron Microscopy Sciences). The TEM instrument model used was FEI Morgagni. Scanning electron microscopy (SEM) of rGO/carbon nitride was performed directly on the Si chip. The SEM instrument model used was ZEISS Sigma 500 VP.

Powder x-ray diffraction (PXRD). PXRD was performed on a Bruker D8 XRD system equipped with LynxEye detector. Powder carbon nitride on a glass slide was the sample tested.

2θ angles between 8º and 60º were measured at 0.02º intervals with a rate of 0.3 seconds/point. The x-ray source was Cu Kα held at 40 kV and 40 μA with a 0.2 mm aperture slit width.

Gas adsorption experiments. Gas adsorption isotherms were collected using a Quantachrome Autosorb-1 instrument. A 9 mm stem diameter sample cell equipped with Cell Seal™ assembly was first evacuated on an outgassing station at room temperature and backfilled with N_2 gas. Once removed from outgassing station, the empty cell capped with a Cell Seal™ valve was weighed on a balance. Approximate 40 mg of ZIF-8/SWCNT (zinc acetate; 1:40 Zn:2mIM; $[Zn^{2+}]$ = 20 mM) sample was loaded to the sample cell. The sample cell was then evacuated at 80 ºC for 12 hours using an outgassing station. The cell was allowed to cool to room temperature, backfilled with N_2 gas and removed from the outgassing station. The loaded sample cell capped with a Cell Seal™ valve was weighed. The weight of empty cell was subtracted from that of loaded cell to calculate the sample weight. The sample cell was then installed to analysis station to perform the gas adsorption experiments. A liquid N_2 bath was used for N_2 adsorption experiments at 77 K. A water–ethylene glycol bath was used for N_2 and CO_2 experiments at 298 K. UHP grade N2 and CO2 gas adsorbates (99.999%) were used. Brunauer–Emmett–Teller (BET) surface area was calculated based on N_2 77K isotherm data.

Electrical characterization: A 2 x 2 mm SiO_2 chip with 4 interdigitated gold electrode was used to collect the I-V characteristics of ZIF-8/SWCNT. ZIF-8/SWCNT in water was dropcast above the chip such that the entire surface was covered with a very thick layer of ZIF-8/SWCNT. The I-V characteristics were collected with a Keithly 2400 sourcemeter and LabView software.

3.4 RESULTS AND DISCUSSION

3.4.1 Molecularly Ordered Imidazole Layer on SWCNTs

In this work, all reactions were done in ambient and aqueous conditions. In order to get well-dispersed carbon nanotubes in aqueous solution, oxidized SWCNTs (ox-SWCNTs) were used. Ox-SWCNTs are approximately 3 atomic % of oxygen in the form of hydroxyl and carboxyl groups on their sidewall and ends. Sonication of ox-SWCNTs in polar solvents promotes dispersive forces, allowing separation of large carbon nanotube agglomerates into smaller bundles and individual ox-SWCNTs. A typical ZIF-8 synthesis involves careful control of zinc salt and 2-methylimidazole (2mIM) concentrations and Zn:2mIM ratio. The addition of ox-SWCNTs as a precursor adds a complicating factor to the synthesis, wherein the order in which the precursors are added plays an important synthetic role. When ox-SWCNTs are mixed with the zinc salt first or both precursors simultaneously, they re-agglomerate and precipitate out of solution before any ZIF-8 forms. This effect is caused by the salt's contraction of the hydration layer around the charged ox-SWCNTs. However, when ox-SWCNTs are first mixed 2mIM, they remain dispersed in solution even after adding Zn salt (Fig. 3.1). It has been previously observed through molecular dynamics simulations that 1-ethyl-3-methylimidazolium tetrafluoroborate ($EMI^+BF_4^-$) forms an external solvation layer around SWCNTs through π-π interaction between the SWCNTs and EMI^+.[123]

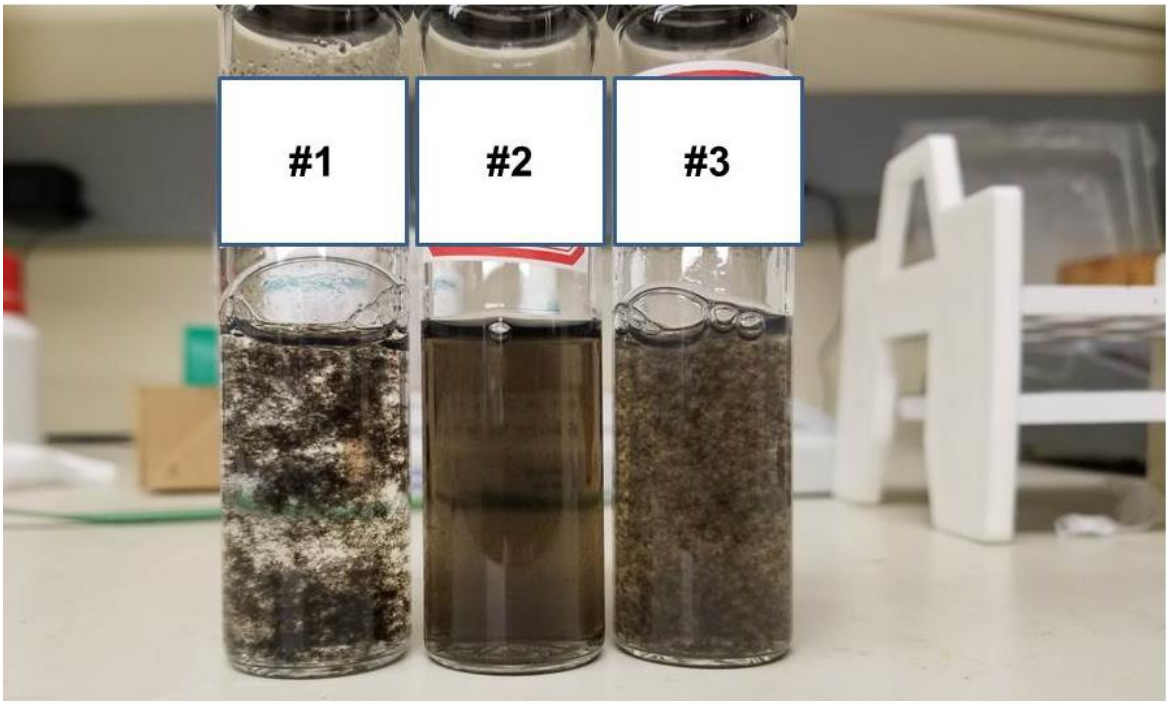

Figure 3.1 Photograph of ZIF-8/SWCNT water-based syntheses. Solution #1: ox-SWCNT solution is added to zinc salt solution first, then 2mIM is added. Solution #2: ox-SWCNT is added to 2mIM solution first, then zinc salt is added. Solution #3: ox-SWCNT is added to zinc salt and 2mIM solution simultaneously.

A synthesis was done with a large excess of ox-SWCNT (0.336 mmol $Zn(NO_3)_2$/13.44 mmol 2mIM/3 mg ox-SWCNT in 21 mL of H_2O) to determine whether a similar solvation layer forms between 2-methylimidazole and SWCNTs. If a 2mIM solvation layer forms around ox-SWCNT through π-stacking, then an excess amount of ox-SWCNTs should sequester all available 2mIM and prevent the formation of ZIF-8 crystals in solution. Ox-SWCNTs and 2mIM were combined and left for 5 minutes before adding the zinc nitrate hexahydrate solution and

leaving for 4 hours. The reaction was centrifuged to remove the mother liquor, then washed with water and methanol. X-ray diffraction (XRD) of this material showed a dominant single peak at $2\theta = 17.78^{o}$ and very small peaks relating to ZIF-8 formation (Fig. 3.2a). Fukushima *et al.* have previously reported the molecular ordering of molten salts (in their case, imidazolium-based ionic liquids) by SWCNTs.[124] They observed a single XRD peak with d-spacing of 4.60 Å, which they attributed to unimodal long-range molecular ordering of plane-to-plane separated imidazolium ions without polycrystalline character. A similar molecular ordering phenomenon occurs between SWCNTs, 2mIM, and zinc. According to XRD, the d-spacing of this material is 4.98 Å, which is large for π-stacked 2mIM. When ox-SWCNTs were mixed with the same amount of 2mIM, but zinc nitrate was not subsequently added, no XRD peak was detected. This observation, in addition to the larger than expected d-spacing, implies that the Zn (II) ions play a role in the long-range ordering of 2mIM around the ox-SWCNTs.

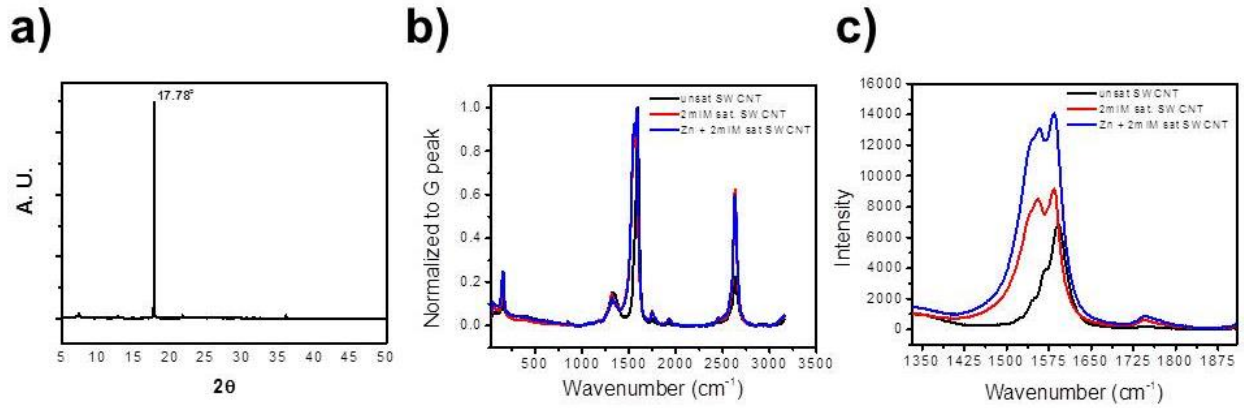

Figure 3.2 Characterization of excess ox-SWCNT synthesis. (a) PXRD of excess ox-SWCNT synthesis product showing one significant peak at 17.78°; (b) Raman spectra of unsaturated ox-SWCNT (black), 2mIM-saturated ox-SWCNT (red), and excess ox-SWCNT synthesis product (blue). Entire spectrum is normalized to the G peak; (c) Raman spectrum of the G-peak for unsaturated ox-SWCNT (black), 2mIM-saturated ox-SWCNT (red), and excess ox-SWCNT synthesis product (blue).

Raman spectroscopy demonstrated that both the crystalline 2mIM/ox-SWCNT material and the non-crystalline 2mIM-saturated ox-SWCNT undergo the same G peak shape change and red-shift as compared to untreated ox-SWCNTs (Fig. 3.2c). The ox-SWCNT spectrum has a single G peak which is indicative of SWCNT bundling; in contrast, the G peak of the 2mIM/ox-SWCNT materials split into G^- and G^+ peaks, which is a signature of single, unbundled SWCNTs.[125-126] Moreover, the G peak red-shifted for both 2mIM/ox-SWCNT materials compared to the ox-SWCNT G peak. Charge transfer may be occurring between 2mIM and ox-SWCNTs since red-shifting of a SWCNT G peak indicates n-doping.[127]

Figure 3.3 illustrates the effect precursor addition order has on ox-SWCNTs. Addition of the zinc salt first "salts out" or agglomerates the ox-SWCNTs because the hydration layer that originally dispersed them is lost to the ionic solution. This agglomeration affects the resulting ZIF-8/SWCNT morphology, such that large ZIF-8 crystals grow on islands of agglomerated ox-SWCNTs rather than along the nanotube axis. In all later syntheses described in this work, 2mIM-saturated ox-SWCNTs are used as the precursor material to prevent agglomeration, to promote nucleation of ZIF-8 crystals according to pathway #2 (Fig. 3.3), and to prevent 2mIM from further π-stacking on ox-SWCNTs, which would alter the Zn:2mIM ratio.

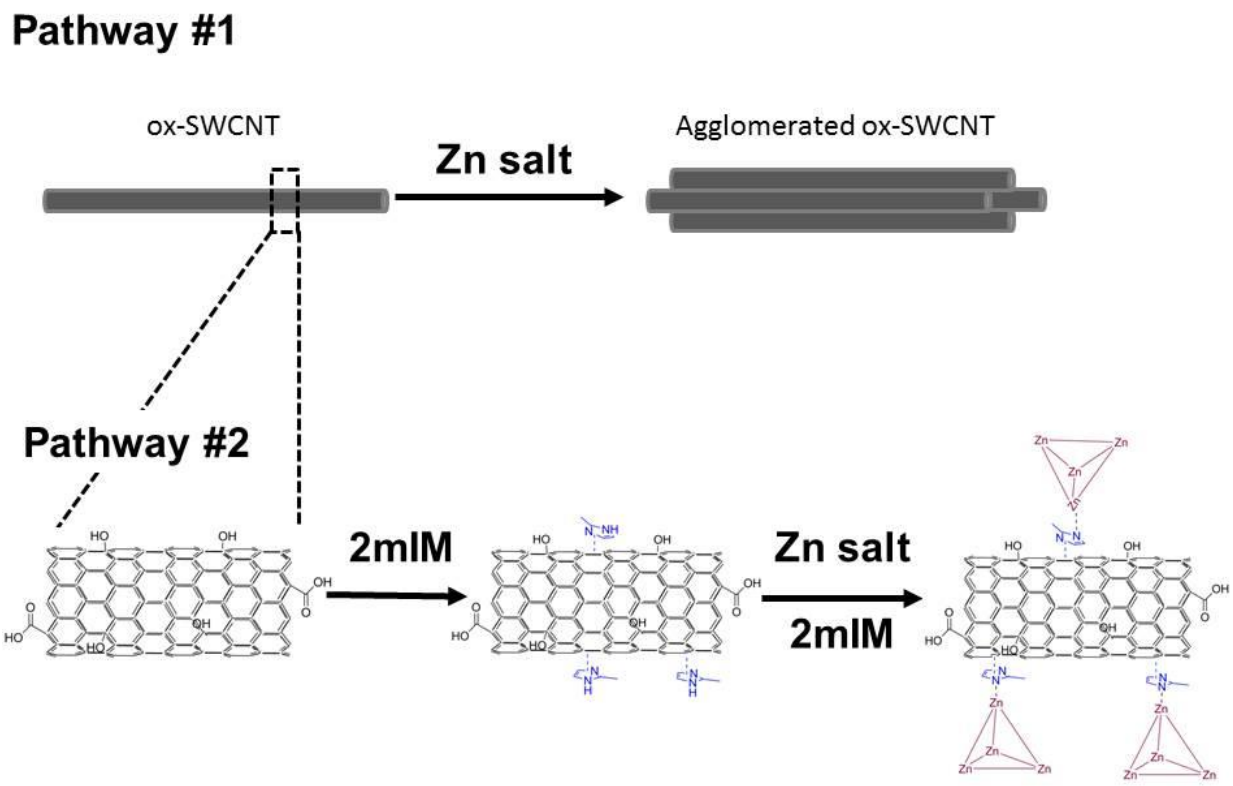

Figure 3.3 Schematic illustration of the effect of precursor order. Pathway #1 results in ox-SWCNT agglomeration and precipitation. Pathway #2 results in a 2mIM solvation layer around ox-SWCNTs and subsequent Zn (II) chelation.

3.4.2 Effect of Synthetic Parameters on ZIF/SWCNT Morphology

Factors that are known to influence ZIF growth, size, morphology, and polymorph in water-based synthesis include zinc precursor source, zinc concentration, zinc to 2mIM ratio, and temperature.[128-129] In this work, zinc (II) acetate and zinc (II) nitrate hexahydrate were used as zinc sources. In order to synthesize a ZIF-8/SWCNT composite, a 1:40 Zn:2mIM ratio and total zinc concentration of 20 mM was used for each zinc source. The zinc to ox-SWCNT ratio used was 1 mmol Zn:1 mg ox-SWCNT. The overall precursor composition for this synthesis was 0.3 mg 2mIM-saturated ox-SWCNT/12 mmol 2mIM/0.3 mmol zinc source added in sequential order (15 mL total volume). The reaction was left unstirred at room temperature for 24 hours. The reaction precipitate was collected with centrifugation and washed in water and methanol. The morphology of these syntheses may be described as large ZIF-8 crystals (1—1.5 μm) threaded with SWCNTs (Fig. 3.4a-d). TEM images show crystal growth occurs along a linear path, which is consistent with growth along a CNT axis. XRD of the ZIF-8/SWCNT composites made from both zinc sources contain characteristic ZIF-8 diffraction peaks (Fig. 3.4e). The peak widths of the ZIF-8/SWCNT composite made with zinc nitrate hexahydrate is ~3 times broader than the composite made with zinc acetate. The XRD peak broadening of ZIF-8/SWCNT made from zinc nitrate hexahydrate can be attributed to the smaller crystal domain size of the composite. TEM and SEM of the zinc nitrate ZIF-8/SWCNT composite clearly show small crystallites that are coalescing into larger crystals (Fig. 3.4a, b). This observation is consistent with the Hofmeister series effect wherein zinc nitrate is more likely to nucleate and form small crystallites compared to zinc acetate.[130]

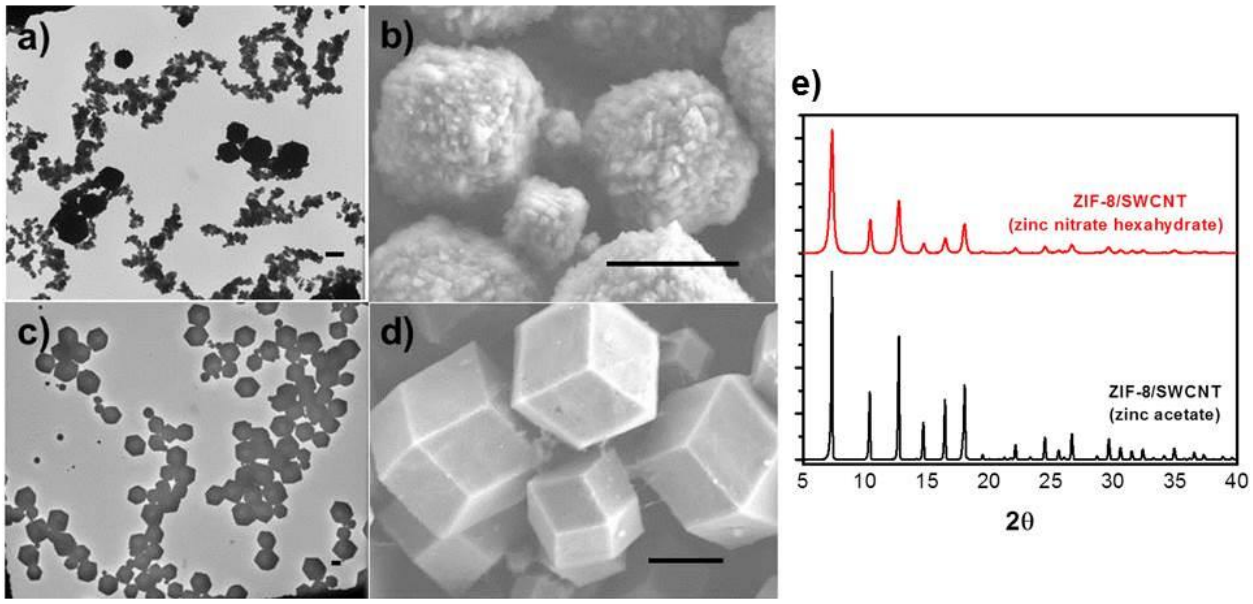

Figure 3.4 TEM, SEM, and XRD of ZIF-8/SWCNT composite. (a, b) ZIF-8/SWCNT from zinc (II) nitrate hexahydrate and (c, d) ZIF-8/SWCNT from zinc (II) acetate. Scale bars are 1 μm. (e) PXRD of ZIF-8/SWCNT synthesized from different zinc sources.

The zinc:2mIM ratio controls what type of polymorph/pseudopolymorph is produced in water-based syntheses. High ratios (1:35 and above) produce ZIF-8, while lower ratios produce ZIF-L, dia(Zn), or a mixture of one with ZIF-8. A low zinc:2mIM ratio (1:8) using zinc acetate produces pure dia(Zn) while zinc nitrate produces pure ZIF-L.[128] A low ratio synthesis was performed with 2mIM-saturated ox-SWCNTs (0.1 mg ox-SWCNT/0.8 mmol 2mIM/0.1 mmol zinc nitrate/15 mL total volume). XRD of this material yields a mixture of ZIF-8 and ZIF-L peak features (Fig. 3.5b); moreover, TEM shows large (>3 μm) crystals with a morphology unlike ZIF-8 (rhombic dodecahedron) or ZIF-L (thin, leaf-shaped) (Fig. 3.5a). This product can be understood as the result of two different reaction environments containing different precursor ratios: solution and ox-SWCNT surface. 2mIM is expected to concentrate at the surface of ox-SWCNTs through π-stacking, which will promote ZIF-8 crystal growth. In contrast, the solution zinc:2mIM ratio remains 1:8, leading to ZIF-L crystal growth. It has been previously reported that when separately synthesized ZIF-8 and ZIF-L crystals are combined into a single solution, they will coalesce into a new core-shell composite.[131] The addition of ox-SWCNTs into low zinc:2mIM ratio solutions produces similar ZIF-L/ZIF-8/ox-SWCNT composites in a one-pot synthesis.

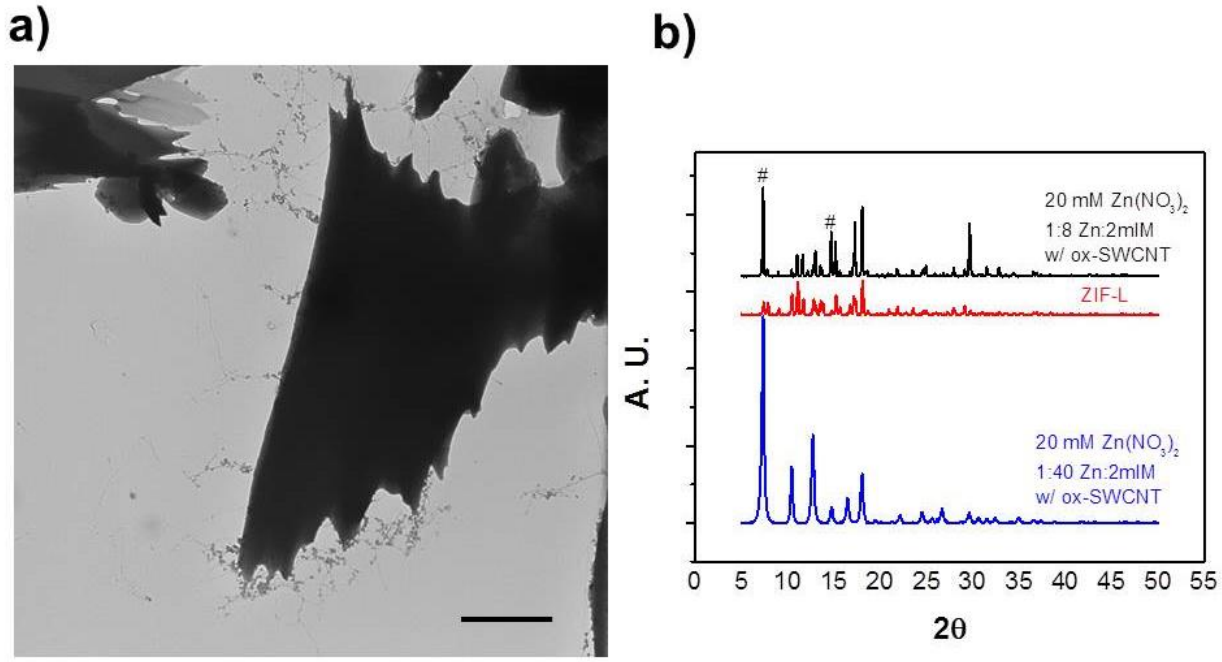

Figure 3.5 Zn:2mIM = 1:8 synthesis with ox-SWCNTs. (a) TEM image of Zn:2mIM = 1:8 with ox-SWCNTs synthesis product; (b) PXRD patterns of Zn:2mIM = 1:8 with ox-SWCNTs synthesis product (black), Zn:2mIM = 1:8 without ox-SWCNTs which is representative of pure ZIF-L (red), and Zn:2mIM = 1:40 with ox-SWCNTs synthesis product which is representative of ZIF-8/SWCNT (blue). (#) symbols above certain peaks are used to highlight ZIF-8 peak features in the Zn:2mIM = 1:8 with ox-SWCNT diffraction pattern.

Decreasing the overall precursor concentration slows the kinetics of the reaction and achieves smaller ZIF-8 coverage on the surface of ox-SWCNTs. 10 mM zinc acetate reaction (1:40 zinc:2mIM ratio) was done with 2mIM-saturated ox-SWCNTs and collected after 24 hours and 90 hours. After 24 hours a smaller ZIF-8 crystal shell growth (approximately 90 nm) on the ox-SWCNTs was observed (Fig. 3.6a). However, the decrease in precursor concentration also lowers the pH, such that large pseudopolymorph dia(Zn) crystals form in solution if the reaction is left for 90 hours (Fig. 3.6b). XRD of the 10 mM synthesis shows a mixture of ZIF-8 and dia(Zn) peaks, indicating that there are two growth environments where crystals can grow: solution and ox-SWCNT sidewalls (Fig. 3.6c). XRD of 20 mM zinc acetate 1:8 ratio with 2mIM-saturated ox-SWCNTs synthesis product is shown in Figure 3.6c as a dia(Zn) diffraction pattern reference (red diffraction pattern).

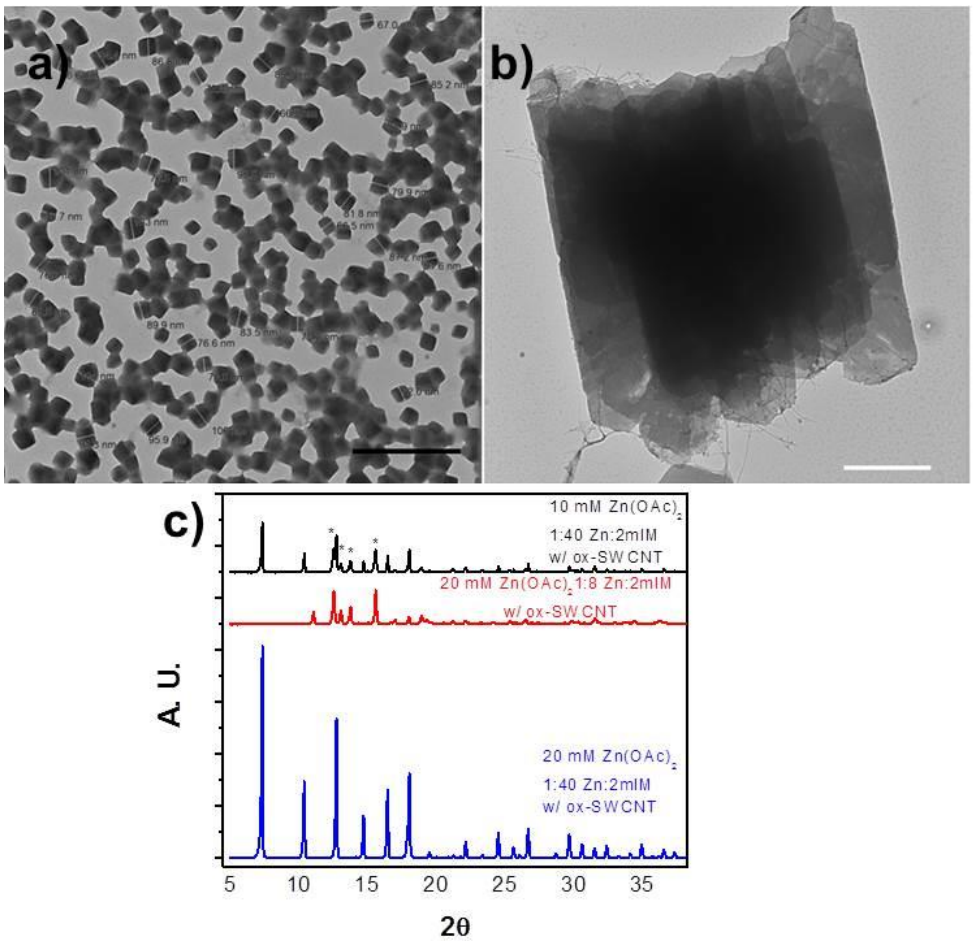

Figure 3.6 Zn:2mIM = 1:40, [Zn^{2+}] = 10 mM (zinc acetate) synthesis with ox-SWCNTs. (a) TEM image of Zn:2mIM = 1:40, [Zn^{2+}] = 10 mM with ox-SWCNTs synthesis product after 24 hours; (b) TEM image of Zn:2mIM = 1:40, [Zn^{2+}] = 10 mM with ox-SWCNTs synthesis product after 90 hours; (c) PXRD patterns of Zn:2mIM = 1:40, [Zn^{2+}] = 10 mM with ox-SWCNTs synthesis product after 90 hours (black), Zn:2mIM = 1:8, [Zn^{2+}] = 20mM (zinc acetate) with ox-SWCNTs which is representative of dia(Zn) (red), and Zn:2mIM = 1:40, [Zn^{2+}] = 20 mM with ox-SWCNTs synthesis product which is representative of ZIF-8/SWCNT (blue). (*) symbols above certain peaks are used to highlight dia(Zn) peak features in the Zn:2mIM = 1:40, [Zn^{2+}] = 10 mM with ox-SWCNT diffraction pattern.

3.4.3 Gas Adsorption and Electrical Conduction Characterization of ZIF-8/SWCNT

The gas adsorption and current-voltage (I-V) performance of ZIF-8/SWCNT (shown in Fig. 3.4c, d) was tested (Fig. 3.6). ZIF-8/SWCNT displayed a type-I isotherm and the BET surface area of ZIF-8/SWCNT was calculated to be 1792 m^2/g, which is near the reported BET surface area of pure ZIF-8(1851 m^2/g).[132] The CO_2 vs. N_2 uptake was tested and showed the same preference for CO_2 uptake as pure ZIF-8. In order to test I-V performance, a 3μL droplet of ZIF-8/SWCNT solution was dropcast on a device of two interdigitated gold electrodes. The material displayed a conductance of 25 μS and the I-V curve shape indicates a mixture of semiconducting and metallic behavior. These experiments demonstrate both the highly microporous and electrically conductive nature of the reported ZIF-8/SWCNT composite.

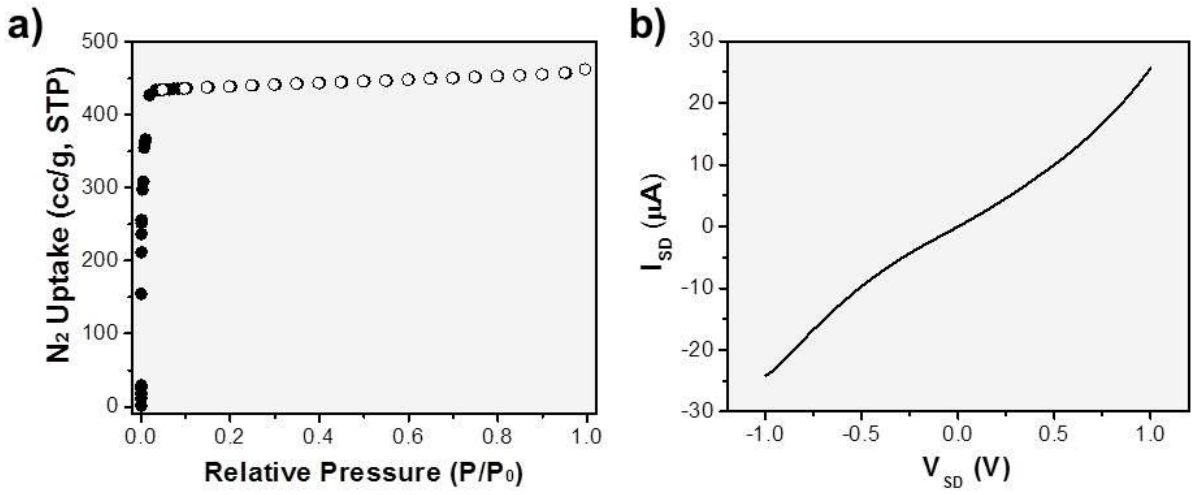

Figure 3.7 Porosity and electrical conductivity of ZIF-8/SWCNT. (a) N_2 adsorption isotherm of ZIF-8/SWCNT at 77 K; (b) I-V curve of ZIF-8/SWCNT

3.5 CONCLUSION

In conclusion, this work demonstrates the molecular ordering of 2-methylimidazole (2mIM) as a solvation layer on the surface of oxidized single-walled carbon nanotubes (ox-SWCNTs). This 2mIM solvation layer gives rise to ZIF-8 growth on ox-SWCNT sidewalls. The high concentration of 2mIM on ox-SWCNTs produces ZIF-8 at the surface of the nanotube even at low zinc:2mIM ratios that typically produce ZIF-L. The size of ZIF-8 growth on ox-SWCNTs can be controlled by precursor concentration, wherein decreasing the precursor concentration decreases the size of ZIF-8. Finally, the ZIF-8/SWCNT composite was shown to combine the porous nature of ZIF-8 with the electrically conductive nature of carbon nanotubes. A highly porous, electrically conductive nanomaterial should be effective for a variety of applications such as sensing, electrocatalysis, and energy storage.

4.0 UNCONDENSED GRAPHITIC CARBON NITRIDE ON REDUCED GRAPHENE OXIDE FOR OXYGEN SENSING VIA A PHOTOREDOX MECHANISM

4.1 CHAPTER PREFACE

Parts of the text and figures in this chapter were published in ACS Applied Materials and Interfaces, and have been reprinted with permission from *ACS Appl. Mater. Interfaces* **2017,** DOI**:** 10.1021/acsami.7b06017.

List of authors: James E. Ellis, Dan C. Sorescu, Seth C. Burkert, David L. White, Alexander Star

Author Contributions: JEE and AS designed the experiments and wrote the manuscript, JEE performed the experimental work, SCB collected SEM images, DLW collected HRTEM images, DCS performed computational modeling and DFT calculations.

4.2 INTRODUCTION

The ability to detect and quantify the concentration of a specific target gas is an important resource for a variety of fields including medical, industry, and security. In particular, molecular oxygen is a target of interest due to its ubiquity in the environment, in diverse industrial and mechanical processes, and in biological systems. For example, oxygen sensors have been deployed in automobiles and other combustion systems to determine the combustion efficiency, since inefficient combustion is directly related with harmful gas emissions.[133-134] Alternatively, dissolved oxygen concentration in biological systems is an important physiological factor that would be beneficial to sense. For example, hypoxia in tissue cells has been found to correlate with an acceleration of disease progression,[135] including tumor growth.[136] For this reason, nanoscale sensors that can map the oxygen concentration in tissues have been pursued.[137] These examples illustrate the wide-ranging condition requirements (e.g., gas vs. solution; high vs. low pressure, *etc.*) of oxygen sensing applications that drive the development of novel sensing materials and call for an understanding and optimization of their associated working mechanisms.

The research area of gas sensor development, including oxygen sensors, has benefitted from and grown alongside the rise of nanomaterials and of nano-characterization techniques.[9, 138] For example, graphene-based materials have shown excellent sensing performance at room temperature to a wide-range of different gases/vapors.[139] In addition, sensor material research has borrowed and adapted many findings from the heterogeneous catalysis field. Common heterogeneous catalyst materials, e.g., metal nanoparticles and metal oxides, have shown excellent sensor properties when coupled with good transducer materials like carbon nanotubes or graphene.[140-142] Catalytic materials provide the receptor function by adsorbing and reacting

with certain analytes, while changes in the local chemical environment and minute charge transfers are able to effect observable changes in a carbon nanomaterial's electrical properties due to its large charge carrier mobility and high surface area to volume ratio.[143] Maximizing receptor/transducer interface and choosing receptors that have complementary work functions with the transducer are important strategies for improving sensor sensitivity.

Semiconductor photocatalysts are a class of heterogeneous catalysts that utilize photo-generated electron-hole pairs for photoredox catalysis.[144-145] One such photocatalyst, "graphitic" carbon nitride, is a metal-free semiconductor that has a planar, sheet-like morphology similar to graphene.[146-147] Carbon nitride's bandgap (2.7 eV) is ideal due to its ability to be photoexcited by visible light, and has the proper band structure to catalyze multiple redox reactions;[148] it has shown activity toward water splitting,[149-150] H_2O_2 activation,[151] oxygen reduction reaction (ORR),[121, 152-154] and CO_2 reduction.[121, 155-156] Graphitic carbon nitride is produced by thermally polymerizing cyanamide, dicyandiamide, or melamine at temperatures ranging from 500-600^{o}C. Depending on the precursor and synthetic parameters, the resulting structure can be composed of heptazine[157] or triazine[158] units with different degrees of condensation (condensed-C_3N_4; uncondensed-$C_6N_9H_3$).

4.3 EXPERIMENTAL SECTION

*Synthesis and preparation of exfoliated "graphitic" carbon nitride***.** Dicyandiamide (DCDA, 99% purity, 1 gram; Sigma-Aldrich) was placed in an open quartz boat, which was subsequently placed in a quartz tube. The quartz tube atmosphere was replaced with argon and the tube was sealed on both ends by water bubblers. The sample was heated in a CVD furnace (Lindberg blue

3-zone furnace) for 2 hours at 550ºC and left to cool overnight. The remaining pale-yellow solid (~140 mg) was recovered from the quartz boat and ground in a mortar and pestle for ~10 minutes to yield a fine powder. In order to exfoliate the bulk sheets into nanosheets, the resultant carbon nitride powder was dispersed in nanopure water (100 μg/mL) and sonicated in a bath sonicator (Branson 1510) for 1 hour.

Preparation of rGO/carbon nitride chemiresistor devices. rGO was prepared through a previously described chemical reduction method.[159] Briefly, graphene oxide (5 mL, 3 mg/mL in H_2O; Graphene Supermarket) was stirred with 5 μL of hydrazine hydrate (ca. 51% hydrazine; Acros Organics) in an 80 ºC oil bath for 3 hours. The black precipitate (rGO) was collected through vacuum filtration and dispersed in DMF. Si chips, each containing 4 devices with interdigitated Au electrodes, were fabricated in-house and connected to 40 CERDIP packages with Au wires. 3 μL of rGO (0.1 mg/mL in DMF) is dropped above the chip and, *via* dielectrophoresis (DEP; 10 V_{pp}, 300 kHZ, 10 seconds), rGO sheets were deposited between the interdigitated electrodes. Exfoliated carbon nitride was deposited above rGO on the devices by dropcasting 3 μL of exfoliated carbon nitride (0.1 mg/mL in H_2O) on top of the chip and evaporating off the solvent by placing the packaged chip on a 130ºC hotplate. Thickness of the carbon nitride layer above rGO can be controlled by the volume of solution dropcast, as well as the concentration of the solution.

*Oxygen sensing experiment set-up***.** Packaged rGO/carbon nitride chemiresistor chips were placed on a test board and sealed in a Teflon chamber. The test board was connected to a Keithley Dual SourceMeter 2602 and Keithley Switching Matrix 708A, which were controlled with Labview software. This set-up extracts 4 data outputs simultaneously, allowing changes in electrical conductance of each chemiresistor device to be collected with Zephyr data-acquisition

software (http://zephyr.sourceforge.net). Two gas flow controllers were used to control the concentration of oxygen in the Teflon test chamber. The diluting gas flow controller was connected to dry N_2 and the experimental gas flow controller was connected to dry air (for concentrations 1-5% O_2) or 1% O_2 in dry N_2 (for concentrations 0.05-0.5% O_2). In order to humidify the gas, a glass-fritted water bubbler filled with DI H_2O was connected in-line before the Teflon chamber, thus delivering 100% relative humidity at 21°C. The gas velocity was kept at 540 standard cubic centimeters per minute (sccm) for all experiments. The bias voltage for all experiments was 50 mV. For sensing experiments that provided calibration curve data, UV light was provided by a handheld lamp (Analytik Jena (UVP) UVGL-55). The longwave (365 nm) source was used at a distance of three inches, thus providing 950 $\mu W/cm^2$. In order to demonstrate the effect UV light power on the sensor performance, a longwave UV LED (LED Engin LZ1-10UA00-00U4, 385-390 nm) was used that provided irradiance of 4.2 mW/cm^2.

Characterization.

Electron microscopy. Transmission electron microscopy (TEM) samples were prepared by dropcasting 7 μL of diluted samples in water on TEM sample grids (carbon film, 400 mesh copper grid; Electron Microscopy Sciences). The TEM instrument model used was FEI Morgagni. Scanning electron microscopy (SEM) of rGO/carbon nitride was performed directly on the Si chip. The SEM instrument model used was ZEISS Sigma 500 VP.

Powder x-ray diffraction (PXRD). PXRD was performed on a Bruker D8 XRD system equipped with LynxEye detector. Powder carbon nitride on a glass slide was the sample tested. 2θ angles between 8° and 60° were measured at 0.02° intervals with a rate of 0.3 seconds/point. The x-ray source was Cu Kα held at 40 kV and 40 μA with a 0.2 mm aperture slit width.

Fluorescence spectroscopy. Photoluminescence measurements were obtained using a Nanolog spectrofluorometer (HORIBA Jobin Yvon) equipped with a xenon lamp (400 W) light source, double excitation monochromators, and R928 Hamamatsu visible light detector. In order to test solid samples, a custom-made integrating sphere with quartz tube solid sample holders was used as an accessor to the spectrofluorometer. Spectra were obtained by exciting the sample with a single wavelength (300, 320, 340, 360, or 380 nm) while the emission wavelength was scanned from 400 to 600 nm at 2 nm increments.

X-ray photoelectron spectroscopy (XPS). XPS was performed on an ESCALAB 250Xi. Carbon nitride powder samples were placed directly onto copper tape, which were subsequently fixed onto the XPS sample holder. rGO samples were dropcast from DMF solution onto copper foil and subsequently secured onto the XPS sample holder with copper tape. An electron flood gun was run simultaneously with the experiment to allow charge compensation. Survey, valence, high-res C_{1s} and N_{1s} were collected for carbon nitride samples. Survey and valence scans were collected for rGO. Valence scan was collected for Cu foil. Due to surface contamination on the surface of Cu and rGO, an Ar ion etching treatment (3000 eV, 60 seconds) was applied before collecting the XPS data.

4.4 RESULTS AND DISCUSSION

4.4.1 Carbon Nitride Characterization

Characterization of the as-synthesized carbon nitride material was done to determine whether the material was heptazine- or triazine-based, as well as whether it was condensed or uncondensed (Fig. 4.1). High resolution transmission electron microscopy (HRTEM) of the synthesized carbon nitride material shows a lattice spacing of 3.2 Å (Fig. 4.1a). Powder X-ray diffraction (PXRD) of the as-synthesized material displayed a pattern indicative of layered, graphitic-like sheets (Fig. 4.1b). Since melamine is an intermediate of "graphitic" carbon nitride synthesis, the absence of melamine peaks indicates that reaction went to full completion. The calculated d-spacing of the material is 3.2 Å matches the d-spacing for uncondensed, heptazine-based, graphitic carbon nitride (gh-$C_6N_9H_3$).[160] Bragg's law (Eq. 3) was used to derive d-spacing from the PXRD, where $\theta = 13.9^o$ (2θ of 002 peak / 2), $\lambda = 1.54$ Å (wavelength of X-ray source), and $n = 1$. Triazine-based graphitic-carbon nitride and condensed carbon nitride (g-C_3N_4) have larger d-spacings of 3.3-3.4 Å.[158, 161-162] The fluorescence emission of the as-synthesized material was measured in the range (300-380 nm) of long-wave UV excitation wavelengths (Fig. 4.1c). The emission peak is centered at 456 nm (2.72 eV) for each excitation wavelength, which corresponds well with the bandgap for pristine gh-$C_6N_9H_3$ (referred to as melon in cited reference).[163] The bandgap size of gh-$C_6N_9H_3$ is unique for non-metal materials since it is wide enough to photocatalyze numerous redox pairs, yet narrow enough to absorb visible light. Since proximate ^1H atoms are necessary for ^{13}C and ^{15}N CP-MAS solid-state NMR, the appearance of solid-state NMR peaks for the as-synthesized carbon nitride material supports the uncondensed structure of the material. The shifts of the peaks match well with previous literature examples.[160]

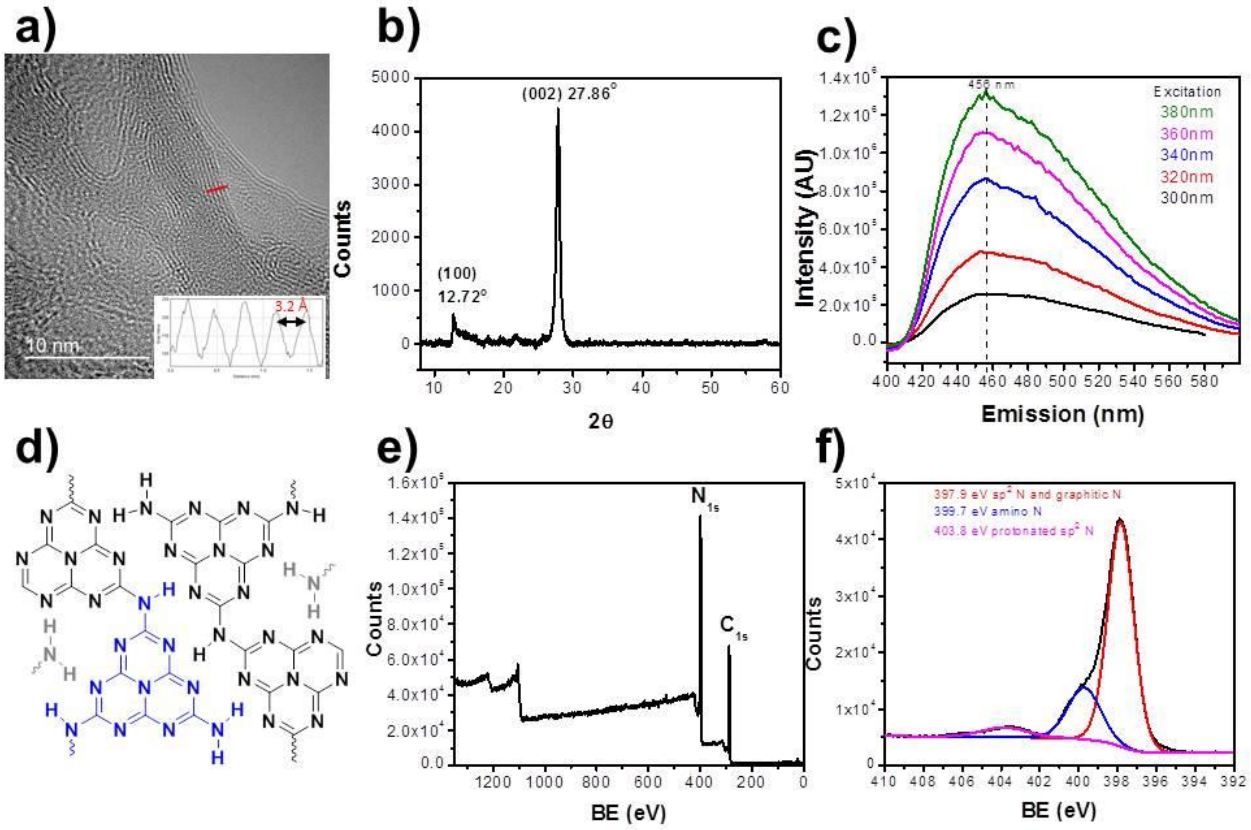

Figure 4.1 Characterization of synthesized graphitic carbon nitride. (A) HRTEM of exfoliated carbon nitride nanosheets. Inset: Gray scale plot profile of HRTEM cross-section (red line). Peak-to-peak distance (3.2 Å) shows lattice spacing of uncondensed carbon nitride. (B) XRD of as-synthesized carbon nitride material. (C) Fluorescence spectra of as-synthesized carbon nitride powder at different excitation wavelengths (300, 320, 340, 360, and 380 nm). (D) Unit cell of uncondensed graphitic carbon nitride with heptazine monomer (gh-$C_6N_9H_3$). (E) Survey scan of as-synthesized carbon nitride material exhibits N_{1s} peak (60 atomic %) and C_{1s} peak (40 atomic %). H_{1s} cannot be detected with XPS. (F) High-resolution scan of N_{1s} peak shows three deconvolved peaks: protonated sp^2 N (403.8 eV), sp^3 N (399.7 eV), and sp^2 N (397.9 eV). The sp^3 to sp^2 N ratio is ~2:7, which matches the unit cell N ratio of the corresponding species.

XPS of the as-synthesized carbon nitride material confirmed the chemical structure of the material by providing the C to N ratio and the ratio of sp^2 N/graphitic N to sp^3 N ($N(-H)_{1-2}$) (Fig. 4.1e, f). Two peaks, C_{1s} and N_{1s}, appear on the low-resolution survey XPS scan. No elemental impurities are detected. The ratio of carbon to nitrogen is 2C:3N, which is the empirical formula for uncondensed graphitic carbon nitride (C_2N_3H). Condensed graphitic carbon nitride (g-C_3N_4), on the other hand, has a C:N ratio of 3:4. The high-resolution N_{1s} XPS scan of carbon nitride was deconvolved into three peaks: 397.9 eV (pyridinic and graphitic N); 399.7 eV (amino N); and 403.8 eV (protonated pyridinic N). These N_{1s} peak assignments were made using previous literature assignments of N-functionalities on sp^2 carbon.[164-165] The unit cell for gh-$C_6N_9H_3$ (Fig. 4.1d) contains a total of 36 nitrogen atoms, of which 28 N atoms are pyridinic or graphitic, and 8 N atoms are amino (*i.e.* $N(-H)_{1-2}$). This composition (77.78% pyridinic plus graphitic N; 22.22% amino N) is closely matched by the high-resolution N_{1s} XPS peaks in which 78.19% of N atoms are pyridinic (including protonated)/graphitic N and 21.81% are amino N.

The XPS peak centered at 403.8 eV, which accounts for 2 of the 36 N atoms in the unit cell (Fig. 4.1d), can be explained by protonation of two pyridinic N atoms in the gh-$C_6N_9H_3$ unit cell. There are a total of six sp^2 N sites in the gh-$C_6N_9H_3$ unit cell where protonation can potentially occur. Pels *et al.* observed that positively-charged N species in pyrolyzed coals and chars led to XPS peaks similar to quaternary N peaks in the range of 401-405 eV.[165-166] In the case of carbon nitride, the peak at 404 eV has been attributed to positive charge localization on the heterocycle structure.[167] Protonation of sp^2 N in carbon nitride would lead to positive charge localization within the heptazine unit of the polymer.[168]

4.4.2 Carbon Nitride/rGO Chemiresistor

Sensor devices were prepared by sequentially depositing rGO and exfoliated carbon nitride between interdigitated gold electrodes. rGO sheets used in this work were between 0.5-2 μm wide and contained structural defects such as wrinkles and grain boundaries on the graphitic basal plane (Fig. 4.2a). The distance between interdigitated electrodes of the chemiresistor devices are 8 μm, thus requiring the deposition of several overlapping rGO sheets to bridge the electrodes. Effective deposition of rGO sheets between the interdigitated electrodes was tested by taking current-voltage (I-V) curves after the dielectrophoresis (DEP) procedure. A current in the μA range at 1 V was found to correspond to an ideal deposition, since lower currents represent an unreliably low concentration of rGO between the electrodes while higher currents represent an overabundance of rGO sheets resulting in sensor insensitivity.

Uniform distribution of carbon nitride nanosheets across the Si sensor chip was achieved with the dropcast procedure (Fig. 4.2c), which provided similar sensing behavior among the four chemiresistor devices. Exfoliation of the carbon nitride material was done with bath sonication of an aqueous dispersion. It was found that an hour of sonication was sufficient to exfoliate 1-3 μm carbon nitride sheets into 10-100 nm nanosheets. The carbon nitride nanosheets were found to deposit on the wrinkles and edges of the rGO sheet (Fig. 4.2 b, d). Wrinkles, grain boundaries, and edges of rGO are known to contain a higher concentration of defect sites and oxygen moieties as compared to flat basal plane regions of the rGO sheet.[169-170] The carbon nitride nanosheets can be removed off the rGO with a water wash, thus demonstrating the non-covalent nature of the carbon nitride/rGO interface. Ong *et al.* have shown that electrostatic interaction between protonated carbon nitride and the oxygen moieties on rGO is the dominant intermolecular force between the two materials.[171]

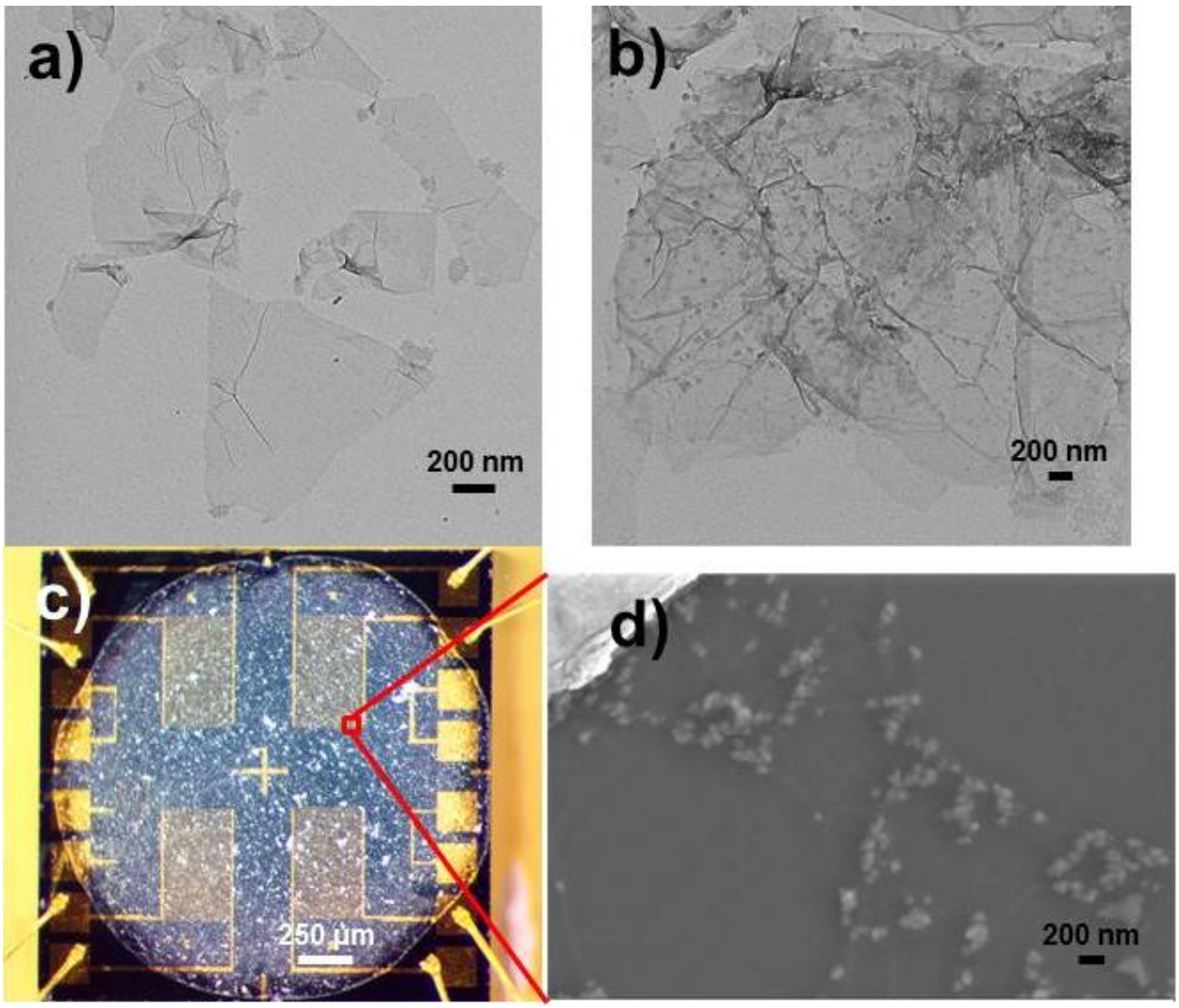

Figure 4.2 Sensing with carbon nitride/rGO. (a) TEM of bare rGO; (b) TEM of carbon nitride/rGO; (c) optical image of carbon nitride/rGO sensor chip; (d) SEM image of rGO decorated with carbon nitride nanosheets between two Au electrodes.

4.4.3 Oxygen Sensing with Carbon Nitride/rGO

Carbon nitride/rGO chemiresistor devices were tested in various gas environments with and without UV irradiation. Though carbon nitride can be photoexcited with visible light, longwave UV light (365-390 nm) was used in this work because UV light has a cleaning effect on graphene by removing surface contaminants.[172] When the carbon nitride/rGO chemiresistor was irradiated with UV light in a humid N_2 environment, a sharp increase in electrical conductance was observed (Fig. 4.4a). In the same experiment a saturation point in conductance is reached after 15 minutes of UV irradiation (950 $\mu W/cm^2$), which is more than double the initial conductance measured before UV irradiation. UV light is known to photoexcite carbon nitride;[173] therefore, the increase in the chemiresistor's conductance can be explained by photogeneration of charge carriers in the carbon nitride nanosheets and subsequent transfer of charge carriers into the rGO transducer. In a humid nitrogen environment, the carbon nitride/rGO chemiresistor recovers back towards its baseline once UV light is removed. UV irradiation of a bare rGO chemiresistor showed a small decrease in conductance (Fig. 4.3a), likely due to UV light's cleaning effect of surface contaminants. Therefore, the two-fold conductance increase of the carbon nitride/rGO chemiresistor under UV light is the result of charge carrier photogeneration in carbon nitride nanosheets. Likewise, the carbon nitride/rGO chemiresistor in dry nitrogen conditions also rose in conductance when irradiated with UV light; however, once the UV light was removed the chemiresistor shows little to no recovery back to baseline (Fig. 4.3b). The difference between baseline recovery post-UV light in humid nitrogen versus dry nitrogen indicates that H_2O, or O_2 evolved from H_2O oxidation, is responsible for the baseline recovery.

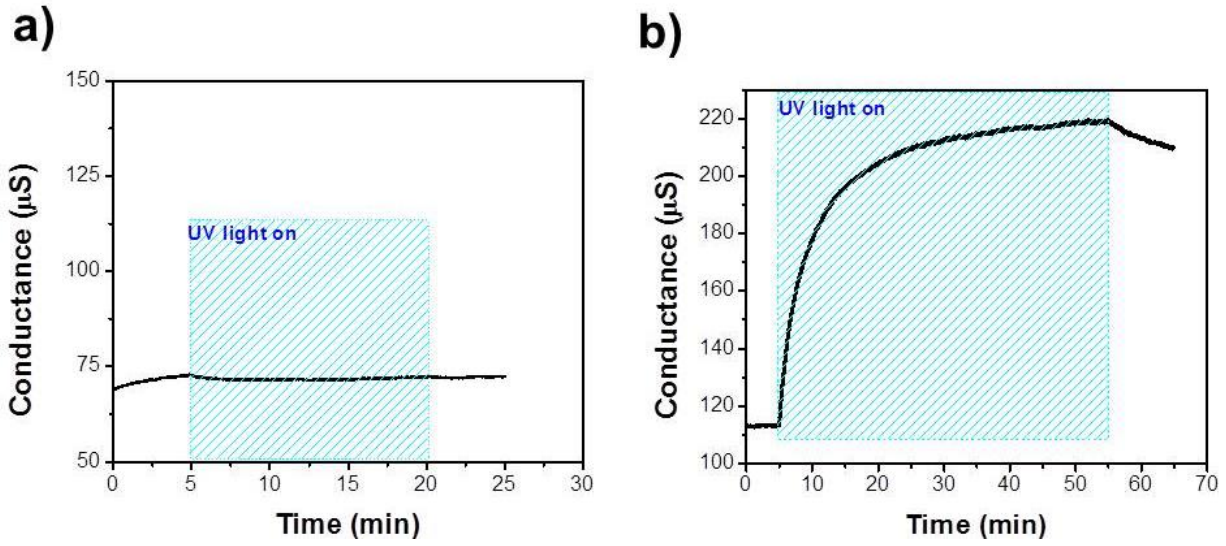

Figure 4.3 Photoirradiation without carbon nitride or humidity. (a) Conductance response curve of bare rGO deposited on a chemiresistor device while irradiated with UV light for 15 minutes in humid N_2 background; (b) conductance response curve of carbon nitride/rGO deposited on a chemiresistor device while irradiated with UV light for 40 minutes in dry N_2 background.

Exfoliation of graphitic carbon nitride into nanosheets had an effect on the chemiresistor's photoexcitation behavior. Non-exfoliated graphitic carbon nitride/rGO chemiresistor in humid nitrogen showed a 32% increase in conductance when irradiated with UV light for five minutes. In comparison, exfoliated carbon nitride/rGO chemiresistor increased by 160% when irradiated with UV light for five minutes (Fig. 4.4a). This large difference in photoexcitation between non-exfoliated and exfoliated carbon nitride can be explained by several possible effects: 1) exfoliated carbon nitride absorbs more UV light than non-exfoliated carbon

nitride due to a shift in bandgap;[155] 2) exfoliation of carbon nitride into nanosheets "unstacks" carbon nitride such that there is a larger carbon nitride surface area; or 3) carbon nanosheets are able to form a better interface with rGO than non-exfoliated sheets due to their size (10-100 nm vs. 1-3 μm).

As charge transfer from UV-irradiated carbon nitride into the rGO transducer was hypothesized, the carbon nitride/rGO chemiresistor was exposed to oxygen gas in both dry and humid conditions. Oxygen is an oxidizing gas that will react with photoexcited electrons if their potential is large enough. In dry N_2 background, 5% oxygen exposures with and without UV irradiation showed little to no effect on chemiresistor's conductance (Fig. 4.4b). Likewise, in humid N_2 background without UV irradiation, 5% oxygen exposure had little effect on the chemiresistor. In contrast, under humid conditions and UV light, the carbon nitride/rGO chemiresistor showed a large drop in conductance when exposed to oxygen (Fig. 4.4c). In the same experiment the conductance of the chemiresistor was found to increase once the oxygen exposure ended. A reversible response indicates that oxygen gas is not irreversibly adsorbed, but rather reacts with photoexcited electrons. From this set of experiments it was determined that humidity and UV irradiation are necessary for O_2 sensitivity.

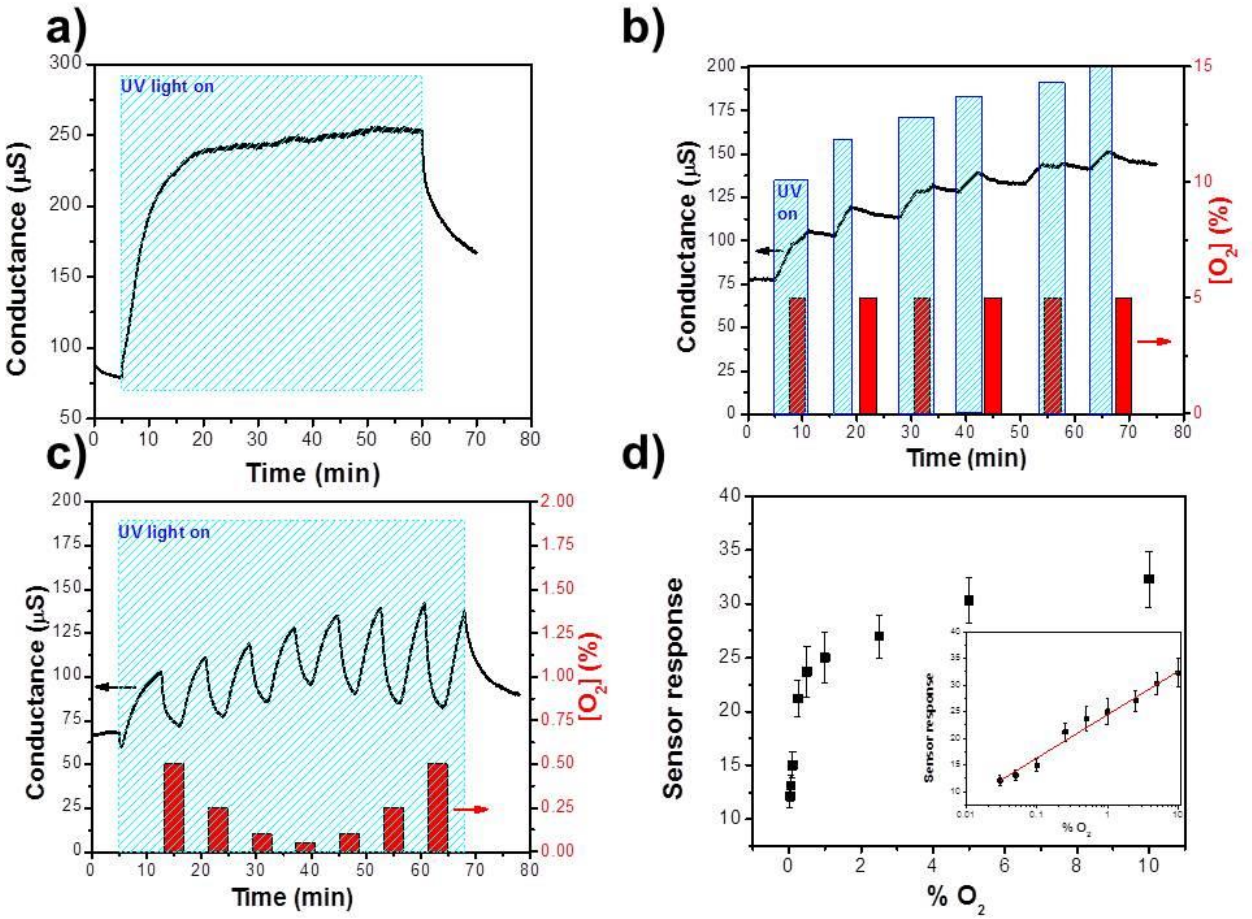

Figure 4.4 Conductance measurements of chemiresistor devices. (a) Carbon nitride/rGO in humid N_2; (b carbon nitride/rGO with 3 min exposures of O_2 in dry N_2; (c) carbon nitride/rGO with 3 min exposures of different O_2 concentrations in humid N_2; (D) sensor response (see Eq. 5) vs. O_2 concentration of carbon nitride/rGO chemiresistor. Inset: X-axis changed to logarithmic scale to illustrate the logarithmic dependence of the sensor response

A set of 3-minute exposures of oxygen concentrations ranging from 300-100,000 parts per million by volume (ppm_v) were tested with a carbon nitride/rGO chemiresistor chip. Each chip contains four chemiresistor devices which provide four simultaneous sensor responses to every oxygen exposure. The experimental data shown in Fig. 4.4c is representative of the data used to form the oxygen sensor calibration curve shown in Fig. 4.4d. The data shown in Fig. 4.4c is the conductance change from one of the four devices on the chemiresistor chip exposed to O_2 concentrations between 0.5% and 0.05%. The response (Eq. 5) of the chemiresistor in the first minute of oxygen exposure was found to be logarithmically proportional to oxygen concentration (Fig. 4.4d). For Eq. 5, G_0 is conductance of the chemiresistor at t=0 minutes after oxygen exposure, while G_1 is conductance at t=1 minute after oxygen exposure.

$$sensor\ response = \frac{G_0 - G_1}{G_0} * 100\% \quad \text{(Eq. 5)}$$

The limit of quantification (LOQ) for this sensor, assuming the logarithmic function (Eq. 6) continues for concentrations <300 ppm, was found to be 20 ppm. LOQ was determined as the oxygen concentration that exceeds ten times the standard deviation of the blank ($10SD_{blank}$ = 0.015).

$$sensor\ response = 3.575 \ln(O_2\ \text{vol}\%) + 24.59 \quad \text{(Eq. 6)}$$

Response and recovery time of the sensor can be improved by increasing the power of the UV light source. When the UV light source was changed to an LED (4.2 mW/cm^2; Fig. 4.5b), the sensor's response and recovery times improved to 38 and 39 seconds, respectively, for exposure to 0.1% O_2 (Fig. 4.5a). This result suggests that the rate of charge carrier photogeneration, which is proportional to UV light power, is directly correlated with sensor performance.

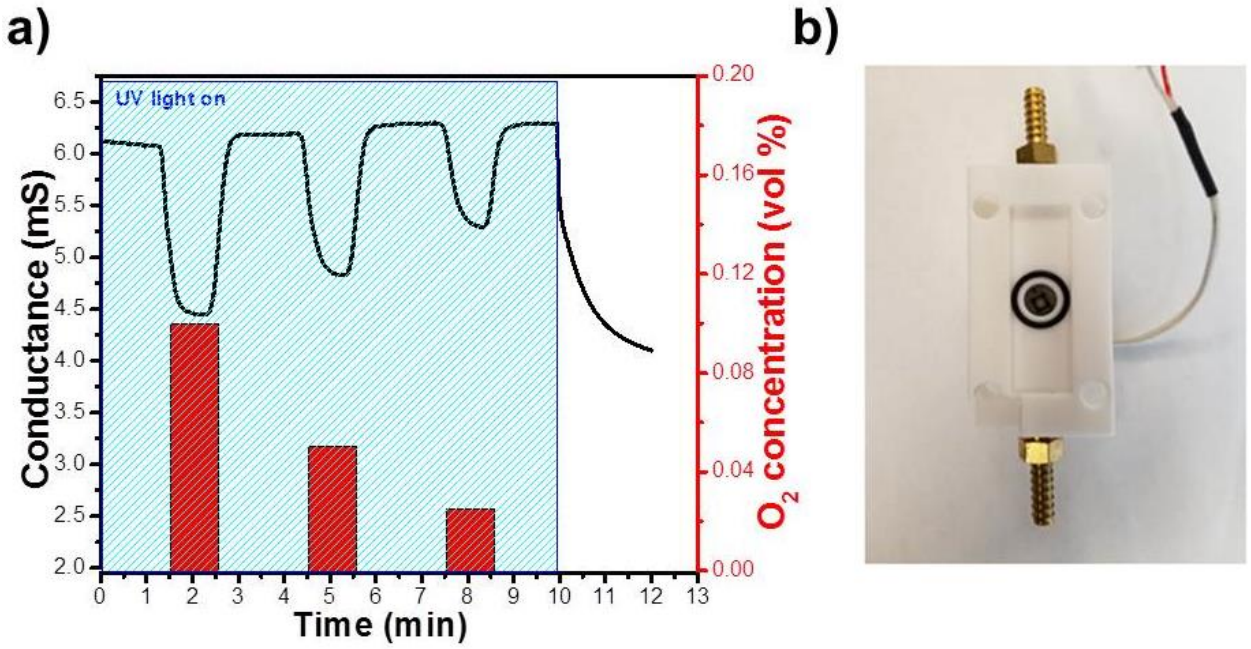

Figure 4.5 The effect of light power in carbon nitride/rGO oxygen sensing. (a) Carbon nitride/rGO chemiresistor O_2 sensing performance in humid N2 using UV LED; (b) photograph of gas flow chamber with built-in UV LED.

4.4.4 Oxygen Sensing Mechanism

Kofuji *et al.* studied a similar system of carbon nitride on rGO, albeit in a photoelectrochemical set-up.[174] Their results showed that photoexcited electrons are generated in carbon nitride and transferred to the rGO sheet. In their photocatalyst experiment, photogenerated holes remain on carbon nitride and oxidize water to oxygen gas, while the photogenerated electrons reduce

oxygen to hydrogen peroxide on the rGO surface. The same charge separation from carbon nitride to rGO was observed in this work. It is this charge transfer to rGO that makes the chemiresistor sensitive to oxygen gas since bare rGO shows no response to O_2, whether with or without UV irradiation. Charge transfer from carbon nitride to rGO was evidenced by a large conductance increase of the carbon nitride/rGO chemiresistor under UV irradiation. In dry nitrogen background the conductance remains elevated even after the UV light is removed, indicating that charge recombination between photogenerated electrons and holes does not occur once the photogenerated electrons are separated in the carbon nitride/rGO system. Estimation of carbon nitride and rGO's approximate Fermi levels from literature precedent allows the comparison of each material's electronic bands against a standard electrode potential (Fig. 4.6).[35, 175] Carbon nitride is a semiconductor with a ~2.7 eV bandgap while rGO is a semi-metal with little to no bandgap. Charge transfer from carbon nitride's conduction band to rGO places photoexcited electrons at a potential exceeding that of 4-e^- reduction potential of O_2. From a Koutecky-Levich plot, the calculated electron transfer number, n = 2.30, indicates a 2 e^- reduction process. This result is comparable to the findings of Kofuji *et al.*, who found n = 2.10 for their carbon nitride/rGO material.[174] In humid conditions, photogenerated holes on carbon nitride oxidize water to O_2. Water oxidation provides protons, thus allowing photoexcited electrons on rGO to reduce O_2 to H_2O or H_2O_2. The absence of protons in dry conditions prevents oxygen reduction, which corresponds to the lack of oxygen sensitivity in dry conditions (Fig. 4.4b). Recovery toward baseline once UV irradiation is removed (Fig. 4.3a and 4.4a) can also be understood with the photoredox mechanism. In humid conditions a small concentration of O_2 is present due to water oxidation, while dry conditions are always anaerobic unless O_2 is introduced. According to the photoredox mechanism (Fig. 4.6), the sensor should have a

response to O_2 concentrations as long as the rate of O_2 reduction exceeds the rate of charge transfer from carbon nitride to rGO.

The carbon nitride/rGO chemiresistor showed little to no response to large concentrations (5 vol%) of H_2 or CO_2. There was a small sensor response toward H_2 gas only when the carbon nitride/rGO system was irradiated with UV light. Reducing gases cannot react with photogenerated electrons transferred to the rGO conduction band, but may react with the photogenerated holes remaining in the carbon nitride valence band. Oxidative splitting of H_2 gas on the carbon nitride layer would hydrogenate the carbon nitride layer and thus slow the rate of electron/hole pair photogeneration. This indirect photoredox sensing mechanism occurring on the carbon nitride layer rather than the rGO layer would explain why the sensor response toward H_2 gas is only a tenth the response toward the same concentration of O_2 gas. CO_2, on the other hand, is an oxidizing gas but the reduction potential for CO_2 is much greater than the reduction potential for O_2. While the reduction potentials for O_2 fall near rGO's work function, the reduction potentials for CO_2 are much closer to H^+ reduction potential, thus making the chemiresistor unresponsive to CO_2. This result shows how the photoredox sensing mechanism allows selectivity to be tuned based on the location of the transducer's Fermi level on the energy scale.

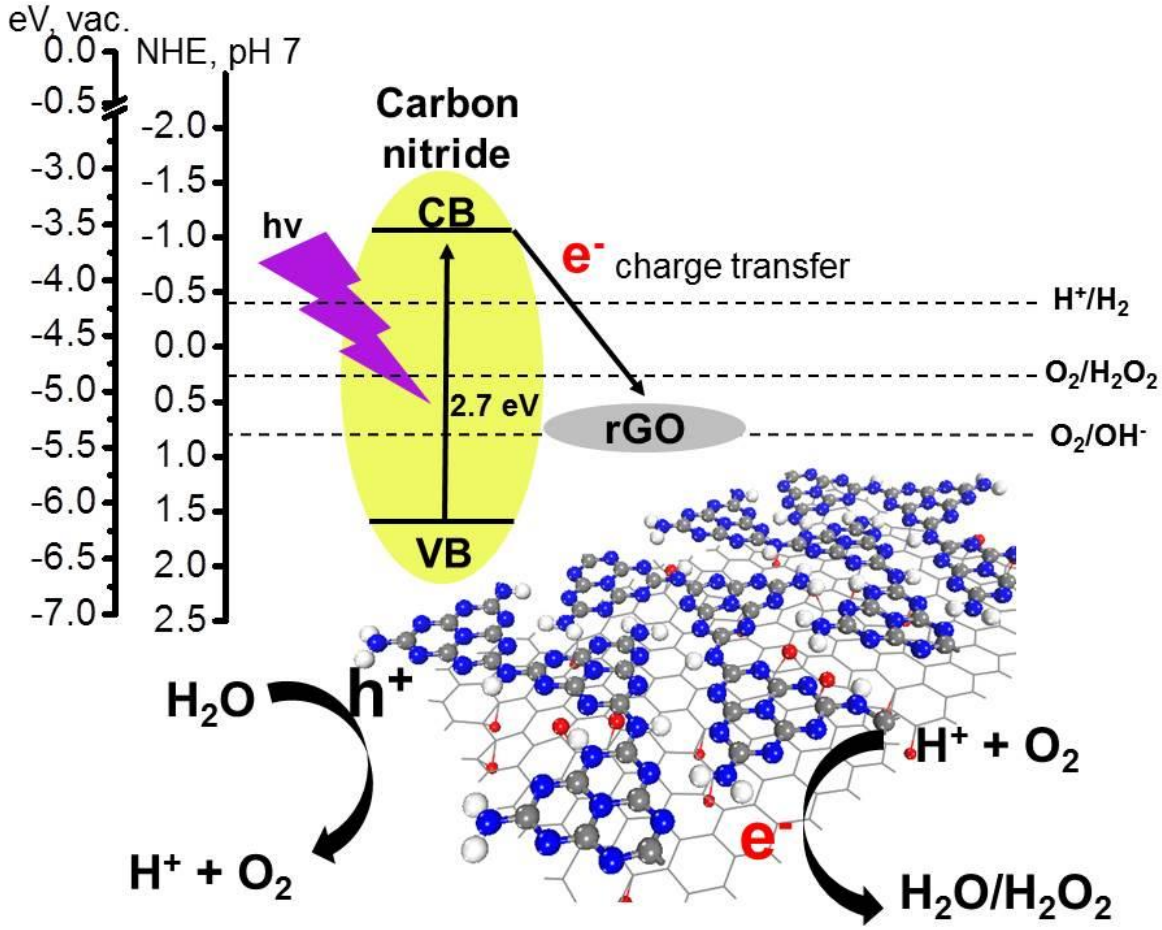

Figure 4.6 Schematic illustration of photoredox mechanism for oxygen sensing on photoexcited carbon nitride/rGO.

4.5 CONCLUSION

In this work, it was shown that uncondensed graphitic carbon nitride (melon) coupled to rGO can sense oxygen gas within the concentration range of 300-10,000 ppm. Through XRD, fluorescence spectroscopy, and XPS characterization it was determined that the as-synthesized carbon nitride material was heptazine-based uncondensed graphitic carbon nitride (gh-$C_6N_9H_3$). XPS characterization, especially N_{1s} XPS, provided structural insight into the degree of sp^2 N protonation on the synthesized carbon nitride. The N_{1s} peak centered at 403.8 eV was found to be correlated with positive charge localization caused by protonation of pyridinic N sites. The as-synthesized carbon nitride material was exfoliated into nanosheets *via* bath sonication, which proved to have an advantageous effect toward sensing application. Carbon nitride/rGO chemiresistor devices were prepared and tested for oxygen sensitivity in humid and dry conditions with and without UV irradiation. UV irradiation doubled the measured conductance of the carbon nitride/rGO chemiresistor due to charge transfer of photoexcited electrons from carbon nitride nanosheets to the rGO transducer. The carbon nitride/rGO chemiresistor significantly dropped in conductance whenever exposed to oxygen gas in humid conditions and under UV irradiation. A photoredox mechanism wherein water is oxidized on the carbon nitride surface and oxygen is reduced on the rGO surface explains the chemiresistor behavior observed. The chemiresistor's response to oxygen was found to be logarithmically proportional to oxygen concentration in the range 300-100,000 ppm. A close electrical interface between two materials like the one observed in this work is a crucial feature for sensing, photocatalysis, and photovoltaic applications.

5.0 MODIFYING THE ELECTRONIC STRUCTURE OF CARBON NITRIDE/REDUCED GRAPHENE OXIDE VAN DER WAALS HETEROSTRUCTURE WITH COPPER NANOPARTICLES

5.1 CHAPTER PREFACE

The following chapter has been adapted from a completed manuscript that is yet to be submitted to a journal

List of contributors: James E. Ellis, Seth C. Burkert, Alexander Star

Contributions: JEE and AS designed the experiments. JEE performed all experimental work. SCB collected SEM images of the material. JEE and AS wrote the manuscript.

5.2 INTRODUCTION

Van der Waals heterostructures (vdWH) are a class of material composites in which neighboring two-dimensional materials are weakly bound through van der Waals interactions.[75] Without the constraints of lattice matching and process compatibility, combining any two-dimensional metal, semiconductor, or insulator layer with another becomes feasible, thus allowing a variety of different heterostructures. "Graphitic" carbon nitride/graphene is a metal-free vdWH with a semiconductor/semi-metal heterojunction. Carbon nitride/graphene vdWHs demonstrate large photocurrents, indicating high charge separation across the heterojunction. This charge separation solves carbon nitride's high recombination rate, thus greatly improving its photocatalytic activity toward hydrogen evolution reaction (HER)[176-178] and oxygen reduction reaction (ORR).[179] In a previous publication, we demonstrated high charge separation across a carbon nitride/reduced graphene oxide (rGO) heterojunction and applied it toward oxygen gas sensing in a chemiresistor device.[180] The sensing mechanism for carbon nitride/rGO is a photoredox reaction wherein, in the presence of water vapor and light, photoexcited electrons transferred to rGO's conduction band reduce oxygen gas. The rate of oxygen reduction affects the photocurrent of the chemiresistor device, thus allowing a calibration curve to be created between oxygen concentration and sensor response. While this carbon nitride/rGO vdWH sensor demonstrated oxygen sensitivity, no response was observed toward carbon dioxide.

The ubiquity of carbon dioxide in combustion processes, earth's atmosphere, and human respiration has created an important need for reliable CO_2 detection. However, CO_2 remains a difficult target analyte for chemiresistor detection because of its relatively inert redox behavior and nonpolarity. The few examples of CO_2 chemiresistive sensors rely on adsorption and charge transfer to metal oxide films and require high operating temperatures.[181-182] In the case of carbon

nitride/rGO vdWH, photoexcited electrons are energetic enough to react with CO_2, thus eliminating the need for high operating temperature; however, CO_2 adsorbs poorly on graphitic surfaces such as rGO. A method to increase gas sensing selectivity and sensitivity for graphene-based sensors is to append metal nanoparticles (NPs). Addition of metal NPs on graphitic surfaces are known to modulate the electronic structure of the composite, as well as create more adsorbed species close to the graphitic surface. The addition of metal NPs to graphene and rGO has been shown to improve the sensing performance toward inorganic gases such as H_2, NO_2, and NH_3.[183-184]

In this work, we turned to heterogeneous catalysis literature to find a metal surface known to effectively adsorb and reduce CO_2. Copper (Cu) metal is a surface that has been studied extensively for its CO_2 reduction behavior because of its reasonable current density and efficiency, and its hydrocarbon product selectivity.[185-186] Inspired by these findings, Shown *et al.* decorated graphene oxide (GO) with CuNPs and demonstrated a factor of greater than 60 times enhancement in CO_2 to fuel conversion as compared with using pristine GO.[187] This catalytic enhancement was attributed to charge transfer from Cu NPs d-orbital to the CO_2 (C—O) π^* orbital, which is a known mechanism of carbon dioxide reduction on metal NPs.[188]

5.3 EXPERIMENTAL SECTION

Carbon nitride synthesis and exfoliation: dicyandiamide (DCDA, 99% purity, 1 g; Sigma-Aldrich) was placed in an open quartz boat, which was subsequently placed in a quartz tube. The quartz tube atmosphere was replaced with argon, and the tube was sealed on both ends by water bubblers. The sample was heated in a CVD furnace (Lindberg blue 3-zone furnace) for 2 h at

550°C and left to cool overnight. The remaining pale-yellow solid (~140 mg) was recovered from the quartz boat and ground in a mortar and pestle for ~10 min to yield a fine powder. For exfoliation of the bulk sheets into nanosheets, the resultant carbon nitride powder was dispersed in nanopure water (100 μg/mL) and sonicated in a bath sonicator (Branson 1510) for 1 h.

Bare rGO synthesis: graphene oxide (5 mL, 3 mg/mL in H_2O; Graphene Supermarket) was stirred with 5 μL of hydrazine hydrate (ca. 51% hydrazine; Acros Organics) in an 80°C oil bath for 3 h. The black precipitate (rGO) was collected through vacuum filtration and dispersed in DMF.

CuNP@rGO synthesis: graphene oxide (1 mL, 5 mg/mL in H_2O; Graphene Supermarket) was stirred with 0.2M NaOH (2 mL) and $CuSO_4 \cdot 5H_2O$ (15 mg; Sigma Aldrich) for 1.5 hours in a ~70ºC oil bath. 5 μL of hydrazine hydrate (ca. 51% hydrazine; Acros Orgranics) is added and the reaction vial is left in the oil bath for 40 minutes. The resulting black/red material is collecting with vacuum filtration and washed with ethanol and DMF. The collected material is dispersed in 10 mL DMF. After 3 days, the CuNP@rGO material precipitates while unreacted rGO remains dispersed. The unreacted rGO is removed and discarded and the precipitated CuNP@rGO is resuspended in 10 mL DMF with brief sonication.

Preparation of chemiresistor devices: Si chips, each containing 4 devices with interdigitated Au electrodes, were fabricated in-house and connected to 40 CERDIP packages with Au wires. A 2 μL portion of CuNP@rGO (or bare rGO) (0.1 mg/mL in DMF) is dropped above the chip, and via dielectrophoresis (DEP; 10 Vpp, 300 kHz, 10 s), CuNP@rGO sheets (or bare rGO sheets) were deposited between the interdigitated electrodes. Exfoliated carbon nitride was deposited above CuNP@rGO (or rGO) on the devices by dropcasting 3 μL of exfoliated

carbon nitride (0.1 mg/mL in H_2O) on top of the chip and evaporating off the solvent by placing the packaged chip on a 130°C hot plate.

Carbon dioxide-sensing experiment setup: Packaged carbon nitride/CuNP@rGO (or rGO) chemiresistor chips were placed on a test board and sealed in a Teflon chamber. The test board was connected to a Keithley Dual SourceMeter 2602 and Keithley Switching Matrix 708A device, which were controlled with Labview software. This setup extracts 4 data outputs simultaneously, allowing changes in electrical conductance of each chemiresistor device to be collected with Zephyr data-acquisition software (http://zephyr.sourceforge.net). Two gas-flow controllers were used to control the concentration of carbon dioxide in the Teflon test chamber. The diluting gas-flow controller was connected to dry N_2, and the experimental gas-flow controller was connected to 10% CO_2 in dry N_2. For humidification of the gas, a glass-fritted water bubbler filled with DI H2O was connected in-line before the Teflon chamber, thus delivering 100% relative humidity at 21°C. The gas velocity was kept at 540 standard cubic centimeters per minute (sccm) for all experiments. The bias voltage for all experiments was 50 mV. UV light was provided by a long-wave UV LED (LED Engin LZ1-10UA00-00U4, 385−390 nm), which provided irradiance of 4.2 mW/cm^2.

Characterization Methods:

X-ray photoelectron spectroscopy (XPS): XPS was performed on an ESCALAB 250Xi. Carbon nitride powder samples were placed directly onto copper tape, which were subsequently fixed onto the XPS sample holder. CuNP@rGO and bare rGO samples were dropcast from DMF solution onto aluminum foil and subsequently secured onto the XPS sample holder with copper tape. For the carbon nitride sample, an electron flood gun was run simultaneously with the experiment to allow charge compensation. Survey and valence scans were collected for each

sample. Because of surface contamination on the surface of Cu and rGO, an Ar ion etching treatment (3000 eV, 60 seconds) was applied before collecting the XPS data.

Ultraviolet photoelectron spectroscopy (UPS): UPS was performed on an ESCALAB 250Xi. The XPS samples (preparation mentioned above) were also used for UPS. The UV source was a HeI emission line (21.2 eV). The band pass energy was 40 eV and no sample bias voltage was applied. An electron flood gun was used on the carbon nitride sample to allow charge compensation.

5.4 RESULTS AND DISCUSSION

5.4.1 Preparation of CuNP@rGO

In order to make the previous carbon nitride/rGO vdWH discussed in chapter 4 sensitive to CO_2, CuNPs were attached to rGO through a simultaneous chemical reduction process of $CuSO_4$ and GO.[189] This method allows electrostatic interactions to occur between Cu^{2+} and the negatively charged oxygen moieties on GO before the reducing agent is added, thus creating nucleation sites for further CuNP growth on the rGO sheet. Without a capping agent, a distribution of Cu NP diameters ranging from 80 nm—1 μm with an average diameter of ~300 nm are observed on the CuNP@rGO material (Fig. 5.1a). According to an XPS survey scan, the surface of the synthesized CuNP@rGO is 9.6% Cu, 81.2% C, and 9.2% O.

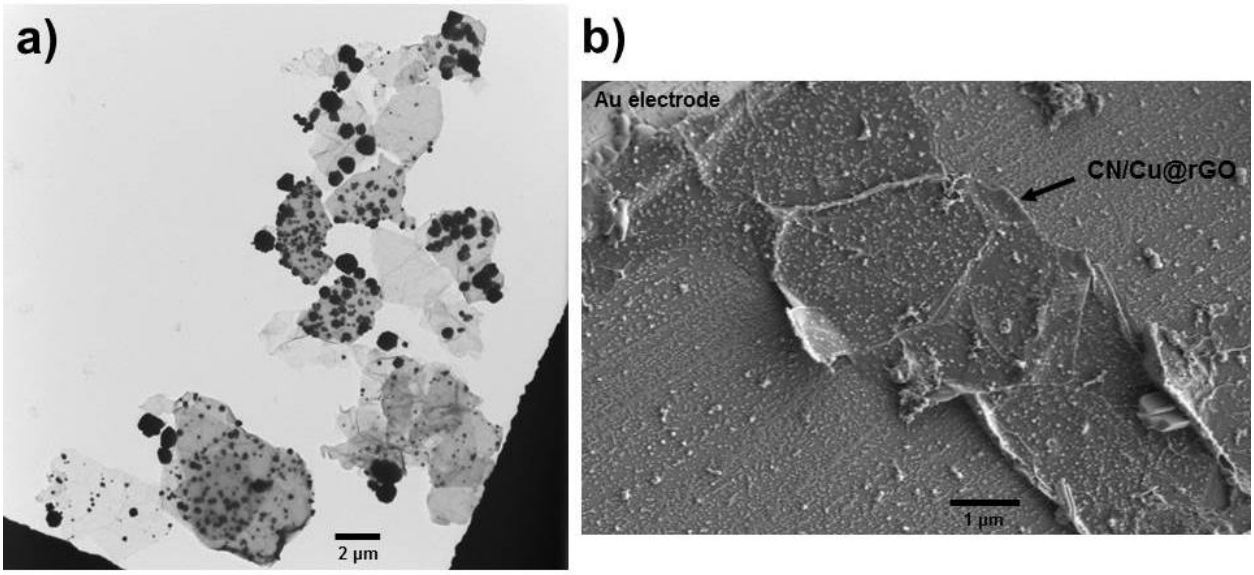

Figure 5.1 Cu NP@rGO and carbon nitride/CuNP@rGO. a) TEM of Cu NP@rGO material; b) SEM image of multiple carbon nitride/Cu NP@rGO sheets deposited on a Si-substrate chemiresistor device.

5.4.2 Electronic Structure Analysis of Carbon Nitride/CuNP@rGO vdWH through Photoelectron Spectroscopy

Ultraviolet photoelectron spectroscopy (UPS) was used to determine the work function (Φ_m) of the semimetals rGO and CuNP@rGO, as well as the ionization energy or valence band maximum (VBM) of carbon nitride. Whereas XPS is conventionally referenced to vacuum level, UPS is referenced to Fermi energy, thus allowing the work function to be measured. For both XPS and UPS the spectrometer work function (Φ_{sp}) must be accounted for when determining the

work function of the sample. The binding energy (E_B) of a sample electron can be calculated with the following equation:

$$E_B = h\nu - E_K - \Phi_{sp} \quad \text{(Eq. 7)}$$

A HeI emission UV source (21.2 eV) was used to collect UPS spectra for rGO, CuNP@rGO, and carbon nitride. The sample's maximum binding energy and minimum binding energy in a UPS spectrum are given as

$$E_{B,\,max} = h\nu - \Phi_{sp} \quad \text{(Eq. 8)}$$

$$E_{B,\,min} = \Phi - \Phi_{sp} \quad \text{(Eq. 9)}$$

Therefore, the work function of a metal or the VBM of a semiconductor can be determined by subtracting the UPS spectrum width from the UV source energy.

$$\Delta E = E_{B,\,max} - E_{B,\,min} = h\nu - \Phi \quad \text{(Eq. 10)}$$

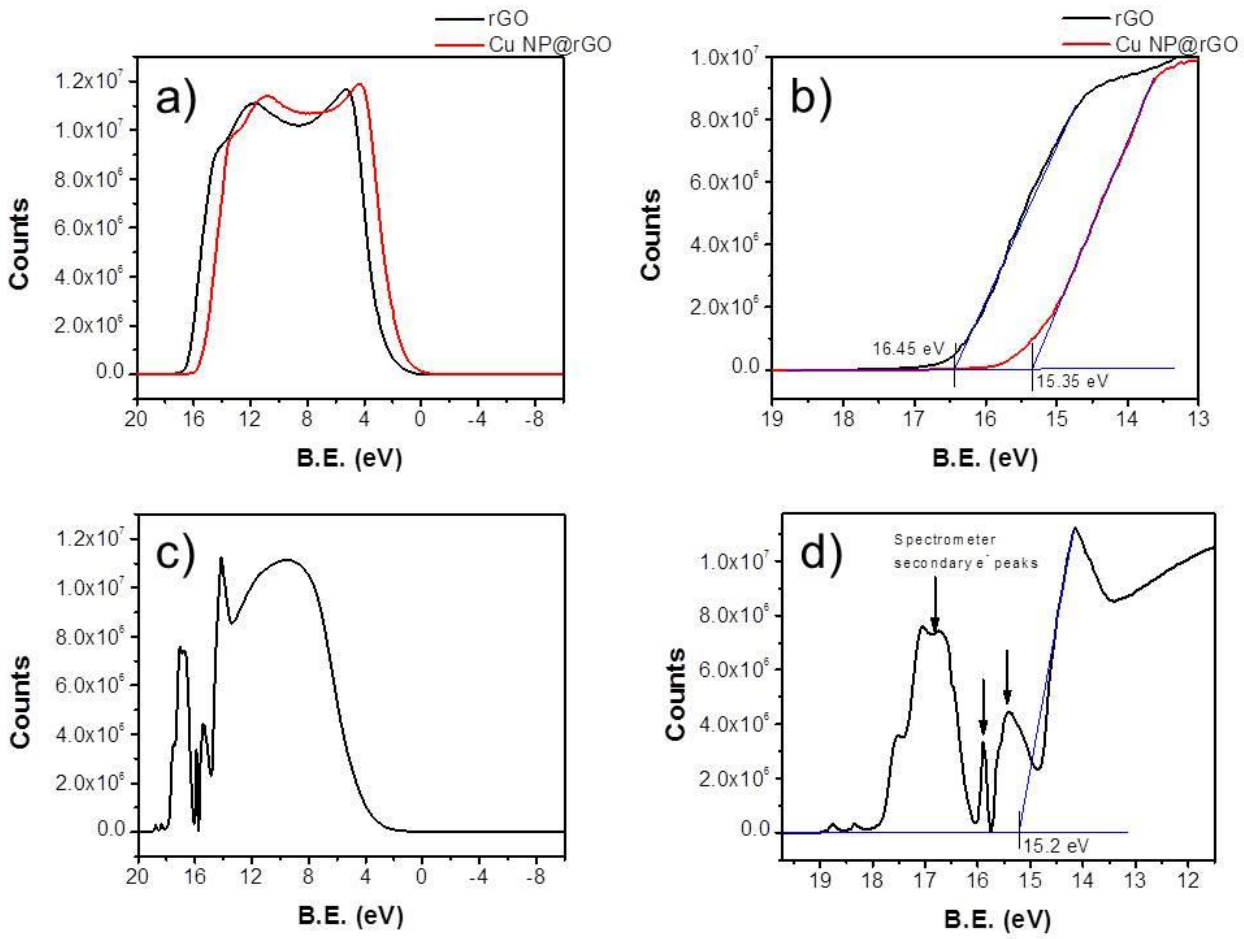

Figure 5.2 UPS of bare rGO, Cu NP@rGO, and carbon nitride. a,c) UPS spectra of rGO, Cu NP@rGO, and carbon nitride; b, c) secondary e- cut-off of rGO, Cu NP@rGO, and carbon nitride.

The UPS spectra for the rGO and CuNP@rGO samples were dominated by secondary electron emission from the sample (Fig. 5.2a, b); however, it was still possible to calculate ΔE from the observed secondary electron cut-off. The calculated work function for rGO (4.75 eV) agrees well with literature values, which range between 4.2 eV and 5.5 eV depending on heteroatom content and reduction method.[35] As compared to rGO, the secondary electron cut-off for CuNP@rGO was shifted 0.9 eV toward the Fermi level, indicating a larger work function. This shift may be caused by either the higher oxygen content of CuNP@rGO (9.2 O% vs. 4.7 O% for rGO), a p-doping effect caused by CuNPs, or a combination of these effects. The calculated VBM of carbon nitride (5.85 eV) places the valence band right below the oxidation potential of water (vs. NHE, pH=0), which is an important requirement for light driven CO_2 reduction. The bandgap for the synthesized carbon nitride, determined in our previous publication,[180] was found to be 2.7 eV, which would place the conduction band minimum (CBM) at 3.3 eV. The large difference between CuNP@rGO's work function and carbon nitride's CBM should results in charge transfer of photoexcited electrons from carbon nitride to CuNP@rGO.

Valence XPS was taken of CuNP@rGO to confirm the presence of d-band electrons. Valence XPS of Cu foil shows a very large, narrow peak near the Fermi level, which is indicative of d-band electrons in transition metals (Fig. 5.3b).[190] A large, narrow peak is detected in the valence scan for CuNP@rGO, thus demonstrating the presence of 3d valence electrons in the hybrid material (Fig. 5.3a). Valence XPS spectra of carbon nitride and bare rGO on the other hand are broad, low intensity, and include several peaks (Fig. 5.3c, d).

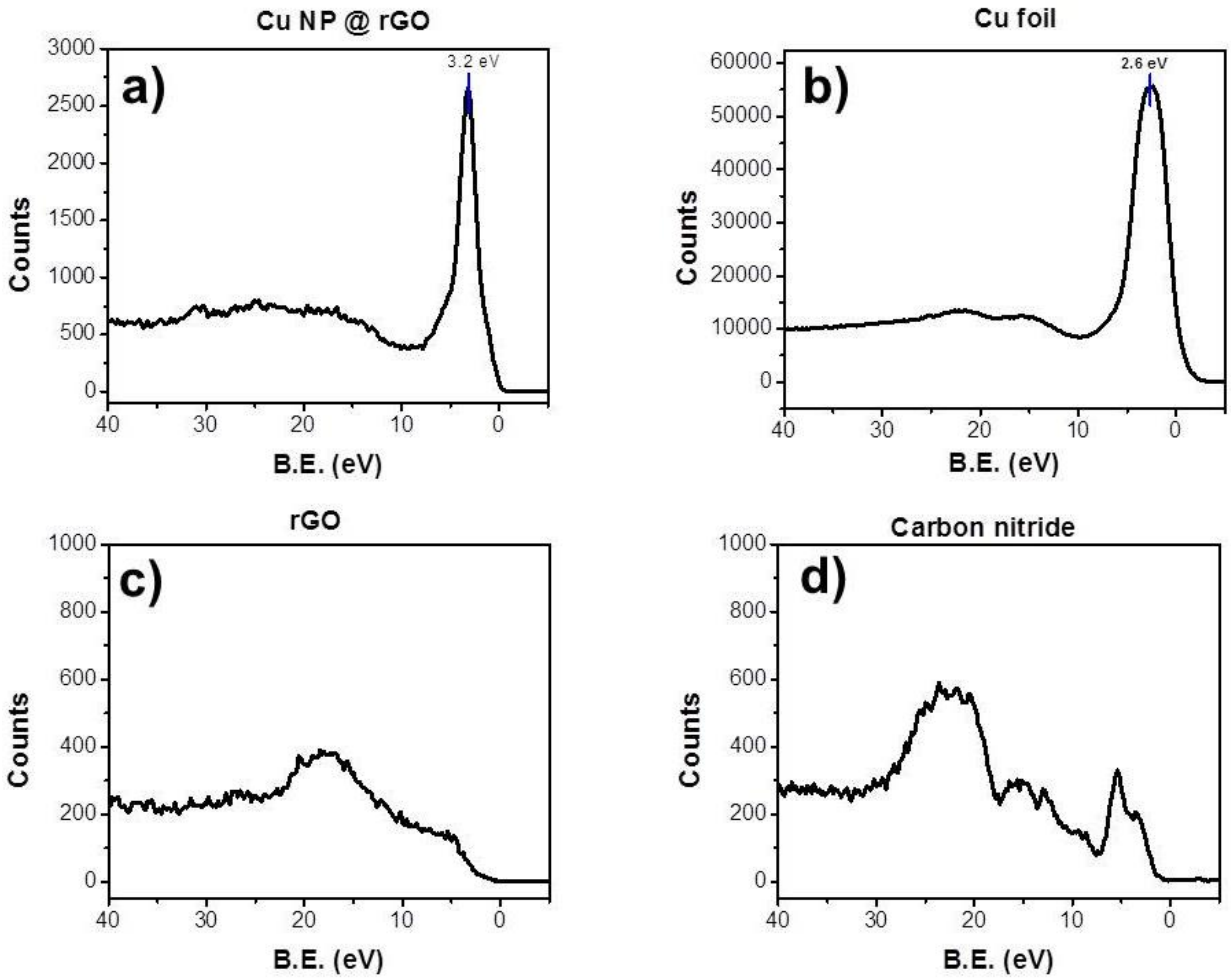

Figure 5.3 Valence XPS of Cu NP@rGO. a) Cu NP@rGO (d-band center: 3.2 eV), b) copper foil (d-band center (2.8 eV), c) rGO, and d) carbon nitride.

5.4.3 Carbon Dioxide Sensitivity of Carbon Nitride/CuNP@rGO

In our previous work with carbon nitride/rGO vdWH, we found that oxygen sensitivity only occurred when carbon nitride/rGO was in a humid environment and illuminated with light (395 nm). Without humidity, a photocurrent was observed when carbon nitride/rGO was irradiated,

but no change in conductance occurred when the device was exposed to O_2. Water vapor was necessary for the photoredox sensing of O_2 because it served as both an electron and proton donor for the photoreduction of O_2 on the rGO layer. This mechanism was previously observed for carbon nitride/rGO vdWH by Kofuji *et al.*,[179] wherein H_2O is oxidized by photogenerated holes localized on the carbon nitride layer and O_2 is reduced by photogenerated electrons localized on the rGO layer; however, their experiments were done in a photoelectrochemical setting rather than a chemiresistor device like that used in our work. When carbon nitride/rGO vdWH was exposed to CO_2, either irradiated or non-irradiated, there was no discernible chemiresistor signal (Fig. 5.4a). The absence of a signal may be caused by poor CO_2 chemisorption on rGO or the reduction potential for CO_2 reduction being too high.

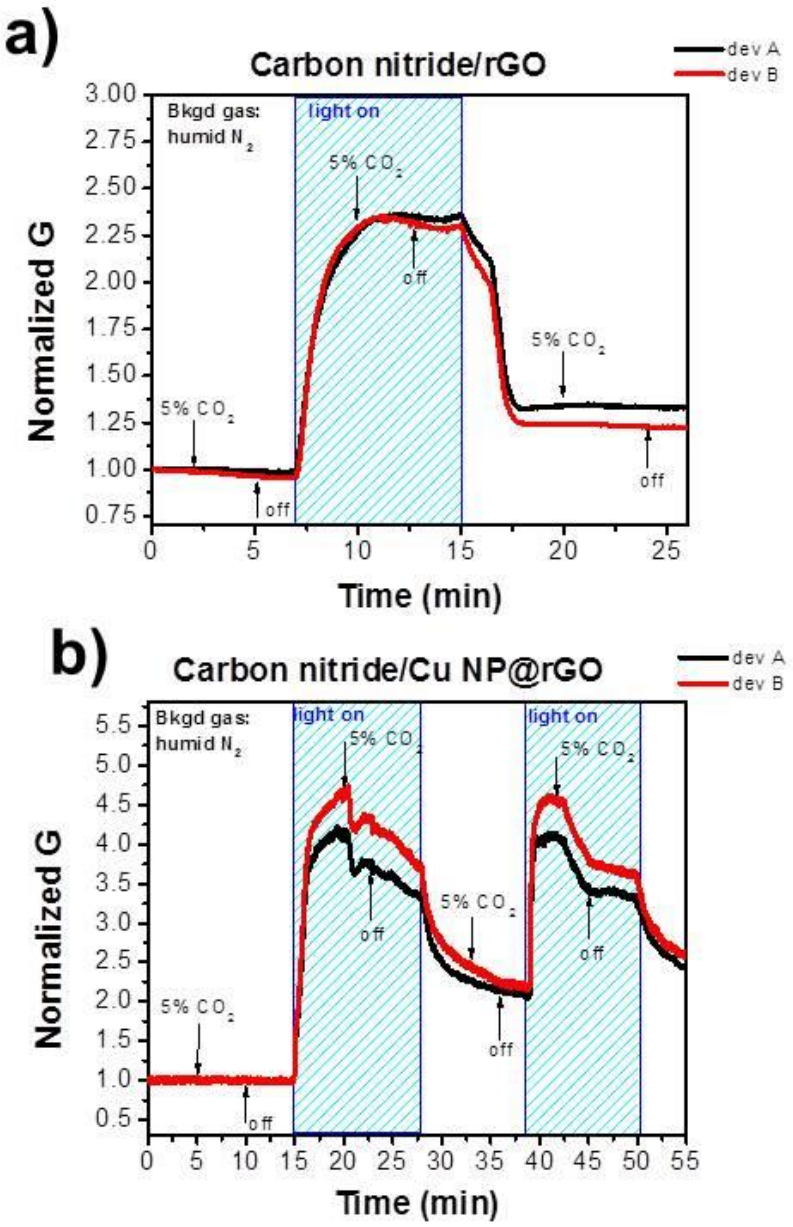

Figure 5.4 CO_2 sensing with carbon nitride/Cu NP@rGO. a) Carbon nitride/rGO chemiresistor and b) carbon nitride/Cu NP@rGO chemiresistor response to 5% CO_2 in humid N2 with and without UV irradiation.

Two carbon nitride/CuNP@rGO devices (A and B) were tested for CO_2 sensitivity using a controlled gas environment sample chamber (Fig. 5.4b). A baseline conductance was established in humid N_2 flow without irradiation. A 5-minute CO_2 exposure in the dark yielded no signal, thus demonstrating that even with Cu NPs, no charge transfer occurs without photogenerated electrons. Irradiation of the carbon nitride/CuNP@rGO device with a 395nm LED light caused a fourfold increase in conductance, which can be attributed to the photogeneration of charge carriers in carbon nitride and subsequent electron transfer to the rGO layer. A 3-minute exposure of 5% (v/v) CO_2 causes an 11% drop in conductance for device A and 12% drop in conductance for device B. During a second 3-minute CO_2 exposure under irradiation, both devices A and B drop in conductance by 16% and 18%, respectively. The device response toward CO_2 of carbon nitride/CuNP@rGO versus the non-response of carbon nitride/rGO toward CO_2 illustrates the necessary function CuNPs play toward CO_2 detection.

However, unlike the reversible O_2 response observed in our previous work, the carbon nitride/CuNP@rGO response to 5% CO_2 was irreversible. In the case of a photoredox mechanism, recovery back to the original photoexcited conductance means that the photoredox product is desorbed and photogenerated charge carriers can be transferred and transduced through the rGO layer once again. An irreversible response indicates that either the target analyte, in this case CO_2, or a photoredox product cannot desorb or be further reduced to a product that can desorb. It is known that carbon monoxide and formate are key intermediates for CO_2 reduction to methane and ethylene on copper electrodes.[191] Schouten *et al.* have shown that CO_2 reduction to methane is highly pH-dependent and Cu facet- dependent, such that further reduction of chemisorbed CO to CH_4 requires fine-tuning of the catalyst system.[192] The carbon nitride/CuNP@rGO chemiresistor response is consistent with CO_2 reduction occurring, but the

irreversibility of the sensor response suggests further desorption or reduction of CO_2 or the reduced species cannot occur on the surface of CuNP@rGO.

5.4.4 Photoredox Mechanism of Carbon Nitride/CuNP@rGO vdWH

The band structures of carbon nitride and CuNP@rGO were plotted alongside CO_2, H^+, and O_2 reduction potentials to better illustrate the photoredox sensing mechanism of the carbon nitride/CuNP@rGO heterostructure (Fig. 5.5). Light irradiation that exceeds carbon nitride's bandgap (2.7 eV) will create photoexcited electron-hole pairs and raise carbon nitride's Fermi level. Rather than recombining with holes, some photoexcited electrons will transfer from carbon nitride's conduction band to the CuNP@rGO layer. This charge transfer to the CuNP@rGO layer is reflected by the large photocurrent generated whenever UV light is irradiated. Photoexcited electrons on the CuNP@rGO layer can be delocalized across the d-orbitals of the CuNPs, which promotes CO_2 adsorption and subsequent reduction on the CuNP surface. CO_2 reduction removes charge carriers from the CuNP@rGO layer, while CO_2 or CO chemisorption would result in charge pinning; both of these events will cause a decrease in the chemiresistor's conductance.

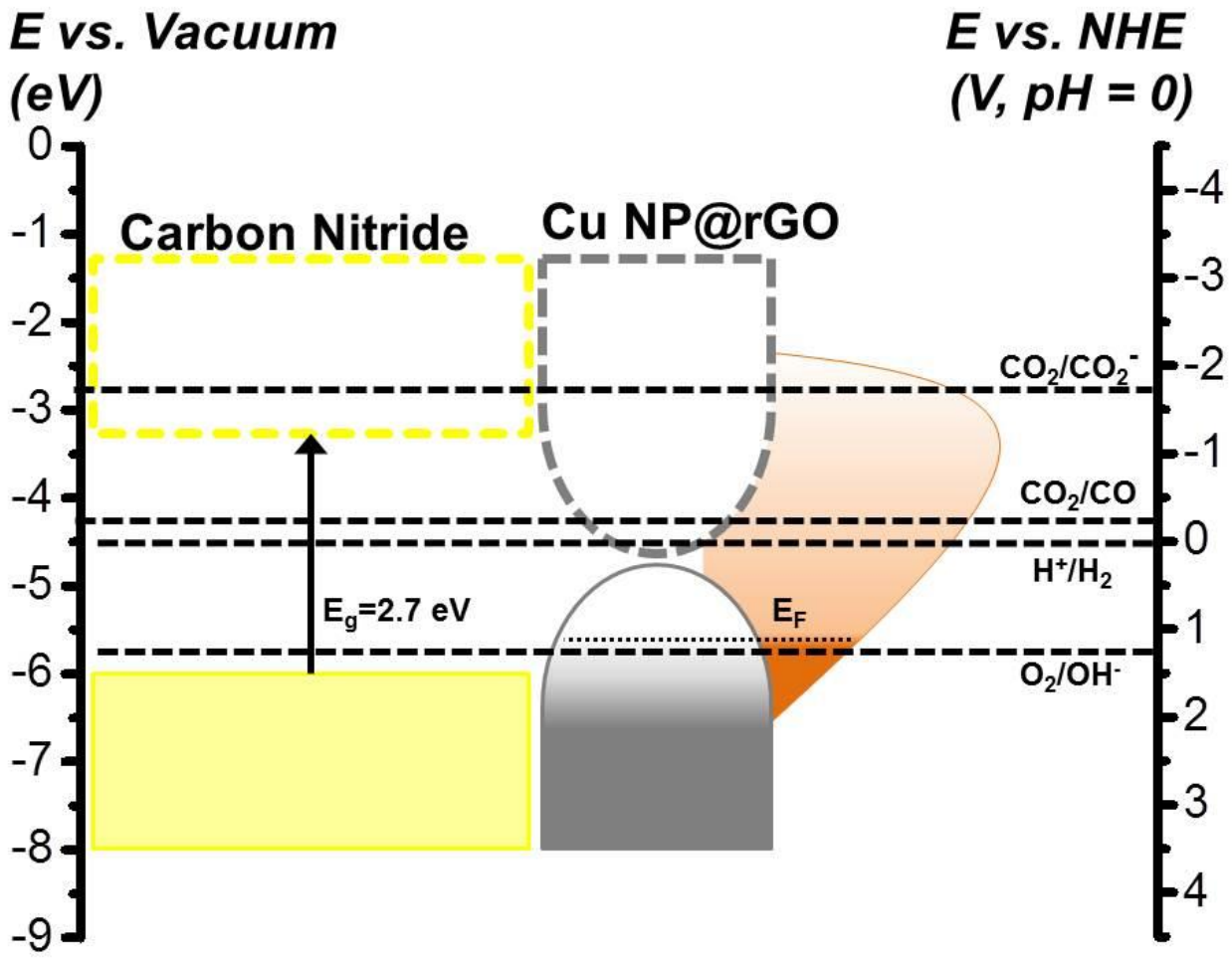

Figure 5.5 Schematic illustration of carbon nitride/Cu NP@rGO vdWH band structure.

5.5 CONCLUSION

In conclusion, this work has characterized the effect of adding CuNPs to a semiconductor/semimetal vdWH, namely carbon nitride/rGO. A +0.9 eV shift in work function and an appearance of a large d-band peak were observed with UPS and valence XPS, respectively, for CuNP@rGO, in contrast to bare rGO. When incorporated into a chemiresistor device, the carbon nitride/CuNP@rGO vdWH showed large photocurrents and sensitivity toward carbon dioxide; carbon dioxide sensitivity was not observed with carbon nitride/bare rGO vdWH. The addition of metal NPs, as well as other dopants, to vdWHs provides a method for tuning the electronic structure of these composite materials, which may in turn provide newfound sensitivities when the composite nanomaterial is incorporated into a sensor device. This work demonstrates the possibilities of electronically tunable vdWHs as a new class of photoelectrochemical sensors.

6.0 SUMMARY AND FUTURE OUTLOOK

The research described in this dissertation sought to synthesize new inorganic—CNM composites that could be applied toward chemical sensing. The common strategy employed throughout this dissertation, with the exception of chapter 4, was the use of defective CNMs, either oxidized SWCNTs or rGO, as the growth substrate for inorganic nanomaterials. In chapter 4, carbon nitride was separately synthesized and stacked on rGO through van der Waals forces and π-stacking interaction. Growth from oxidized defect sites was the synthetic mechanism for In_2O_3/SWCNT composite and CuNP@rGO composite (chapters 2 and 5, respectively); however, the extended π-system of CNM was the basis for inorganic compositing for ZIF-8/SWCNT and carbon nitride/rGO (chapters 3 and 4, respectively). Section 1.4.1 discussed noncovalent attachment of inorganic receptors to CNMs using aromatic linker molecules such as pyrene. Rather than using an aromatic linker molecule, imidazole (chapter 3) and carbon nitride (chapter 4 and 5) themselves are aromatic, which allows for close contact between the CNM and the inorganic layer.

The proposed growth mechanism of ZIF-8 on SWCNTs detailed in chapter 3 is based on the molecular ordering of 2-methylimidazole into a solvation layer around individual SWCNTs. This noncovalent interaction between the imidazole molecules and SWCNT substrate should allow this synthesis to be adapted to other zeolitic imidazolate frameworks. In a broader outlook, MOFs that are composed of water-soluble aromatic organic linkers may also be composited with

SWCNTs using a similar approach. The porosity and high gas intake of these composites make them interesting candidates for chemical sensing or as a component for mixed matrix membranes for gas separation and capture-and-release applications. Each MOF has its own well-defined aperture diameter that restricts gas transport based on the kinetic diameter of the gas molecule.

CNMs have been used as membrane substrates, heterogeneous catalyst substrates, and sensing transducers because of their electrical conductivity, relative high chemical and thermal stability, and nanoscale dimensions; the ability to grow homogenous receptor layers of MOF on these materials will open up new application avenues that were previously unreachable. For example, the well-defined pore aperture and cavity volume of MOFs can provide molecule-specific adsorption, which is rare for electrically conductive materials. Additionally, the electrical properties of a MOF/CNM composite may serve as a probe for gas intake, as well as a potential trigger to release gas from the MOF pores through Joule heating. Another application that MOF/CNM composites may find is as a thermoelectric material; the thermoelectric figure of merit is proportional to electrical conductivity and inversely proportional to thermal conductivity. Most MOF materials are electrically and thermally insulating, while CNMs are electrically and thermally conductive. Through careful compositing of these two materials, a hybrid material with a high thermoelectric figure of merit may be achieved.

The strong adhesion between carbon nitride and rGO created by π-stacking makes the carbon nitride/rGO vdWH unique among the graphene-based 2-D vdWHs. Large charge carrier separation between the two layers was demonstrated in chapters 4 and 5, which was utilized for chemical sensing in a photoredox mechanism. For MOS and most CNM-based sensors, humidity is a confounding effect and obscures the sensing response (e.g., chapter 2); in contrast, the photoredox mechanism of carbon nitride/rGO requires a certain level of humidity to function.

The modulation of the carbon nitride/rGO vdWH electronic structure with copper nanoparticles was analyzed with UPS in chapter 5. Such electronic structure modulation exhibits the wide range of possible modifications that can be performed on the carbon nitride/rGO motif.

CNMs such as SWCNTs and rGO possess many exceptional attributes for chemical sensing such as high surface area to volume ratio, high conductivity, and semiconducting electronic structure, all on the nanoscale. However, CNMs on their own lack microporosity and photoexcited charge carriers. Attaching inorganic layers, such as MOFs and semiconductors, to CNMs can endow new properties to the composite material. The combination of MOF microporosity, photoexcited charge carriers from carbon nitride, and the high conductivity and surface area of CNMs may provide a new class of materials that are both highly selective and sensitive chemical sensors.

APPENDIX A

PUBLICATIONS

1. **J. E. Ellis**, Z. Zeng, S. I. Hwang, S. Li, T. Luo, S. C. Burkert, David L. White, N. L. Rosi, J. J. Gassensmith, A. Star* "Growth of ZIF-8 on molecularly ordered 2-methylimidazole/single-walled carbon nanotubes to form highly porous, electrically conductive composites" *Chem. Sci.* **2019**, Advance Article, DOI: 10.1039/C8SC03987A
2. **J. E. Ellis**, D. C. Sorescu, S. C. Burkert, D. L. White, A. Star* "Uncondensed Graphitic Carbon Nitride on Reduced Graphene Oxide for Oxygen Sensing via a Photoredox Mechanism" *ACS Appl. Mater. Interfaces* **2017,** *9*, 27142-27151
3. **J. E. Ellis**, A. Star* "Carbon Nanotube-based Gas Sensors toward Breath Analysis" *ChemPlusChem* **2016,** *81*, 1248-1265
4. G. Peng, S. Wu, **J. E. Ellis**, X. Xu, G. Xu, C. Yu, A. Star* "Single-Walled Carbon Nanotubes Templated CuO Networks for Gas Sensing" *J. Mater. Chem. C* **2016,** *4*, 6575-6580
5. G. Peng, **J. E. Ellis**, G. Xu, X. Xu, A. Star* "In-situ Grown TiO2 Nanospindles Facilitate the Formation of Holey Reduced Graphene Oxide by Photodegradation" *ACS Appl. Mater. Interfaces* **2016**, *8*, 7403-7410

6. G. Peng, J. Wu, X. Xu*, **J. E. Ellis**, G. Xu*, A. Star, D. Gao* "Perovskite Solar Cells Based on Bottom-Fused TiO2 Nanocones" *J. Mater. Chem. A* **2016**, *4*, 1520-1530
7. **J. E. Ellis**, U. Green, D. C. Sorescu, Y. Zhao, and A. Star* "Indium Oxide--Single-Walled Carbon Nanotube Composite for Ethanol Sensing at Room Temperature" *J. Phys. Chem. Lett.* **2015**, *6*, 712-717
8. G. Peng, X. Xu*, F. Mei, G. Xu, J. Wu, D. Gao, **J. E. Ellis**, Y. Zhao, Y. Xing, and A. Star "Substrate Placement Angle-Dependent Growth of Dandelion-like TiO2 Nanorods for Solid-State Semiconductor-Sensitized Solar Cells." *RSC Adv.* **2014**, *4*, 53335-53343
9. Y. Tang, Y. Zhao, S. C. Burkert, M. Ding, **J. E. Ellis**, and A. Star* "Efficient Separation of Nitrogen-Doped Carbon Nanotube Cups." *Carbon* **2014**, *80*, 583-590

APPENDIX B

TABLE OF ABBREVIATIONS

Table 1. Abbreviations

Abbreviation		Abbreviation	
CB	Conduction band	GC	Gas chromatography
CBM	Conduction band minimum	GO	Graphene oxide
CNM	Carbon nanomaterial	g-C_3N_4	"Graphitic" carbon nitride
CNT	Carbon nanotube	HER	Hydrogen evolution reaction
CVD	Chemical vapor deposition	HRTEM	High-resolution transmission electron microscopy
DEP	Dielectrophoresis	LDOS	Localized density of state
DRIFTS	Diffuse reflectance infrared Fourier transform spectroscopy	LED	Light emitting diode
E_B	Bandgap energy	LOD	Limit of detection
FET	Field effect transistor	LOQ	Limit of quantification
FID	Flame ionization detector	MOF	Metal organic framework
FTIR	Fourier transform infrared	MOS	Metal oxide sensor

	spectroscopy		
Abbreviation		Abbreviation	
OP	Octagonal-pentagonal	NP	Nanoparticle
ox-SWCNT	Oxidized single-walled carbon nanotube	SWCNT	Single-walled carbon nanotube
rGO	reduced graphene oxide	MWCNT	Multi-walled carbon nanotube
ORR	Oxygen reduction reaction	I	Current
PID	Photo-ionization detector	G	Conductance
ppm	Parts per million	R	Resistance
PXRD	Powder X-ray diffraction	V	Voltage
QD	Quantum dot	SW	Stone-Wales
TGA	thermal gravimetric analyzer	TEM	transmission electron microscopy
TMD	Transition metal dichalcogenide	TCD	Thermal conductivity detector
UPS	Ultraviolet photoelectron spectroscopy	VB	Valence band
VBM	Valence band minimum	vdWH	van der Waals heterostructure
XPS	X-ray photoelectron spectroscopy	ZIF	Zeolitic-imidazolate framework
Φ	Work function		

BIBLIOGRAPHY

(1) Rabalais, J. W.; Bergmark, T.; Werme, L. O.; Karlsson, L.; Siegbahn, K. The Jahn-Teller Effect in the Electron Spectrum of Methane. *Phys. Scrip.* **1971,** *3*, 13-18.

(2) Seiyama, T.; Kato, A.; Fujishi, K.; Nagatani, M. *Anal. Chem.* **1962,** *34*, 1502.

(3) Gurlo, A., Insights into the Mechanism of Gas Sensor Operation. In *Metal Oxide Nanomaterials for Chemical Sensors*, Carpenter, M. A.; Kolmakov, A.; Mathur, S., Eds. Springer: New York, 2013.

(4) Gu, F.; Zhang, L.; Wang, Z.; Han, D.; Guo, G. Fine-tuning the structure of cubic indium oxide and their ethanol-sensing properties. *Sens. Actuator B* **2014,** *193*, 669-678.

(5) Seetha, M.; Meena, P.; Mangalaraj, D.; Masuda, Y.; Senthil, K. Synthesis of indium oxide cubic crystals by modified hydrothermal route for application in room temperature flexible ethanol sensors. *Mater. Chem. Phys.* **2012,** *133*, 47-54.

(6) Siemons, M.; Leifert, A.; Simon, U. Preparation and Gas Sensing Characteristics of Nanoparticulate p-Type Semiconducting LnFeO3 and LnCrO3 Materials. *Adv. Funct. Mater.* **2007,** *17*, 2189-2197.

(7) Meixner, H.; Lampe, U. Metal oxide sensors. *Sens. Actuator B* **1996,** *33*, 198-202.

(8) Krivetskiy, V.; Rumyantseva, M.; Gaskov, A., Design, Synthesis and Application of Metal Oxide-Based Sensing Elements: A Chemical Principles Approach. In *Metal Oxide Nanomaterials for Chemical Sensors*, Carpenter, M. A.; Kolmakov, A.; Mathur, S., Eds. Springer: New York, 2013.

(9) Franke, M. E.; Koplin, T. J.; Simon, U. Metal and Metal Oxide Nanoparticles in Chemiresistors: Does the Nanoscale Matter? *Small* **2006,** *2*, 36-50.

(10) Kobayashi, T.; Haruta, M.; Tsubota, S.; Sano, H.; Delmon, B. Thin films of supported gold catalysts for CO detection. *Sens. Actuator B* **1990,** *1*, 222-225.

(11) Spivey, J. J. Complete catalytic oxidation of volatile organics. *Ind. Eng. Chem. Res.* **1987,** *26*, 2165-2180.

(12) Krupke, R.; Hennrich, F.; Lohneysen, H.; Kappes, M. M. Separation of metallic from semiconducting single-walled carbon nanotubes. *Science* **2003,** *301*, 344-7.

(13) Novoselov, K. S.; Geim, A. K.; Morozov, S. V.; Jiang, D.; Zhang, Y.; Dubonos, S. V.; Grigorieva, I. V.; Firsov, A. A. Electric field effect in atomically thin carbon films. *Science* **2004,** *306*, 666-9.

(14) Reina, A.; Jia, X.; Ho, J.; Nezich, D.; Son, H.; Bulovic, V.; Dresselhaus, M. S.; Kong, J. Large area, few-layer graphene films on arbitrary substrates by chemical vapor deposition. *Nano Lett.* **2009,** *9*, 30-5.

(15) Kim, K. S.; Zhao, Y.; Jang, H.; Lee, S. Y.; Kim, J. M.; Kim, K. S.; Ahn, J. H.; Kim, P.; Choi, J. Y.; Hong, B. H. Large-scale pattern growth of graphene films for stretchable transparent electrodes. *Nature* **2009,** *457*, 706-10.

(16) Li, X.; Cai, W.; An, J.; Kim, S.; Nah, J.; Yang, D.; Piner, R.; Velamakanni, A.; Jung, I.; Tutuc, E.; Banerjee, S. K.; Colombo, L.; Ruoff, R. S. Large-area synthesis of high-quality and uniform graphene films on copper foils. *Science* **2009,** *324*, 1312-4.

(17) Kovtyukhova, N. I.; Wang, Y.; Berkdemir, A.; Cruz-Silva, R.; Terrones, M.; Crespi, V. H.; Mallouk, T. E. Non-oxidative intercalation and exfoliation of graphite by Bronsted acids. *Nat. Chem.* **2014,** *6*, 957-63.

(18) Park, S.; Ruoff, R. S. Chemical methods for the production of graphenes. *Nat. Nanotechnol.* **2009,** *4*, 217-24.

(19) Geim, A. K.; Novoselov, K. S. The Rise of Graphene. *Nat. Mater.* **2007,** *6*, 183-191.

(20) Du, X.; Skachko, I.; Barker, A.; Andrei, E. Y. Approaching ballistic transport in suspended graphene. *Nat. Nanotechnol.* **2008,** *3*, 491-5.

(21) Charlier, J.-C.; Eklund, P. C.; Zhu, J.; Ferrari, A. C., Electron and Phonon Properties of Graphene: Their Relationship with Carbon Nanotubes. In *Carbon Nanotubes*, Jorio, A.; Dresselhaus, G.; Dresselhaus, M. S., Eds. Springer: Berlin, 2008; pp 673-709.

(22) Oshima, C.; Nagashima, A. Ultra-thin epitaxial films of graphite and hexagonal boron nitride on solid surfaces. *J. Phys.: Condens. Matter* **1997,** *9*, 1-20.

(23) Giovannetti, G.; Khomyakov, P. A.; Brocks, G.; Karpan, V. M.; van den Brink, J.; Kelly, P. J. Doping graphene with metal contacts. *Phys. Rev. Lett.* **2008,** *101*, 026803.

(24) Novoselov, K. S.; Geim, A. K.; Morozov, S. V.; Jiang, D.; Katsnelson, M. I.; Grigorieva, I. V.; Dubonos, S. V.; Firsov, A. A. Two-dimensional gas of massless Dirac fermions in graphene. *Nature* **2005,** *438*, 197-200.

(25) Nakada, K.; Fujita, M.; Dresselhaus, G.; Dresselhaus, M. S. Edge state in graphene ribbons: Nanometer size effect and edge shape dependence. *Physical Review B* **1996,** *54*, 17954-17961.

(26) Barone, V.; Hod, O.; Scuseria, G. E. Electronic structure and stability of semiconducting graphene nanoribbons. *Nano Lett.* **2006,** *6*, 2748-54.

(27) Avouris, P.; Chen, Z.; Perebeinos, V. Carbon-based electronics. *Nat. Nanotechnol.* **2007,** *2*, 605-15.

(28) Dayen, J. F.; Mahmood, A.; Golubev, D. S.; Roch-Jeune, I.; Salles, P.; Dujardin, E. Side-gated transport in focused-ion-beam-fabricated multilayered graphene nanoribbons. *Small* **2008,** *4*, 716-20.

(29) Li, X.; Wang, X.; Zhang, L.; Lee, S.; Dai, H. Chemically derived, ultrasmooth graphene nanoribbon semiconductors. *Science* **2008,** *319*, 1229-32.

(30) Bai, J.; Zhong, X.; Jiang, S.; Huang, Y.; Duan, X. Graphene nanomesh. *Nat. Nanotechnol.* **2010,** *5*, 190-4.

(31) Liang, X.; Jung, Y. S.; Wu, S.; Ismach, A.; Olynick, D. L.; Cabrini, S.; Bokor, J. Formation of bandgap and subbands in graphene nanomeshes with sub-10 nm ribbon width fabricated via nanoimprint lithography. *Nano Lett.* **2010,** *10*, 2454-60.

(32) Moreno, C.; Vilas-Varela, M.; Kretz, B.; Garcia-Lekue, A.; Costache, M. V.; Paradinas, M.; Panighel, M.; Ceballos, G.; Valenzuela, S. O.; Pena, D.; Mugarza, A. Bottom-up synthesis of multifunctional nanoporous graphene. *Science* **2018,** *360*, 199-203.

(33) Velasco-Soto, M. A.; Pérez-García, S. A.; Alvarez-Quintana, J.; Cao, Y.; Nyborg, L.; Licea-Jiménez, L. Selective band gap manipulation of graphene oxide by its reduction with mild reagents. *Carbon* **2015,** *93*, 967-973.

(34) Shen, Y.; Yang, S.; Zhou, P.; Sun, Q.; Wang, P.; Wan, L.; Li, J.; Chen, L.; Wang, X.; Ding, S.; Zhang, D. W. Evolution of the band-gap and optical properties of graphene oxide with controllable reduction level. *Carbon* **2013,** *62*, 157-164.

(35) Sygellou, L.; Paterakis, G.; Galiotis, C.; Tasis, D. Work Function Tuning of Reduced Graphene Oxide Thin Films. *J. Phys. Chem. C* **2015,** *120*, 281-290.

(36) Feng, H.; Cheng, R.; Zhao, X.; Duan, X.; Li, J. A low-temperature method to produce highly reduced graphene oxide. *Nat Commun* **2013,** *4*, 1539.

(37) Saito, R.; Fujita, M.; Dresselhaus, G.; Dresselhaus, M. S. Electronic structure of chiral graphene tubules. *Appl. Phys. Lett.* **1992,** *60*, 2204-2206.

(38) Kim, S. N.; Rusling, J. F.; Papadimitrakopoulos, F. Carbon Nanotubes for Electronic and Electrochemical Detection of Biomolecules. *Adv. Mater.* **2007,** *19*, 3214-3228.

(39) Li, S.; Yu, Z.; Yen, S.-F.; Tang, W. C.; Burke, P. J. Carbon Nanotube Transistor Operation at 2.6 GHz. *Nano Lett.* **2004,** *4*, 753-756.

(40) Snow, E. S.; Campbell, P. M.; Ancona, M. G.; Novak, J. P. High-mobility carbon-nanotube thin-film transistors on a polymeric substrate. *Appl. Phys. Lett.* **2005,** *86*, 033105.

(41) Derycke, V.; Martel, R.; Appenzeller, J.; Avouris, P. Controlling doping and carrier injection in carbon nanotube transistors. *Appl. Phys. Lett.* **2002,** *80*, 2773-2775.

(42) Ando, T. The Electronic Properties of Graphene and Carbon Nanotubes. *NPG Asia Mater.* **2009,** *1*, 17-21.

(43) Shiraishi, M.; Ata, M. Work function of carbon nanotubes. *Carbon* **2001,** *39*, 1913-1917.

(44) Hirsch, A. Functionalization of Single-Walled Carbon Nanotubes. *Angew. Chem. Int. Ed.* **2002,** *41*, 1853.

(45) Tasis, D.; Tagmatarchis, N.; Bianco, A.; Prato, M. Chemistry of Carbon Nanotubes. *Chem Rev.* **2006,** *106*, 1105.

(46) Eder, D. Carbon Nanotube-Inorganic Hybrids. *Chem. Rev.* **2010,** *110*, 1348.

(47) Blondeau, P., Enhancing the Surface Sensitivity and Selectivity: Functionalization of Carbon Nanomaterials. In *Carbon for Sensing Devices*, Demarchi, D.; Tagliaferro, A., Eds. Springer International: Switzerland, 2015.

(48) Ding, M.; Tang, Y.; Star, A. Understanding Interfaces in Metal-Graphitic Hybrid Nanostructures. *J. Phys. Chem. Lett.* **2013,** *4*, 147-60.

(49) Datsyuk, V.; Kalyva, M.; Papagelis, K.; Parthenios, J.; Tasis, D.; Siokou, A.; Kallitsis, I.; Galiotis, C. Chemical Oxidation of Multiwalled Carbon Nanotubes. *Carbon* **2008,** *46*, 833.

(50) Zhang, J.; Zou, H.; Qing, Q.; Yang, Y.; Li, Q.; Liu, Z.; Guo, X.; Du, Z. Effect of Chemical Oxidation on the Structure of Single-Walled Carbon Nanotubes. *J. Phys. Chem. B* **2003,** *107*, 3712.

(51) Kim, J. H.; Song, M.-J.; Lee, C. J.; Lee, J.-H.; Kim, J.-H.; Min, M. K. A Comparative Study of Electrochemical and Biointerfacial Properties of Acid- and Plasma-Treated Single-Walled Carbon-Nanotube-Film Electrode Systems for Use in Biosensors. *Carbon* **2013,** *52*, 398.

(52) Rubio, N.; Fabbro, C.; Herrero, M. A.; Hoz, A. d. l.; Meneghetti, M.; Fierro, J. L. G.; Prato, M.; Vázquez, E. Ball-Milling Modification of Single-Walled Carbon Nanotubes: Purification, Cutting, and Functionalization. *Small* **2011,** *7*, 665.

(53) Jeon, I. Y.; Choi, H. J.; Choi, M.; Seo, J. M.; Jung, S. M.; Kim, M. J.; Zhang, S.; Zhang, L.; Xia, Z.; Dai, L.; Park, N.; Baek, J. B. Facile, scalable synthesis of edge-halogenated graphene nanoplatelets as efficient metal-free eletrocatalysts for oxygen reduction reaction. *Sci. Rep.* **2013,** *3*, 1810.

(54) Liang, Y.; Li, Y.; Wang, H.; Dai, H. Strongly Coupled Inorganic/Nanocarbon Hybrid Materials for Advanced Electrocatalysis. *J. Am. Chem. Soc.* **2013,** *135*, 2013.

(55) Wang, H.; Dai, H. Strongly Coupled Inorganic-Nano-Carbon Hybrid Materials for Energy Storage. *Chem. Soc. Rev.* **2013,** *42*, 3088.

(56) Wang, H.; Liang, Y.; Gong, M.; Li, Y.; Chang, W.; Mefford, T.; Zhou, J.; Wang, J.; Regier, T.; Wei, F.; Dai, H. An Ultrafast Nickel-Iron Battery from Strongly Coupled Inorganic Nanoparticle/Nanocarbon Hybrid Materials. *Nat. Commun.* **2012,** *3*, 917.

(57) Liang, Y.; Wang, H.; Diao, P.; Chang, W.; Hong, G.; Li, Y.; Gong, M.; Xie, L.; Zhou, J.; Wang, J.; Regier, T. Z.; Wei, F.; Dai, H. Oxygen Reduction Electrocatalyst Based on Strongly Coupled Cobalt Oxide Nanocrystals and Carbon Nanotubes. *J. Am. Chem. Soc.* **2012,** *134*, 15849.

(58) Bahr, J. L.; Tour, J. M. Covalent Chemistry of Single-Wall Carbon Nanotubes. *J. Mater. Chem.* **2002,** *12*, 1952.

(59) Banerjee, S.; Hamraj-Benny, T.; Wong, S. S. Covalent Surface Chemistry of Single-Walled Carbon Nanotubes. *Adv. Mater.* **2005,** *17*, 17.

(60) Hu, H.; Zhao, B.; Hamon, M. A.; Kamaras, K.; Itkis, M. E.; Haddon, R. C. Sidewall Functionalization of Single-Walled Carbon Nanotubes by Addition of Dichlorocarbene. *J. Am. Chem. Soc.* **2003,** *125*, 14893.

(61) Holzinger, M.; Vostrowsky, O.; Hirsch, A.; Hennrich, F.; Kappes, M.; Weiss, R.; Jellen, F. Sidewall Functionalization of Carbon Nanotubes. *Angew. Chem. Int. Ed.* **2001,** *40*, 4002.

(62) Gao, C.; He, H.; Zhou, L.; Zheng, X.; Zhang, Y. Scalable Functional Group Engineering of Carbon Nanotubes by Improved One-Step Nitrene Chemistry. *Chem. Mater.* **2009,** *21*, 360.

(63) Leinonen, H.; Rintala, J.; Siitonen, A.; Lajunen, M.; Pettersson, M. New Nitrene Functionalizations onto Sidewalls of Carbon Nanotubes and Their Spectroscopic Analysis. *Carbon* **2010,** *48*, 2425.

(64) Georgakilis, V.; Kordatos, K.; Prato, M.; Guldi, D. M.; Holzinger, M.; Hirsch, A. Organic Functionalization of Carbon Nanotubes. *J. Am. Chem. Soc.* **2002,** *124*, 760.

(65) Pastorin, G.; Wu, W.; Wieckowski, S.; Briand, J. P.; Kostarelos, K.; Prato, M. Double Functionalisation of Carbon Nanotubes for Multimodal Drug Delivery. *Chem. Comm.* **2006**, 1182.

(66) Oelsner, C.; Herrero, M. A.; Ehli, C.; Prato, M.; Guldi, D. M. Charge Transfer Events in Semiconducting Single-Wall Carbon Nanotubes. *J. Am. Chem. Soc.* **2011,** *133*, 18696.

(67) Ehli, C.; Rahman, G. M. A.; Jux, N.; Balbinot, D.; Guldi, D. M.; Paolucci, F.; Marcaccio, M.; Paolucci, D.; Melle-Franco, M.; Zerbetto, F.; Campidelli, S.; Prato, M. Interactions in

Single Wall Carbon Nanotubes/Pyrene/Porphyrin Nanohybrids. *J. Am. Chem. Soc.* **2006,** *128*, 11222.

(68) Zhang, S.; Shao, Y.; Yin, G.; Lin, Y. Carbon Nanotubes Decorated with Pt Nanoparticles via Electrostatic Self-Assembly: a Highly Active Oxygen Reduction Electrocatalyst. *J. Mater. Chem* **2010,** *20*, 2826.

(69) Rance, G. A.; Marsh, D. H.; Bourne, S. J.; Reade, T. J.; Khlobystov, A. N. van der Waals Interactions between Nanotubes and Nanoparticles for Controlled Assembly of Composite Nanostructures. *ACS Nano* **2010,** *4*, 4920.

(70) Zhao, Y.-L.; Stoddart, J. F. Noncovalent Functionalization of Single-Walled Carbon Nanotubes. *Acc. Chem. Res.* **2009,** *42*, 1161.

(71) Hu, L.; Zhao, Y.-L.; Ryu, K.; Zhou, C.; Stoddart, J. F.; Gruner, G. Light-Induced Charge Transfer in Pyrene/CdSe-SWNT Hybrids. *Adv. Mater.* **2008,** *20*, 939.

(72) Zhao, Y.-L.; Hu, L.; Stoddart, J. F.; Gruner, G. Pyrenecyclodextrin-Decorated Single-Walled Carbon Nanotube Field-Effect Transistors as Chemical Sensors. *Adv. Mater.* **2008,** *20*, 1910.

(73) Lee, Y.; Song, H. J.; Shin, H. S.; Shin, H. J.; Choi, H. C. Spontaneous Formation of Transition-Metal Nanoparticles on Single-Walled Carbon Nanotubes Anchored with Conjugated Molecules. *Small* **2005,** *1*, 975.

(74) Chen, R. J.; Bangsaruntip, S.; Drouvalakis, K. A.; Kam, N. W. S.; Shim, M.; Li, Y.; Kim, W.; Utz, P. J.; Dai, H. Noncovalent Functionalization of Carbon Nanotubes for Highly Specific Electronic Biosensors. *Proc. Natl. Acad. Sci. U.S.A.* **2003,** *100*, 4984.

(75) Liu, Y.; Weiss, N. O.; Duan, X.; Cheng, H.-C.; Huang, Y.; Duan, X. Van der Waals heterostructures and devices. *Nat. Rev. Mater.* **2016,** *1*.

(76) Zhou, W.; Apkarian, R. P.; Wang, Z. L.; Joy, D., Fundamentals of Scanning Electron Microscopy (SEM). In *Scanning Microscopy for Nanotechnology*, Springer: 2007.

(77) Wang, Z. L. Transmission Electron Microscopy of Shape-Controlled Nanocrystals and Their Assemblies. *J. Phys. Chem. B* **2000,** *104*, 1153-1175.

(78) Dresselhaus, M. S.; Dresselhaus, G.; Saito, R.; Jorio, A. Raman Spectroscopy of Carbon Nanotubes. *Phys. Rep.* **2005,** *409*, 47-99.

(79) Liu, X.; Luo, Z.; Han, S.; Tang, T.; Zhang, D.; Zhou, C. Band engineering of carbon nanotube field-effect transistors via selected area chemical gating. *Appl. Phys. Lett.* **2005,** *86*, 243501.

(80) Bradley, K.; Gabriel, J.-C. P.; Star, A.; Grüner, G. Short-channel effects in contact-passivated nanotube chemical sensors. *Appl. Phys. Lett.* **2003,** *83*, 3821-3823.

(81) Kong, J.; Franklin, N. R.; Zhou, C.; Chapline, M. G.; Peng, S.; Cho, K.; Dai, H. Nanotube Molecular Wires as Chemical Sensors. *Science* **2000,** *287*, 622-625.

(82) Voggu, R.; Rout, C. S.; Franklin, A. D.; Fisher, T. S.; Rao, C. N. R. Extraordinary Sensitivity of the Electronic Structure and Properties of Single-Walled Carbon Nanotubes to Molecular Charge-Transfer. *J.Phys. Chem. C* **2008,** *112*, 13053-13056.

(83) Boyd, A.; Dube, I.; Fedorov, G.; Paranjape, M.; Barbara, P. Gas sensing mechanism of carbon nanotubes: From single tubes to high-density networks. *Carbon* **2014,** *69*, 417-423.

(84) Fennell, J. F., Jr.; Liu, S. F.; Azzarelli, J. M.; Weis, J. G.; Rochat, S.; Mirica, K. A.; Ravnsbaek, J. B.; Swager, T. M. Nanowire Chemical/Biological Sensors: Status and a Roadmap for the Future. *Angew. Chem. Int. Ed.* **2016,** *55*, 1266-81.

(85) Li, C.; Thostenson, E. T.; Chou, T.-W. Dominant role of tunneling resistance in the electrical conductivity of carbon nanotube–based composites. *Appl. Phys. Lett.* **2007,** *91*, 223114.

(86) Wei, C.; Dai, L.; Roy, A.; Tolle, T. B. Multifunctional chemical vapor sensors of aligned carbon nanotube and polymer composites. *J. Am. Chem. Soc.* **2006,** *128*, 1412-3.

(87) Ishihara, S.; O'Kelly, C. J.; Tanaka, T.; Kataura, H.; Labuta, J.; Shingaya, Y.; Nakayama, T.; Ohsawa, T.; Nakanishi, T.; Swager, T. M. Metallic versus Semiconducting SWCNT Chemiresistors: A Case for Separated SWCNTs Wrapped by a Metallosupramolecular Polymer. *ACS Appl. Mater. Interfaces* **2017,** *9*, 38062-38067.

(88) Zhang, M.; Brooks, L. L.; Chartuprayoon, N.; Bosze, W.; Choa, Y. H.; Myung, N. V. Palladium/single-walled carbon nanotube back-to-back Schottky contact-based hydrogen sensors and their sensing mechanism. *ACS Appl. Mater. Interfaces* **2014,** *6*, 319-26.

(89) Kauffman, D. R.; Star, A. Carbon Nanotube Gas and Vapor Sensors. *Angew. Chem. (Int. Ed.)* **2008,** *47*, 6550-6570.

(90) Franke, M. E.; Koplin, T. J.; Simon, U. Metal and Metal Oxide Nanoparticles in Chemiresistors: Does the Nanoscale Matter? *Small* **2006,** *2*, 36-50.

(91) Gopalakrishna, D.; Vijayalakshmi, K.; Ravidhas, C. Effect of Pyrolytic Temperature on the Properties of Nano-Structured CuO Optimized for Ethanol Sensing Applications. *J. Mater. Sci. Mater. Electron.* **2012,** *24*, 1004-1011.

(92) Zhao, C.; Fu, J.; Zhang, Z.; Xie, E. Enhanced Ethanol Sensing Performance of Porous Ultrathin NiO Nanosheets with Neck-Connected Networks. *RSC Adv.* **2013,** *3*, 4018-4023.

(93) Khan, S. B.; Faisal, M.; Rahman, M. M.; Jamal, A. Low-Temperature Growth of ZnO Nanoparticles: Photocatalyst and Acetone Sensor. *Talanta* **2011,** *85*, 943-949.

(94) Durkop, T.; Getty, S. A.; Cobas, E.; Fuhrer, M. S. Extraordinary Mobility in Semiconducting Carbon Nanotubes. *Nano Lett.* **2004,** *4*, 35.

(95) Gu, F.; Zhang, L.; Wang, Z.; Han, D.; Guo, G. Fine-Tuning the Structure of Cubic Indium Oxide and Their Ethanol Sensing Properties. *Sens. Actuator B* **2014,** *193*, 669-678.

(96) Sanze, S.; Gurlo, A.; Hess, C. Monitoring Gas Sensors at Work: Operando Raman-FTIR Study of Ethanol Detection by Indium Oxide. *Angew. Chem. (Int. Ed.)* **2013,** *52*, 3607-3610.

(97) Han, S.-Y.; Herman, G. S.; Chang, C. Low-Temperature, High-Performance, Solution-Processed Indium Oxide Thin-Film Transistors. *J. Am. Chem. Soc.* **2011,** *133*, 5166-5169.

(98) Chen, Y.; Zhu, C.; Wang, T. The Enhanced Ethanol Sensing Properties of Multi-Walled Carbon Nanotubes/SnO_2 Core/Shell Nanostructures. *Nanotechnol.* **2006,** *17*, 3012.

(99) Khanderi, J.; Hoffmann, R. C.; Gurlo, A.; Schneider, J. J. Synthesis and Sensoric Response of ZnO Decorated Carbon Nanotubes. *J. Mater. Chem.* **2009,** *19*, 5039-5046.

(100) Ding, M.; Sorescu, D. C.; Star, A. Photoinduced Charge Transfer and Acetone Sensitivity of Single-Walled Carbon Nanotube-Titanium Dioxide Hybrids. *J. Am. Chem. Soc.* **2013,** *135*, 9015.

(101) Berki, P.; Nemeth, Z.; Reti, B.; Berkesi, O.; Magrez, A.; Aroutiounian, V.; Forro, L.; Hernadi, K. Preparation and Characterization of Multiwalled Carbon Nanotube/In_2O_3 Composites. *Carbon* **2013,** *60*, 266-272.

(102) Chen, P.; Shen, G.; Sukcharoenchoke, S.; Zhou, C. Flexible and Transparent Supercapacitor Based on In_2O_3 Nanowire/Carbon Nanotube Heterogeneous Films. *Appl. Phys. Lett.* **2009,** *94*, 043113.

(103) Kang, D.; Park, N.; Ko, J.; Bae, E.; Park, W. Oxygen-Induced p-Type Doping of a Long Individual Single-Walled Carbon Nanotube. *Nanotechnol.* **2005,** *16*, 1048-1052.

(104) Lee, J.; Park, T.; Lee, J.; Lee, S.; Park, H.; Yi, W. Electric Field Enhancements in In_2O_3-Coated Single-Walled Carbon Nanotubes. *Carbon* **2014,** *76*, 378-385.

(105) Kim, H.-J.; Jeong, H.-M.; Kim, T.-H.; Chung, J.-H.; Kang, Y. C.; Lee, J.-H. Enhanced Ethanol Sensing Characteristics of In_2O_3-Decorated NiO Hollow Nanostructures via Modulation of Hole Accumalation Layers. *ACS Appl. Mater. Interfaces* **2014,** *6*, 18197-18204.

(106) Tao, J.; Batzill, M., Surface Science Studies of Metal Oxide Gas Sensing Materials. In *Metal Oxide Nanomaterials for Chemical Sensors*, Carpenter, M. A.; Mathur, S.; Kolmakov, A., Eds. Springer: New York, 2013.

(107) Mubeen, S.; Lai, M.; Zhang, T.; Lim, J.-H.; Mulchandani, A.; Deshusses, M. A.; Myung, N. V. Hybrid Tin Oxide-SWNT Nanostructures Based Gas Sensor. *Electrochim. Acta* **2013,** *92*, 484-490.

(108) Mendoza, F.; Dionne, D. M.; Makarov, V.; Febus, E.; Weiner, B. R.; Morell, G. Room Temperature Gas Sensor Based on Tin Dioxide-Carbon Nanotubes Composite Films. *Sens. Actuator B* **2014,** *190*, 227-233.

(109) Sato, T. Preparation and Thermal Decomposition of Indium Hydroxide. *J. Therm. Anal. Calorim.* **2005,** *82*, 775-782.

(110) Chen, R.; Yao, J.; Gu, Q.; Smeets, S.; Baerlocher, C.; Gu, H.; Zhu, D.; Morris, W.; Yaghi, O. M.; Wang, H. A two-dimensional zeolitic imidazolate framework with a cushion-shaped cavity for CO2 adsorption. *Chem. Commun.* **2013,** *49*, 9500-2.

(111) Yang, S. J.; Choi, J. Y.; Chae, H. K.; Cho, J. H.; Nahm, K. S.; Park, C. R. Preparation and Enhanced Hydrostability and Hydrogen Storage Capacity of CNT@MOF-5 Hybrid Composite. *Chem. Mater.* **2009,** *21*, 1893-1897.

(112) Xiang, Z.; Peng, X.; Cheng, X.; Li, X.; Cao, D. CNT@Cu3(BTC)2 and Metal–Organic Frameworks for Separation of CO2/CH4 Mixture. *J. Phys. Chem. C* **2011,** *115*, 19864-19871.

(113) Yoo, J.; Lee, S.; Lee, C. K.; Kim, C.; Fujigaya, T.; Park, H. J.; Nakashima, N.; Shim, J. K. Homogeneous decoration of zeolitic imidazolate framework-8 (ZIF-8) with core–shell structures on carbon nanotubes. *RSC Adv.* **2014,** *4*, 49614-49619.

(114) Sohrabi, S.; Dehghanpour, S.; Ghalkhani, M. A cobalt porphyrin-based metal organic framework/multi-walled carbon nanotube composite electrocatalyst for oxygen reduction and evolution reactions. *J. Mater. Sci.* **2017,** *53*, 3624-3639.

(115) Wang, Q.; Wang, Q.; Xu, B.; Gao, F.; Gao, F.; Zhao, C. Flower-shaped multiwalled carbon nanotubes@nickel-trimesic acid MOF composite as a high-performance cathode material for energy storage. *Electrochim. Acta* **2018,** *281*, 69-77.

(116) Zhang, H.; Zhao, W.; Zou, M.; Wang, Y.; Chen, Y.; Xu, L.; Wu, H.; Cao, A. 3D, Mutually Embedded MOF@Carbon Nanotube Hybrid Networks for High-Performance Lithium-Sulfur Batteries. *Adv. Energy Mater.* **2018**, 1800013.

(117) Pu, Y.; Wu, W.; Liu, J.; Liu, T.; Ding, F.; Zhang, J.; Tang, Z. A defective MOF architecture threaded by interlaced carbon nanotubes for high-cycling lithium–sulfur batteries. *RSC Adv.* **2018,** *8*, 18604-18612.

(118) Ge, L.; Yang, Y.; Wang, L.; Zhou, W.; De Marco, R.; Chen, Z.; Zou, J.; Zhu, Z. High activity electrocatalysts from metal–organic framework-carbon nanotube templates for the oxygen reduction reaction. *Carbon* **2015,** *82*, 417-424.

(119) Pan, Y.; Sun, K.; Liu, S.; Cao, X.; Wu, K.; Cheong, W. C.; Chen, Z.; Wang, Y.; Li, Y.; Liu, Y.; Wang, D.; Peng, Q.; Chen, C.; Li, Y. Core-Shell ZIF-8@ZIF-67-Derived CoP Nanoparticle-Embedded N-Doped Carbon Nanotube Hollow Polyhedron for Efficient Overall Water Splitting. *J. Am. Chem. Soc.* **2018,** *140*, 2610-2618.

(120) Zhang, H.; Wang, Y.; Zhao, W.; Zou, M.; Chen, Y.; Yang, L.; Xu, L.; Wu, H.; Cao, A. MOF-Derived ZnO Nanoparticles Covered by N-Doped Carbon Layers and Hybridized on Carbon Nanotubes for Lithium-Ion Battery Anodes. *ACS Appl. Mater. Interfaces* **2017,** *9*, 37813-37822.

(121) Ghiamaty, Z.; Ghaffarinejad, A.; Faryadras, M.; Abdolmaleki, A.; Kazemi, H. Synthesis of palladium–carbon nanotube–metal organic framework composite and its application as electrocatalyst for hydrogen production. *J. Nanostructure Chem.* **2016,** *6*, 299-308.

(122) Li, S.; Dharmarwardana, M.; Welch, R. P.; Benjamin, C. E.; Shamir, A. M.; Nielsen, S. O.; Gassensmith, J. J. Investigation of Controlled Growth of Metal-Organic Frameworks on Anisotropic Virus Particles. *ACS Appl. Mater. Interfaces* **2018,** *10*, 18161-18169.

(123) Shim, Y.; Kim, H. J. Solvation of carbon nanotubes in a room-temperature ionic liquid. *ACS Nano* **2009,** *3*, 1693-702.

(124) Fukushima, T.; Kosaka, A.; Ishimura, Y.; Yamamoto, T.; Takigawa, T.; Ishii, N.; Aida, T. Molecular ordering of organic molten salts triggered by single-walled carbon nanotubes. *Science* **2003,** *300*, 2072-4.

(125) Venkateswaran, U. D.; Rao, A. M.; Richter, E.; Menon, M.; Rinzler, A.; Smalley, R. E.; Eklund, P. C. Probing the single-wall carbon nanotube bundle: Raman scattering under high pressure. *Phys. Rev. B* **1999,** *59*, 10928-10934.

(126) Cronin, S. B.; Swan, A. K.; Ünlü, M. S.; Goldberg, B. B.; Dresselhaus, M. S.; Tinkham, M. Resonant Raman spectroscopy of individual metallic and semiconducting single-wall carbon nanotubes under uniaxial strain. *Phys. Rev. B* **2005,** *72*.

(127) Filho, A. G. S.; Jorio, A.; Samsonidze, G. G.; Dresselhaus, G.; Saito, R.; Dresselhaus, M. S. Raman spectroscopy for probing chemically/physically induced phenomena in carbon nanotubes. *Nanotechnol.* **2003,** *14*, 1130-1139.

(128) Jian, M.; Liu, B.; Liu, R.; Qu, J.; Wang, H.; Zhang, X. Water-based synthesis of zeolitic imidazolate framework-8 with high morphology level at room temperature. *RSC Adv.* **2015,** *5*, 48433-48441.

(129) Lo, Y.; Lam, C. H.; Chang, C.-W.; Yang, A.-C.; Kang, D.-Y. Polymorphism/pseudopolymorphism of metal–organic frameworks composed of zinc(ii) and 2-methylimidazole: synthesis, stability, and application in gas storage. *RSC Adv.* **2016,** *6*, 89148-89156.

(130) Chen, B.; Bai, F.; Zhu, Y.; Xia, Y. Hofmeister anion effect on the formation of ZIF-8 with tuneable morphologies and textural properties from stoichiometric precursors in aqueous ammonia solution. *RSC Adv.* **2014,** *4*, 47421-47428.

(131) Lee, W. C.; Chien, H. T.; Lo, Y.; Chiu, H. C.; Wang, T. P.; Kang, D. Y. Synthesis of Zeolitic Imidazolate Framework Core-Shell Nanosheets Using Zinc-Imidazole Pseudopolymorphs. *ACS Appl. Mater. Interfaces* **2015,** *7*, 18353-61.

(132) Hinterholzinger, F. M.; Ranft, A.; Feckl, J. M.; Rühle, B.; Bein, T.; Lotsch, B. V. One-dimensional metal–organic framework photonic crystals used as platforms for vapor sorption. *J. Mater. Chem.* **2012,** *22*, 10356.

(133) Muller, G.; Krotz, G.; Schalk, J. New Sensors for Automotive and Aerospace Applications. *Phys. Stat. Sol. (a)* **2001,** *185*, 1-14.

(134) Docquier, N.; Candel, S. Combustion Control and Sensors: A Review. *Prog. Energy Combustion Sci.* **2002,** *28*, 107-150.

(135) Ikeda, E. Cellular Response to Tissue Hypoxia and Its Involvment in Disease Progression. *Pathol. Int.* **2005,** *55*, 603-610.

(136) Harris, A. L. Hypoxia-a Key Regulatory Factor in Tumour Growth. *Nat. Rev. Cancer* **2002,** *2*, 38-47.

(137) Wu, C.; Bull, B.; Christensen, K.; McNeill, J. Ratiometric Single-Nanoparticle Oxygen Sensors for Biological Imaging. *Angew. Chem. Int. Ed.* **2009,** *48*, 2741-2745.

(138) Kauffman, D. R.; Shade, C. M.; Uh, H.; Petoud, S.; Star, A. Decorated Carbon Nanotubes with Unique Oxygen Sensitivity. *Nat. Chem.* **2009,** *1*, 500-506.

(139) Wang, T.; Huang, D.; Yang, Z.; Xu, S.; He, G.; Li, X.; Hu, N.; Yin, G.; He, D.; Zhang, L. A Review on Graphene-Based Gas/Vapor Sensors with Unique Properties and Potential Application. *Nano-Micro Lett.* **2016,** *8*, 95-119.

(140) Ellis, J. E.; Star, A. Carbon Nanotube Based Gas Sensors Toward Breath Analysis. *ChemPlusChem* **2016,** *81*, 1248-1265.

(141) Yuan, W.; Shi, G. Graphene-Based Gas Sensors. *J. Mater. Chem. A* **2013,** *1*, 10078-10091.

(142) Meyyappan, M. Carbon Nanotube-Based Chemical Sensors. *Small* **2016,** *12*, 2118-2129.

(143) Ding, M.; Tang, Y.; Star, A. Understanding Interfaces in Metal-Graphitic Hybrid Nanostructures. *J. Phys. Chem. Lett.* **2013,** *4*, 147-160.

(144) Kudo, A.; Miseki, Y. Heterogeneous Photocatalyst Materials for Water Splitting. *Chem. Soc. Rev.* **2009,** *38*, 253-278.

(145) Qu, Y.; Duan, X. Progress, Challenge and Perspective of Heterogeneous Photocatalysts. *Chem. Soc. Rev.* **2013,** *42*, 2568-2580.

(146) Thomas, A.; Fischer, A.; Goettmann, F.; Antonietti, M.; Muller, J.-O.; Schlogl, R.; Carlsson, J. M. Graphitic Carbon Nitride Materials: Variation of Structure and Morphology and Their Use as Metal-Free Catalysts. *J. Mater. Chem.* **2008,** *18*, 4893-4908.

(147) Wang, Y.; Wang, X.; Antonietti, M. Polymeric Graphitic Carbon Nitride as a Heterogeneous Organocatalyst: From Photochemistry to Multipurpose Catalysis to Sustainable Chemistry. *Angew. Chem. Int. Ed.* **2012,** *51*, 68-89.

(148) Zheng, Y.; Lin, L.; Wang, B.; Wang, X. Graphitic Carbon Nitride Polymers toward Sustainable Photoredox Catalysis. *Angew. Chem. Int. Ed.* **2015,** *54*, 12868-12884.

(149) Wang, X.; Maeda, K.; Thomas, A.; Takanabe, K.; Xin, G.; Carlsson, J. M.; Domen, K.; Antonietti, M. A Metal-Free Polymeric Photocatalyst for Hydrogen Production from Water Under Visible Light. *Nat. Mater.* **2009,** *8*, 76-80.

(150) Niu, P.; Zhang, L.; Liu, G.; Cheng, H.-M. Graphene-Like Carbon Nitride Nanosheets for Improved Photocatalytic Activities. *Adv. Funct. Mater.* **2012,** *22*, 4763-4770.

(151) Cui, Y.; Ding, Z.; Liu, P.; Antonietti, M.; Fu, X.; Wang, X. Metal-Free Activation of H_2O_2 by g-C_3N_4 Under Visible Light Irradiation for the Degradation of Organic Pollutants. *Phys. Chem. Chem. Phys.* **2012,** *14*, 1455-1462.

(152) Yang, S.; Feng, X.; Wang, X.; Mullen, K. Graphene-Based Carbon Nitride Nanosheets as Efficient Metal-Free Electrocatalysts for Oxygen Reduction Reactions. *Angew. Chem. Int. Ed.* **2011,** *50*, 5339-5343.

(153) Zheng, Y.; Jiao, Y.; Chen, J.; Liu, J.; Liang, J.; Du, A.; Zhang, W.; Zhu, Z.; Smith, S. C.; Jaroniec, M.; Lu, G. Q.; Qiao, S. Z. Nanoporous Graphitic-C_3N_4@Carbon Metal-Free Electrocatalysts for Highly Efficient Oxygen Reduction. *J. Am. Chem. Soc.* **2011,** *133*, 20116-20119.

(154) Kofuji, Y.; Ohkita, S.; Shiraishi, Y.; Sakamoto, H.; Tanaka, S.; Ichikawa, S.; Hirai, T. Graphitic Carbon Nitride Doped with Biphenyl Diimide: Efficient Photocatalysts for Hydrogen Peroxide Production from Water and Molecular Oxygen by Sunlight. *ACS Catal.* **2016,** *6*, 7201-7029.

(155) Niu, P.; Yang, Y.; Yu, J. C.; Liu, G.; Cheng, H.-M. Switching the Selectivity of the Photoreduction Reaction of Carbon Dioxide by Controlling the Band Structure of a g-C_3N_4 Photocatalyst. *Chem. Commun.* **2014,** *50*, 10837-10840.

(156) Gao, G.; Jiao, Y.; Waclawik, E. R.; Du, A. Single Atom (Pd/Pt) Supported on Graphitic Carbon Nitride as an Efficient Photocatalyst for Visible-Light Reduction of Carbon Dioxide. *J. Am. Chem. Soc.* **2016,** *138*, 6292-6297.

(157) Gracia, J.; Kroll, P. Corrugated Layered Heptazine-Based Carbon Nitride: the Lowest Energy Modifications of C_3N_4 Ground State. *J. Mater. Chem.* **2009,** *19*, 3013-3019.

(158) Algara-Siller, G.; Severin, N.; Chong, S. Y.; Bjorkman, T.; Palgrave, R. G.; Laybourn, A.; Antonietti, M.; Khimyak, Y. Z.; Krasheninnikov, A. V.; Rabe, J. P.; Kaiser, U.; Cooper, A. I.; Thomas, A.; Bojdys, M. J. Triazine-Based Graphitic Carbon Nitride: a Two-Dimensional Semiconductor. *Angew. Chem. Int. Ed.* **2014,** *53*, 7450-7455.

(159) Park, S.; An, J.; Potts, J. R.; Velamakanni, A.; Murali, S.; Ruoff, R. S. Hydrazine-Redution of Graphite- and Graphene Oxide. *Carbon* **2011,** *49*, 3019-3023.

(160) Lotsch, B. V.; Doblinger, M.; Sehnert, J.; Seyfarth, L.; Senker, J.; Oeckler, O.; Schnick, W. Unmasking Melon by a Complementary Aproach Employing Electron Diffraction, Solid-State NMR Spectroscopy, and Theoretical Calculations-Structural Characterization of a Carbon Nitride Polymer. *Chem. Eur. J.* **2007,** *13*, 4969-4980.

(161) Wirnhier, E.; Doblinger, M.; Gunzelmann, D.; Senker, J.; Lotsch, B. V.; Schnick, W. Poly(triazine imide) with Intercalation of Lithium and Chloride Ions $[(C_3N_3)_2(NH_xLi_{1-x})_3$-LiCl]: A Crystalline 2D Carbon Nitride Network. *Chem. Eur. J.* **2011,** *17*, 3213-3221.

(162) Zuluaga, S.; Liu, L.-H.; Shafig, N.; Rupich, S. M.; Veyan, J.-F.; Chabal, Y. J.; Thonhauser, T. Structural Band-Gap Tuning in g-C_3N_4. *Phys. Chem. Chem. Phys.* **2015,** *17*, 957-962.

(163) Niu, P.; Yin, L.-C.; Yang, Y.-Q.; Liu, G.; Cheng, H.-M. Increasing the Visible Light Absorption of Graphitic Carbon Nitride (Melon) Photocatalysts by Homogenous Self-Modification with Nitrogen Vacancies. *Adv. Mater.* **2014,** *26*, 8046-8052.

(164) Jansen, R. J. J.; Bekkum, H. v. XPS of Nitrogen-Containing Functional Groups on Activated Carbon. *Carbon* **1995,** *33*, 1021-1207.

(165) Pels, J. R.; Kapteijn, F.; Moulijn, J. A.; Zhu, Q.; Thomas, K. M. Evolution of Nitrogen Functionalities in Carbonaceous Materials during Pyrolysis. *Carbon* **1995,** *33*, 1641-1653.

(166) Wojtowicz, M. A.; Pels, J. R.; Moulijn, J. A. The Fate of Nitrogen Functionalities in Coal during Pyrolysis and Combustion. *Fuel* **1995,** *74*, 507-516.

(167) Yang, S.; Gong, Y.; Zhang, J.; Zhan, L.; Ma, L.; Fang, Z.; Vajtai, R.; Wang, X.; Ajayan, P. M. Exfoliated Graphitic Carbon Nitride Nanosheets as Efficient Catalysts for Hydrogen Evolution Under Visible Light. *Adv. Mater.* **2013,** *25*, 2452-2456.

(168) Ong, W.-J.; Putri, L. K.; Tan, Y.-C.; Tan, L.-L.; Li, N.; Ng, Y. H.; Wen, X.; Chai, S.-P. Unravelling Charge Carrier Dynamics in Protonated g-C_3N_4 Interfaced with Carbon Nanodots as Co-Catalysts toward Enhanced Photocatalytic CO_2 Reduction: A Combined Experimental and First-Principles DFT Study. *Nano Res.* **2017,** *10*, 1673-1696.

(169) Gomez-Navarro, C.; Meyer, J. C.; Sundaram, R. S.; Chuvilin, A.; Kurasch, S.; Burghard, M.; Kern, K.; Kaiser, U. Atomic Structure of Reduced Graphene Oxide. *Nano Lett.* **2010,** *10*, 1144-1148.

(170) Yu, S. U.; Park, B.; Cho, Y.; Hyun, S.; Kim, J. K.; Kim, K. S. Simultaneous Visualization of Graphene Grain Boundaries and Wrinkles with Structural Information by Gold Deposition. *ACS Nano* **2014,** *8*, 8662-8668.

(171) Ong, W.-J.; Tan, L.-L.; Chai, S.-P.; Yong, S.-T.; Mohamed, A. R. Surface Charge Modification via Protonation of Graphitic Carbon Nitride (g-C_3N_4) for Electrostatic Self-Assembly Construction of 2D/2D Reduced Graphene Oxide (rGO)/g-C_3N_4 Nanostructures toward Enhanced Photocatalytic Reduction of Carbon Dioxide to Methane. *Nano Energy* **2015,** *13*, 757-770.

(172) Chen, G.; Paronyan, T. M.; Harutyunyan, A. R. Sub-ppt Gas Detection with Pristine Graphene. *Appl. Phys. Lett.* **2012,** *101*, 053119.

(173) Lu, X.; Xu, K.; Chen, P.; Jia, K.; Liu, S.; Wu, C. Facile One Step Method Realizing Scalable Production of g-C_3N_4 Nanosheets and Study of Their Photocatalytic H_2 Evolution Activity. *J. Mater. Chem. A* **2014,** *2*, 18924-18928.

(174) Kofuji, Y.; Isobe, Y.; Shiraishi, Y.; Sakamoto, H.; Tanaka, S.; Ichikawa, S.; Hirai, T. Carbon Nitride-Aromatic Diimide-Graphene Nanohybrids: Metal-Free Photocatalysts for Solar-to-Hydrogen Peroxide Energy Conversion with 0.2% Efficiency. *J. Am. Chem. Soc.* **2016,** *138*, 10019-10025.

(175) Niu, P.; Yang, Y.; Yu, J. C.; Liu, G.; Cheng, H. M. Switching the selectivity of the photoreduction reaction of carbon dioxide by controlling the band structure of a g-C3N4 photocatalyst. *Chem. Commun.* **2014,** *50*, 10837-10840.

(176) Zheng, Y.; Jiao, Y.; Zhu, Y.; Li, L. H.; Han, Y.; Chen, Y.; Du, A.; Jaroniec, M.; Qiao, S. Z. Hydrogen evolution by a metal-free electrocatalyst. *Nat. Commun.* **2014,** *5*, 3783.

(177) Xiang, Q.; Yu, J.; Jaroniec, M. Preparation and Enhanced Visible-Light Photocatalytic H2-Production Activity of Graphene/C3N4 Composites. *J. Phys. Chem. C* **2011,** *115*, 7355-7363.

(178) Duan, J.; Chen, S.; Jaroniec, M.; Qiao, S. Z. Porous C3N4 nanolayers@N-graphene films as catalyst electrodes for highly efficient hydrogen evolution. *ACS Nano* **2015,** *9*, 931-40.

(179) Kofuji, Y.; Isobe, Y.; Shiraishi, Y.; Sakamoto, H.; Tanaka, S.; Ichikawa, S.; Hirai, T. Carbon Nitride-Aromatic Diimide-Graphene Nanohybrids: Metal-Free Photocatalysts for Solar-to-Hydrogen Peroxide Energy Conversion with 0.2% Efficiency. *J. Am. Chem. Soc.* **2016,** *138*, 10019-25.

(180) Ellis, J. E.; Sorescu, D. C.; Burkert, S. C.; White, D. L.; Star, A. Uncondensed Graphitic Carbon Nitride on Reduced Graphene Oxide for Oxygen Sensing via a Photoredox Mechanism. *ACS Appl. Mater. Interfaces* **2017,** *9*, 27142-27151.

(181) Prim, A.; Pellicer, E.; Rossinyol, E.; Peiró, F.; Cornet, A.; Morante, J. R. A Novel Mesoporous CaO-Loaded In2O3 Material for CO2 Sensing. *Adv. Funct. Mater.* **2007,** *17*, 2957-2963.

(182) Djerdj, I.; Haensch, A.; Koziej, D.; Pokhrel, S.; Barsan, N.; Weimar, U.; Niederberger, M. Neodymium Dioxide Carbonate as a Sensing Layer for Chemoresistive CO2Sensing. *Chem. Mater.* **2009,** *21*, 5375-5381.

(183) Vedala, H.; Sorescu, D. C.; Kotchey, G. P.; Star, A. Chemical sensitivity of graphene edges decorated with metal nanoparticles. *Nano Lett.* **2011,** *11*, 2342-7.

(184) Alfano, B.; Polichetti, T.; Mauriello, M.; Miglietta, M. L.; Ricciardella, F.; Massera, E.; Di Francia, G. Modulating the sensing properties of graphene through an eco-friendly metal-decoration process. *Sens. Actuators B* **2016,** *222*, 1032-1042.

(185) Hori, Y.; Takahashi, R.; Yoshinami, Y.; Murata, A. Electrochemical Reduction of CO at a Copper Electrode. *J. Phys. Chem. B* **1997,** *101*, 7075-7081.

(186) Gattrell, M.; Gupta, N.; Co, A. A review of the aqueous electrochemical reduction of CO2 to hydrocarbons at copper. *J. Electroanal. Chem.* **2006,** *594*, 1-19.

(187) Shown, I.; Hsu, H. C.; Chang, Y. C.; Lin, C. H.; Roy, P. K.; Ganguly, A.; Wang, C. H.; Chang, J. K.; Wu, C. I.; Chen, L. C.; Chen, K. H. Highly efficient visible light photocatalytic reduction of CO2 to hydrocarbon fuels by Cu-nanoparticle decorated graphene oxide. *Nano Lett.* **2014,** *14*, 6097-103.

(188) Rasko, J.; Solymosi, F. Infrared Spectroscopic Study of the Photoinduced Activation of CO2 on TiO2 and Rh/TiO2 Catalysts. *J. Phys. Chem.* **1994,** *98*, 7147-7152.

(189) Alves, D. C. B.; Silva, R.; Voiry, D.; Asefa, T.; Chhowalla, M. Copper nanoparticles stabilized by reduced graphene oxide for CO2 reduction reaction. *Mater. Renew. Sustain. Energy* **2015,** *4*.

(190) Fadley, C. S.; Shirley, D. A. Electronic densities of states from x-ray photoelectron spectroscopy. *J. Res. Nat. Bur. Stand. Sec. A: Phys. Ch.* **1970,** *74A*, 542-558.

(191) Schouten, K. J.; Qin, Z.; Perez Gallent, E.; Koper, M. T. Two pathways for the formation of ethylene in CO reduction on single-crystal copper electrodes. *J. Am. Chem. Soc.* **2012,** *134*, 9864-7.

(192) Schouten, K. J. P.; Pérez Gallent, E.; Koper, M. T. M. The influence of pH on the reduction of CO and CO_2 to hydrocarbons on copper electrodes. *J. Electroanal. Chem.* **2014,** *716*, 53-57.